La collana della Scuola di Alta Formazione Dottorale accoglie le migliori tesi di dottorato dell'Università degli Studi di Bergamo, insignite della dignità di stampa e sottoposte a procedura di *blind peer review*.

Additive Manufacturing represents one of the Key Enabling Technologies that allow the manufacturing industry to move forward to its highest evolved form thanks to its high design flexibility, the reduction of scrap materials, and the possibility to tailor the physical and mechanical properties of manufactured parts. More specifically, this work explores the feasibility of producing functionally graded parts by mixing two high-strength steels, i.e. AISI 316L and AISI H13, using Direct Laser Deposition. This work has evaluated the optimization and manufacturing process starting from the feedstock analysis to the deposition of two kinds of functionally graded materials. The optimized process parameters were validated by producing FGMs benchmarks, which are properly designed and characterized.

Alessia Teresa Silvestri received her PhD in Technology, Innovation and Management (34th cycle) from the University of Naples Federico II and the University of Bergamo (Italy). Her scientific interests are in additive manufacturing, both for metals, such as powder-bed-fusion or wire- and powder-directed energy deposition, and for polymers/composites, such as fused deposition modeling and continuous fiber fabrication. Her studies are focused on the manufacturing of customized products with different materials or properties, with mechanical, metallurgical and surface characterizations.

ISBN: 978-88-97413-79-0
DOI: 10.13122/978-88-97413-79-0

Alessia Teresa Silvestri

DLD PROCESS OPTIMIZATION

57

Collana della Scuola di Alta Formazione Dottorale
- 57 -

Alessia Teresa Silvestri

OPTIMIZATION OF DIRECT LASER DEPOSITION PROCESS for Hybrid and Tailored Structures

UNIVERSITÀ DEGLI STUDI DI BERGAMO

2023

Collana della Scuola di Alta Formazione Dottorale

Diretta da Paolo Cesaretti

Ogni volume è sottoposto a *blind peer review*.

ISSN: 2611-9927

Sito web: https://aisberg.unibg.it/handle/10446/130100

Alessia Teresa Silvestri

OPTIMIZATION OF DIRECT LASER DEPOSITION PROCESS
for hybrid and tailored structures

Università degli Studi di Bergamo

2023

Optimization of Direct Laser Deposition Process
for Hybrid and Tailored Structures / Alessia Teresa Silvestri. – Bergamo : Università degli Studi di Bergamo, 2023.
(Collana della Scuola di Alta Formazione Dottorale; 57)

ISBN: 978-88-97413-79-0
DOI: 10.13122/978-88-97413-79-0

Progetto grafico: Servizi Editoriali – Università degli Studi di Bergamo
© 2018 Università degli Studi di Bergamo
via Salvecchio, 19
24129 Bergamo
Cod. Fiscale 80004350163
P. IVA 01612800167

https://aisberg.unibg.it/handle/10446/258449

Table of contents

Introduction

We are living in the Age of the fourth industrial revolution, whose manufacturing paradigm is referred as Industry 4.0 and is founded on nine core pillars: Big Data, Autonomous Robots, Simulation, Additive Manufacturing, Internet Of Things, Cloud Computing, Augmented Reality, Horizontal And Vertical Integration, and Cyber Security. The present work is well framed in this context and particularly lies in the Additive Manufacturing (AM) research field. Due to its high design flexibility, the reduction of scrap materials and the possibility to tailor the physical and mechanical properties of manufactured parts, AM represents one of the Key Enabling Technologies that allow the manufacturing industry to move forward to its highest evolved form. As suggested by ASTM International, AM processes can be classified according to different aspects, such as the aggregate state of the feedstock, the material distribution and the source of fusion. Among the AM family, the most intriguing technology to produce tailored and customized components is the Direct Laser Deposition (DLD), which uses a focused laser beam to fuse metallic powders as they are being deposited on a substrate. Moreover, DLD can be used to produce new parts, for coating applications, repair existing damaged parts, and manufacture items with tailored local composition and customized properties. The latter are called Functionally Graded Materials (FGMs), a new class of high-performing materials that is gaining great attention in both industry and academia due to their interesting potentialities. DLD and FGMs have the potential to overcome a critical issue in the die and mold industry related to the premature failures of the tooling, allowing the possibility of repairing the damaged molds instead of replacing them. Indeed, when upgrading an existing component with a new AM part, intermediate layers are commonly employed as buffer material. H13 tool steel and 316L stainless steel are suitable for these purposes and are the materials used. In this context, the research objective is to enrich the actual landscape of DLD production of engineered FGMs components with custom and tailored properties. To tackle this aim, two different research streams will be simultaneously pursued:

i) explore the potentialities of DLD for the fabrication of tailored and customized components, in terms of both properties and composition;
ii) the formulation of established process guidelines, overcoming the actual scarce robustness of the technology for creating FGMs.

To this aim, the present work includes an extensive experimental campaign whose outcomes are discussed in a critical analysis. An introduction to additive manufacturing in general, and the DLD process in particular, will open this work, then the process parameters that play a key role both in the

process and in the design phase are explained in detail. The work continues by describing the crucial steps of process parameters optimization, carefully illustrating each step, pointing out the lack of established guidelines and showing how this knowledge gap can be filled.

In the optimization of the process parameters, the first step is represented by the characterization of H13 and 316L powders in order to find the chemical composition, size, shape, and defects.

The study of the 3D printing process has been organized and will be presented following a criterion of increasing complexity: first will be shown the single tracks, then a scan strategy will be implemented to produce single layers and after that, the manufacturing of walls, cubes and parts will be reported. The outcomes of each section are one of the required inputs for the next step.

Concerning the Single Tracks (STs) analysis, the different processing conditions explored in the experimental campaign were designed by defining and then varying the most influent process parameters, i.e. Laser Power, Powder Feed Rate and Scanning Speed. Particular attention is paid in this section to the analysis procedure, highlighting the gap of knowledge in the literature concerning the scientific rigor to determine the optimum in terms of process parameters for evaluating STs. After the selection of the best combination of process parameters that fit the above-mentioned criteria, explained in detail in the correlated section, the following step was represented by the production of Single Layers, with the introduction of other influent process variables, i.e. the deposition strategy and overlap. The procedures to deposit and analyze the SLs are described and discussed, referring to the literature. A parallel step to the deposition of SLs is the one of Thin Wall (TW). Due to technological issues of the machine, the results are not satisfactory in terms of regular shapes and defects. It was deduced that TW could not be an indicative step to the determination of three-dimensional bulk buildings, but a further and separated experimental campaign is needed to create thin structures. This point allowed to point out some issues which should be fixed to allow the manufacturing of thin parts. At this point, on the basis of the previous step, in section 7.5, the deposition of FGMs structures is described, and precisely two FGMs are considered. The first one, named Graded (G), with a gradient in the chemical composition: 316L decreases as well as H13 increases from the bottom to the top, and vice versa. The second item was named Wafer (W), and it is made of an alternation of single layers of 316L and H13. Both cases are investigated considering the influence also of the two deposition strategies employed. As mentioned, every step enables the successive one. At the end of each section, the related results were characterized by considering geometrical, metallurgical, and mechanical behaviour through established requirements. The most influent process parameters, namely laser power, powder feed rate, scanning speed and overlap, have been balanced for Sigle Tracks and Single Layers, to provide the best trade-off between the geometrical thresholds of the wetting angle ($\alpha>100°$), Aspect Ratio ($AR>5$), Dilution

(10%<Dil>30%), Shift (S<50μm), and Waviness (W<12μm). The resulting laser power, powder feed rate, scanning speed and overlap (respectively 2000W, 15 g/min, 1200 mm/min, 60%) have been used for FGMs structures. In the Graded structures, gradual changes in the chemical composition have been detected; in the Wafer structures, changes with a stair-step effect. The microstructural evolution has involved the transition from austenitic 316L to H13, predominantly made up of martensite, from the bottom to the top in G parts and at the interface between layers in W components. The hardness has gradually changed from ~200HV (316L) to ~700HV (H13), with intermediate values in the transition zone, or alternated them, respectively, in G and W structures. Both deposition strategies studied, namely Zig and ZigZag, have respected the metallurgical and hardness requirements, with major reflections of design data in the Zig strategy specimens. Moreover, the FGMs have not shown delamination between layers under bending stress, showing that brittle and ductile failures occur depending on 316L and H13 in the extrados layers. The correct management of the process parameters was validated by the production of FGMs benchmark, both Graded and Wafer. Following the preliminary conclusions for each of the steps studied, more general conclusions are drawn in the last part of the book, relating both to the main experimental results and to the main limitations highlighted with respect to the manufacturing guidelines.

Chapter 1. Additive Manufacturing

Nowadays, the world is living in the Age of Industry 4.0, a new industrial revolution that combines physical and digital aspects of production with the aim of increasing productivity, reducing costs, and improving flexibility and customization [1]. The Boston Consulting Group described Industry 4.0 through nine core pillars that affect manufacturing growth: big data, autonomous robots, simulation, additive manufacturing (AM), internet of things (IoT), cloud computing, augmented reality, horizontal and vertical integration and cyber security [2]. In this context, Additive Manufacturing is a relatively new technology that represents the perfect symbol of a new vision of manufacturing that can merge the real and virtual worlds, starting from a customized design to a near-net-shape and ready-to-use. AM has been gaining importance over the last decade, demonstrating the possibility of revolutionizing the manufacturing industry by breaking the typical boundaries of the traditional subtractive manufacturing processes [3]. Indeed, AM represents one of the *Key Enabling Technologies* that allow the manufacturing industry to move forward to its highest evolved form [4]. AM has many strategic advantages over traditional manufacturing processes: the production of complex internal and external geometries that cannot be produced in any other way, rapid iteration through design permutations. The technology first emerged in 1987 with stereolithography (SL) and has since evolved from a limited number of expensive prototypes to widely used low-volume production tools. According to the first standard related to AM terminology, ASTM F2792-10 (2010), AM was defined as: “the process of joining materials to make objects from 3D model data, usually layer upon layer, as opposed to subtractive manufacturing technologies” [5]. Due to the rapid evolution of these technologies, this standard was either superseded and replaced by a new version, ISO/ASTM 52900:2015(E), where AM was more correctly described as: “the process of joining materials to make *parts* from 3D model data, usually layer upon layer, as opposed to subtractive manufacturing and formative manufacturing methodologies” [6]. The process is based on the material incrementing, with a primary step represented by a Computer-Aided Design (CAD) model that translates the design into a 3D object, it is then divided into plans called layers, and the final object is the result of the addition of material layer by layer [7]. Currently, there are several benefits of AM with respect to conventional manufacturing that facilitates the production of moderate to large products batches: these include high levels of geometrical complexity achievable, fast prototyping, reduced time to market, a large availability of materials and feedstock, waste reduction, near net shape production and so on [8], [9].

1.1 Classification of Additive Manufacturing technologies

Nowadays, many different AM technologies are mainly differentiated by the class of material and the feedstock used. These variables determine which AM technology should be used, considering the final applications. Figure 1 shows some of the currently available and most used AM processes to give a comprehensive overview.

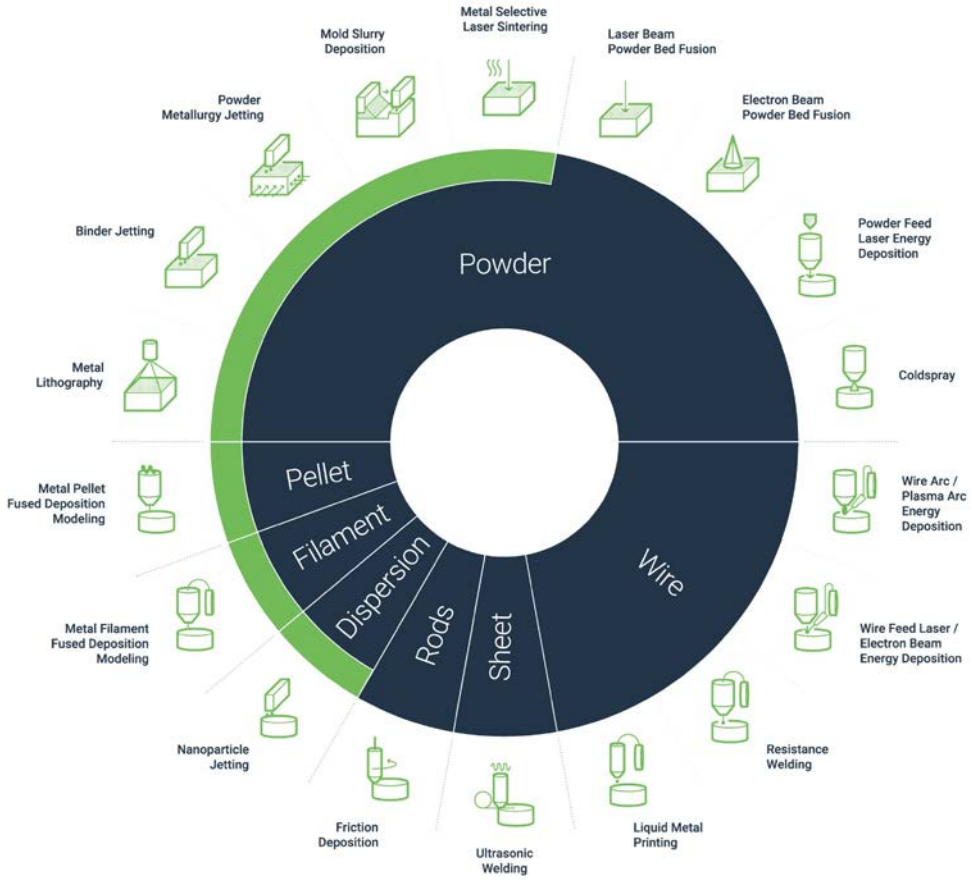

Figure 1: Classification of Additive Manufacturing technologies according to the feedstock [10].

As above-mentioned, the commercial use of AM first emerged with StereoLithography, developed by 3D Systems. It was a process that solidified thin layers of ultraviolet light-sensitive liquid polymer using a laser [11]. Since then, the number of AM technologies for polymers has increased significantly. An overview of AM technologies for polymers is shown in Figure 2 and some of the most widespread will be introduced in the following.

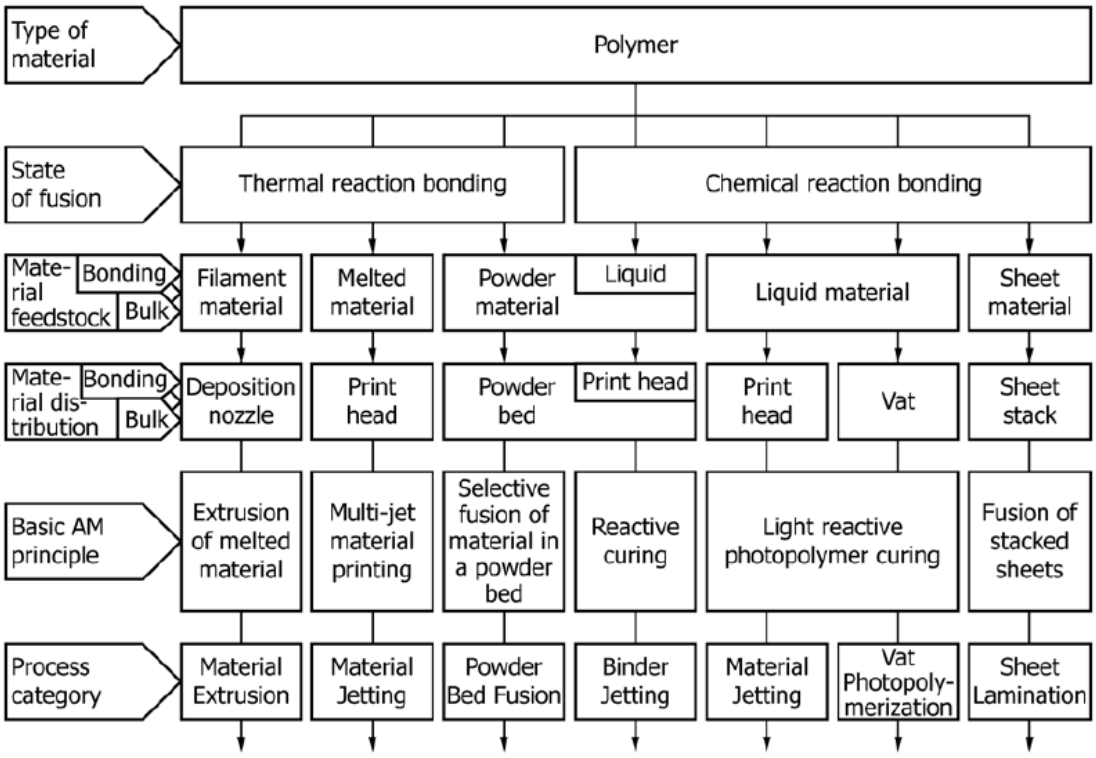

Figure 2: Overview of Additive Manufacturing technologies for polymers [6].

One of the most used technology is Fused Deposition Modeling (FDM), due to the lower costs of the commercialized machines, ease of use and other advantages [12], [13]. It is a technology that uses a plastic thread wound on spools to produce items layer by layer. In this process, one or two materials can be used; in the latter case, the materials to make the workpiece and the supports are different. Concerning the working principle, the filament in the spool is heated until it reaches a viscous state at the extrusion nozzle and is drawn to the extrusion head. Two calibrated and heated extruders are associated with the print head. The extruders melt the polymer and deposit it on the print bed with an X-Y motion. Once the part is finished, it is pulled out of the working chamber and the backing material is removed [14]. The most common commercially available thermoplastic materials for FDM filaments include acrylonitrile butadiene styrene (ABS) and polylactic acid (PLA), polyvinyl alcohol (PVA), poly-caprolactone (PCL) and polyamide (nylon). High-performance engineering thermoplastics such as polyetheretherketone (PEEK) and polyetherimide (PEI) are also commercially available.

Moreover, further and recent studies have investigated the adoption of Additive Manufacturing technology to produce fiber-reinforced composite materials [15]–[17]. Indeed, it is well-known that the use of composite materials to have products with a high strength-to-weight ratio is important, for example, for automotive, aeronautics and aerospace applications [18]. On the other hand, AM can overcome the limits of conventional manufacturing processes, such as the necessity of a mold, limited

complex-shaped and geometries realizable, waste material, etc. In this context, Continuous Fiber/Filament Fabrication (CFF, also known as FFF: Fused Filament Fabrication) has gained great consideration. It is a process belonging to the FDM family that can simultaneously deposit two materials in each layer during the realization of the product. This is possible thanks to two extruders for matrix and fiber. According to the working procedure, the thermoplastic polymer yarn is heated to a quasi-liquid state, allowing it to pass through a heated nozzle where it is fused on a base plate and, in addition, along with the reinforcing filament if the layer is selected. When continuous (carbon, glass, and/or aramid) fibers are printed in-plane, they have the potential to significantly increase the in-plane strength and stiffness of the AM part compared to traditionally printed parts [19]. A very interesting advantage of this technology is the possibility to design and print a composite component featured by a complex fiber orientation, which can be applied to geometric interrupts such as holes [20].

Regarding metals, Figure 3 shows a schematic representation of the most commonly used metal AM techniques, whose most used are the ones in which the feedstock is in powder form. The main techniques that have greater industrial relevance are Selective Laser Melting (SLM), also known as Laser-Powder Bed Fusion (L-PBF), Electron Beam Welding (EBM), and Directed Energy Deposition (DED). In the PBF techniques, the powder is pre-dispersed on a working plate before interacting with the energy source; in the DED technique, the powder is sprayed on a substrate, carried by an inert gas through one or more nozzles, and simultaneously hit by the energy beam. The latter was carefully described in the following chapter.

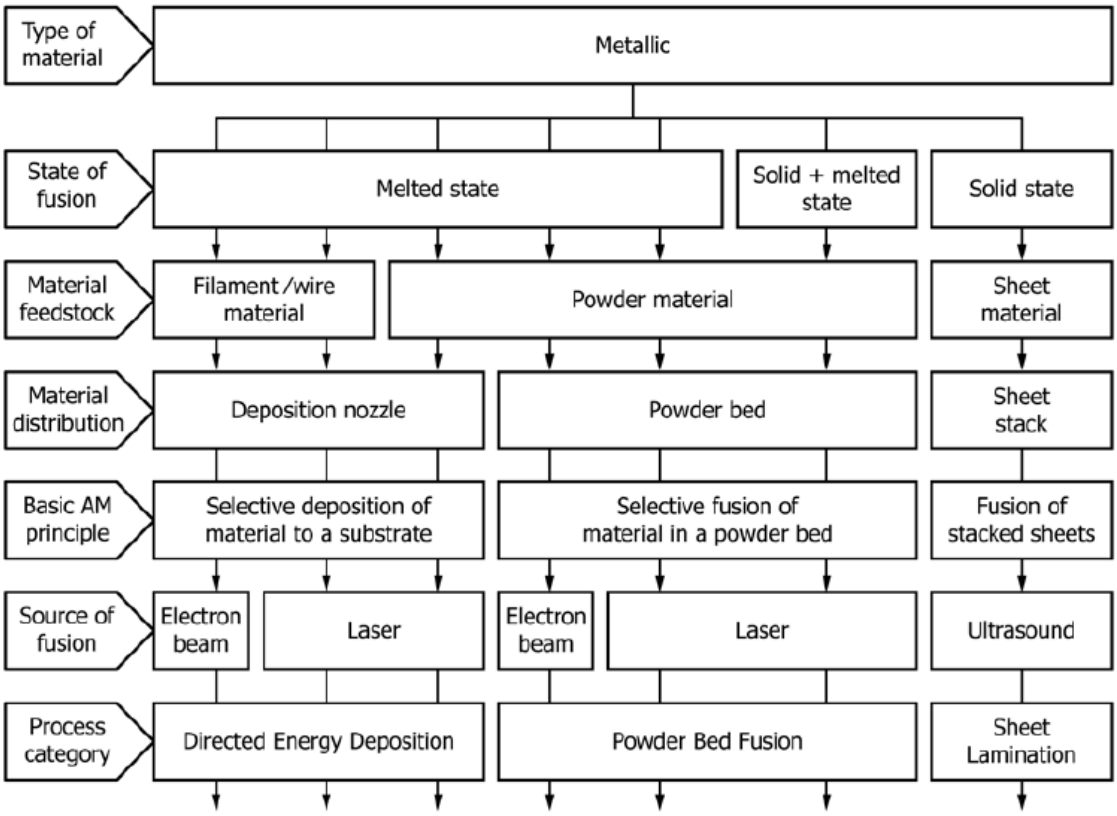

Figure 3: Overview of Additive Manufacturing technologies for metals [6].

In the SLM process, a layer of metal powder is spread onto the plate in a building chamber, in particular, the height of the layer is equal to the desired thickness, then a laser beam is focused on the selected areas to melt, the build plate moves down and the process is repeated until the part fabrication is concluded (Figure 4). As introduced before, SLM is one of the most well-investigated technology and can be used for several alloys, such as steels, aluminum, titanium and nickel alloys, including AlSi10Mg, Ti6Al4V, 316L, and so on [21]. An inert atmosphere of nitrogen and argon is required to prevent the oxidation of the powder. In other words, the SLM is a multi-stage process in which, firstly, air and residual materials are removed from the working chamber and, secondly, inert gas is added. It is essential that the oxygen concentration is less than 0.1% to avoid deterioration of the powder.

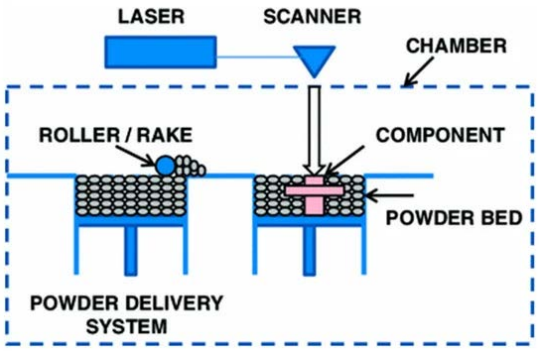

Figure 4: Schematic principle of L-PBF process [22].

The working procedure of the EBM technology is similar, but the heat source is an electron beam. Indeed, in this process, a high-intensity heat source, the electron beam, interacts with the feedstock powders and produces a melt pool, where rapid melting and solidification occur [23]. In EBM, parts are fabricated in a high vacuum chamber providing an ideal contamination-free atmosphere for reactive materials, such as titanium alloys, that have a high affinity to nitrogen and oxygen. Additionally, EBM generates a faster build rate, compared to SLM, due to its superior energy input and faster scan rate [24]

Chapter 2. Direct Laser Deposition

As introduced in the previous chapter, Directed Energy Deposition processes allow parts to be manufactured by melting the material during deposition. This basic approach can be used for various materials such as polymers, ceramics, and metal matrix composites; feedstock typically comprises either powder or wire, but is mainly used for metal powders. Therefore, this technology is often referred to as "metal deposition" [25].

DED systems also comprise multiple categories of machines using laser beam, electron beam, or arc plasma energy sources. Deposition typically occurs either under inert gas (arc systems or laser) or in vacuum (electron beam systems) [26].

2.1 Direct Laser Deposition technology

Direct Laser Deposition (DLD) is one of the promising additive manufacturing technologies used to produce new components, repair and rebuild worn or damaged parts, and apply wear- and corrosion-resistant coatings. DLD produces fully dense, functional metal parts directly from CAD data by depositing metal powders using laser melting [26]. The feedstock is usually metal powders, but can also be provided in wire form. In this context, exploiting the powder-based DLD technology through the optimization of the process parameters is part of the aim of the present work. According to the standard ASTM F3187-16, the Laser-based DED systems working principle is to use a laser beam and focusing optics to provide highly controllable energy to localized areas of the substrate [27]. One of the first DLD machines was commercialized by Optomec, in 1997, with the associated trademark LENS®, i.e. Laser Engineered Net Shaping, developed by Sandia National Laboratories (USA). Meanwhile, this technology has gained great attention, with the consequence of the development of the very similar technologies around the world: Shape Deposition Manufacturing (USA-Stanford), freeform laser consolidation (National Research Council, Canada); Selective Laser Cladding (SLC) (University of Liverpool, UK) [26].

As shown in Figure 5, this powder-based process has a different configuration than the L-PBF processes. More precisely, the powder spreading, melting and subsequent consolidation occur almost simultaneously thanks to a delivery nozzle coaxial to the heat source (i.e., the laser). Usually, an inert gas is used to transport powders from the feeders to the nozzle and simultaneously protect the molten material from atmospheric contaminations and oxidation.

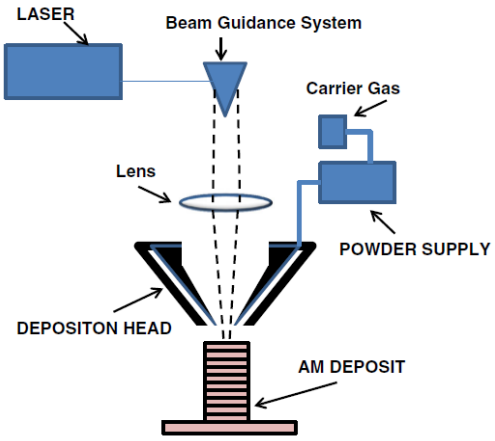

Figure 5: Schematic principle of Powder Direct Laser Deposition process [22].

Moreover, the transport of metal powder from the powder container to the area of interest in the working please can occur mainly in two ways: coaxial feeding or side-nozzle feeding, shown in Figure 6 [25].

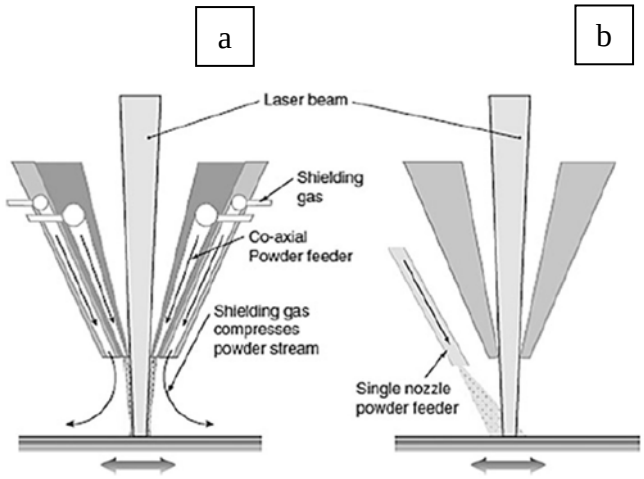

Figure 6: Schematic representation of powder nozzle configuration: a) coaxial nozzle feeding, b) side-nozzle feeding [25].

In the first case, the powder was fed into the process coaxially with the laser beam. The two main advantages are the good efficiency of the powder and the protection against oxidative phenomena of the surface layers. On the other hand, a single nozzle was directed at the interaction zone between the laser and the substrate in side-nozzle feeding. Among the benefits of this kind of feeding, there is the low cost of the apparatus due to its simplicity and the good accessibility to critical zones in comparison to coaxial feeding, in other words, a major possibility to deposit material into tight zones, such as the internal surface of channels or tubes. On the other hand, the main disadvantage is that the geometry of the melt pool depends on the deposition direction; for this reason, it is mainly used for coating and not for three-dimensional manufacturing. Indeed, the most common machine

configurations for the DLD process comprise a deposition head that contains the heat source and the powder delivery system, and this is the structure of the depositing head of the machine used in the present work, DMG MORI LASERTEC 65 (carefully described in Chapter 5), shown in Figure 7.

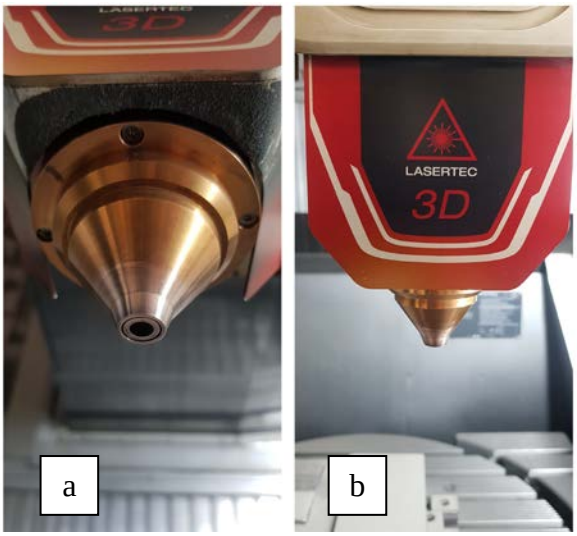

Figure 7: Deposition head of DMG MORI Lasertec 65: a) bottom view and b) front view.

The powder is typically fed by first fluidizing a container of powder material, such as, for example, by bubbling up a gas through the powder and/or applying ultrasonic vibration. Specifically, the DMG MORI Lasertec 65 3D uses a rotating disc system to transport the powder from the container to the nozzle (see section 5.1 for details); it means that the quantity of powder feed is adjusted by varying the Revolutions Per Minute (rpm) of a stirrer situated inside the containers, the rpm of the disk system and liters per minute of the stirrer gas rate. With the combination of the last three parameters, an essential process parameter is obtained, i.e. “Powder feed rate”, measured in grams per minute (g/min). Calibration should be carried out before each deposition, even for the same material, if the deposition is done on different days, considering the influence of external factors such as environmental temperature, humidity, and/or different amounts of powders in the container.

2.3 Process parameters for powder-based Direct Laser Deposition

In DLD technology, the process parameters can be categorized into three groups related to material, machine and process, shown in Figure 8.

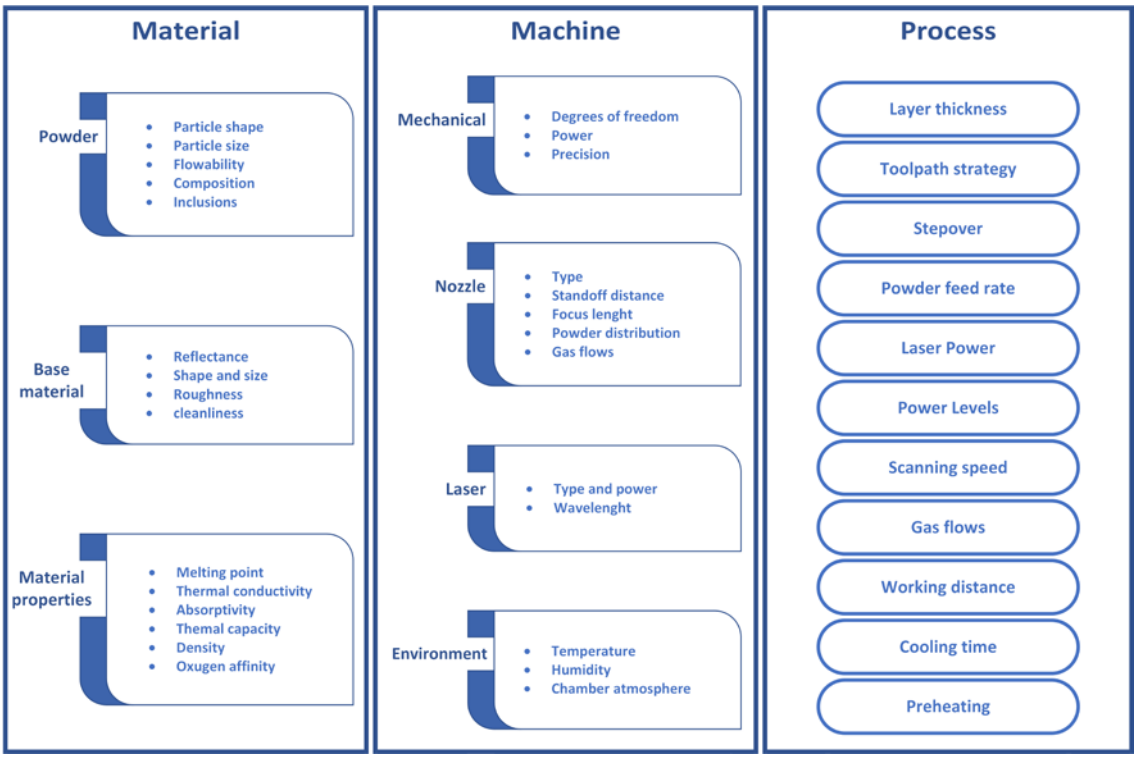

Figure 8: Process Parameters of Direct Laser Deposition.

The figure aims to show the complexity of the operations involved in the DLD process and the troubles in managing such a quantity of parameters simultaneously.

2.4 Advantages and Drawbacks

The following drawbacks and advantages have been pointed out from a comparison of DLD with SLM and EBM:

- DLD process provides considerably higher building rates compared to SLM and EBM [28]. For this reason, it is gaining increasing interest from the industry given the major productivity;
- The design freedom offered by DLD is higher than SLM/EBM, considering the very localized feedstock manipulation. For instance, special attention should be paid when employing PBF processes for the manufacturing of particular geometries with closed cavities, in which the loose powder might be trapped upon the material consolidation;
- Still considering the higher build rates provided by DLD, it is clear that this process becomes more cost-effective compared to PBF processes as the raw material costs increase [29];
- As a consequence of the major freedom of design, DLD represents a flexible process for the manufacturing of new parts and materials build-ups and parts refurbishing [22].
- The feedstock and the molten material protection from the environment are more difficult for DLD machines.

Chapter 3. Functionally Graded Materials

3.1 State of the art

Functionally graded materials (FGMs) are novel composite materials with gradual variations in their composition and structure throughout their volume and, therefore, locally tailored properties. Unlike isotropic bulk materials, the compositions and structures of FGMs can be precisely designed to exhibit tailored multifunctional properties. FGMs are of great interest for numerous applications, including aerospace engineering, nuclear power generation, sensors, biomedical implants, optoelectronic devices and energy absorption systems [30]–[32]. They were firstly proposed by Naotake Noda in order to solve the thermal problems that the combustion chamber of a hypersonic space plane deals with. Indeed, the temperatures involved can range from 1000K to 2000K and, under these conditions, failure in a composite material occurs via delamination (detachment of fibers from the matrix) [33]. Therefore he has proposed a new class of materials, namely Functionally graded materials [34].

FGMs represent a revolution in the field of engineering materials. The idea was born by observing structures composed of graded components as well as exhibiting graded properties that overcome those of the individual constituent and present in nature, for example, bones, teeth, and wood [35]. As pointed out by Mahamood et al., the concept is emulated from nature to solve engineering problems in the same way the artificial neural network is used to emulate the human brain [36]. For this reason, in the last years, they have gained great interest in both industry and academia due to their intriguing potentialities. FGMs are characterized by gradual transitions in either composition/constituents or microstructures (e.g., grain size, texture, porosity, etc.) along at least one direction, resulting in functional modifications associated with at least one property [37], [38]. FGMs can be classified into discontinuous and continuous FGMs, as schematically shown in Figure 9, respectively. In discontinuous FGMs, the compositions and/or microstructures change with a stairstep effect. In contrast, in continuous FGMs, the compositions and/or microstructures change gradually with positions. Moreover, graded structures are present either in the whole material or only in some localized areas.

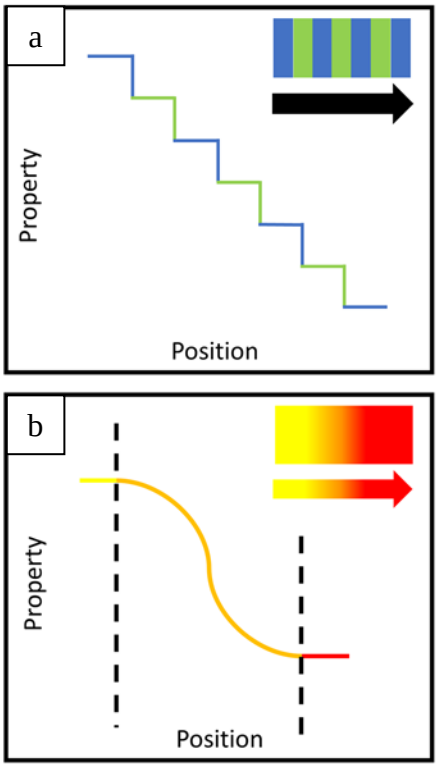

Figure 9: Schematic diagrams illustrating: (a) discontinuous and (b) continuous Functionally Graded Materials.

Summarizing what has been described in previous chapters, additive manufacturing is a near-net shape manufacturing process that can be used to directly manufacture complicated 3D objects without requiring molds, tooling, or the need for joining or assembling. In addition, AM has the advantage of allowing flexible designs that can be optimized for specific geometrical requirements or applications where complex procedures or geometries are too time-consuming, expensive, or difficult to achieve by conventional manufacturing processes. In this scenario, AM processes perfectly match the nature of FGMs, particularly powder-based laser deposition processes.

3.2 Current challenges

Direct Laser Deposition is creating new avenues to manufacture advanced functional materials with complex gradients and highly specific properties through precise control of compositions, constituents and structures at multiple length-scales, as well as the integration of multiple gradients [39]. It is expected that in the future, such advanced multi-materials will be used for the development of novel 3D structures and functionally graded devices. So far, scientists have creatively proposed various AM technologies for the manufacture of FGMs [40]; however, real industrial applications are still far and still need significant and comprehensive research efforts in order to solve a large number of issues and challenges involved. Zhang et al. provided an excellent overview of the challenges of

producing FGMs [41]. They have mainly highlighted the high number of variables involved in the AM processes (power density, powder flow rate, displacement velocity, substrate characteristics, etc.) that affect the resultant microstructure, phase composition and properties of items. On these bases, they have emphasized that the main issue is the needing of optimized multiple variables, necessary to obtain reproducible properties for a specific material system and, so, for an industrial spreading. However, other developments are needed, including theoretical and numerical models and software that can simulate the physical processes of FGM and predict the geometries, properties, and functional performance of manufactured components.

Chapter 4. Developed research solutions and contents

4.1 Aim of the research

The aim of the present work is to generate new knowledge through an experimental approach that will contribute to enrich the actual landscape of DLD production of FGMs components with custom and tailored properties. More specifically, this work explores the feasibility of producing functionally graded parts by mixing two high-strength steels: AISI 316L and H13. To tackle with this aim, two different research streams will be simultaneously pursued:

i) explore the potentialities of Direct Laser Deposition in producing tailored parts with customized mechanical properties and chemical composition;

ii) the formulation of reliable process guidelines, overcoming the actual scarce robustness of the processing routes adopted to produce functionally graded structures.

The developed research solutions, sketched in Figure 10, are expected to have a deep impact on the manufacturing industry, enabling Direct Laser Deposition as a viable process to obtain the above-mentioned structures by providing reliable manufacturing guidelines.

The present research work is founded on an extensive experimental campaign focused on stainless steel 316L and tool steel H13, whose outcomes are discussed in critical analysis with the objective of improving the engineered materials scenario for the die and mold applications related to their hardness and corrosion resistance properties. To prove the effectiveness of the guidelines released, as a final step of this piece of work, an FGM part, intended as a benchmark of the developed knowledge, has been produced and tested.

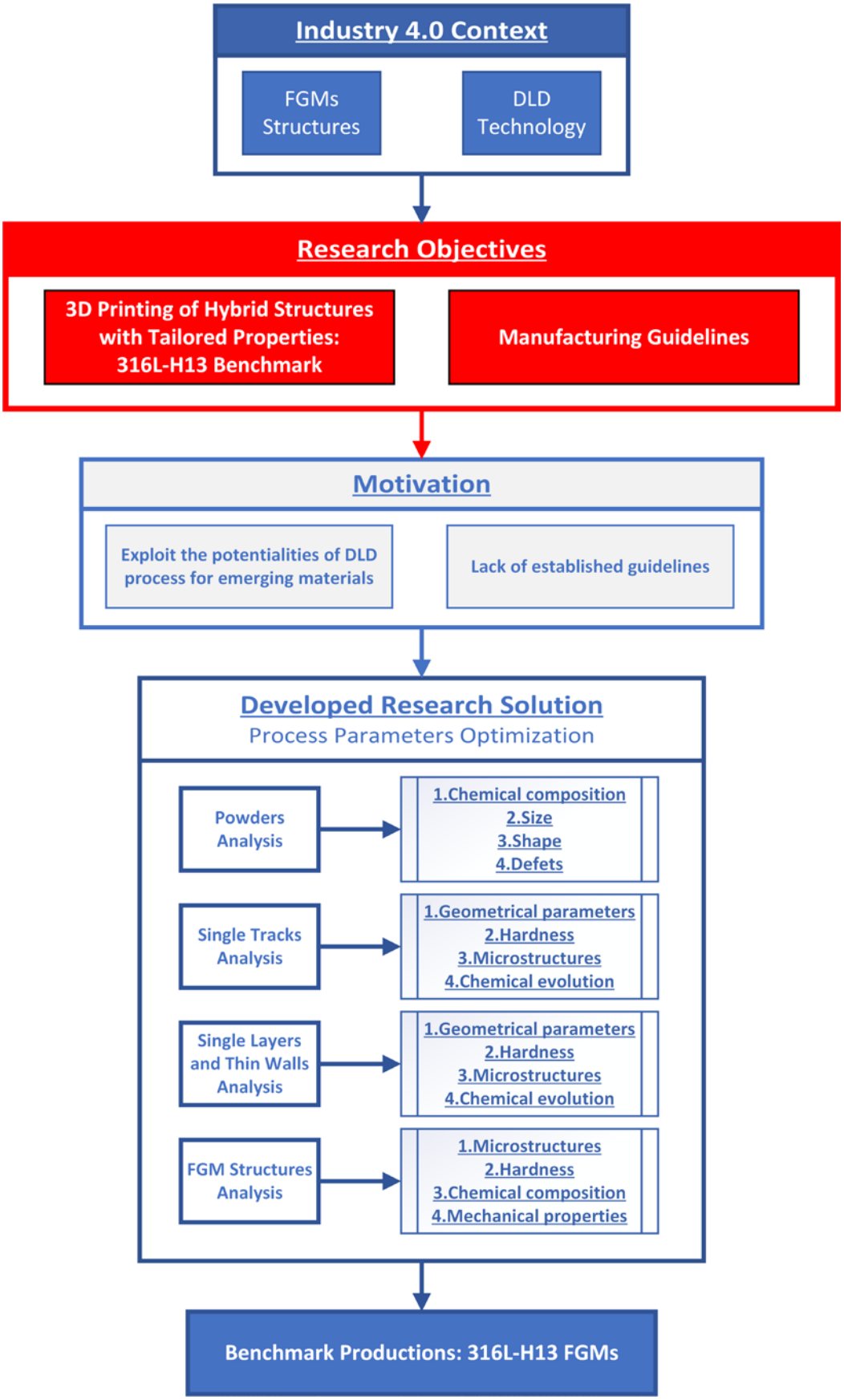

Figure 10: Flow-chart of the research carried out.

4.2 Table of contents

The present work is organized into nine chapters, as illustrated in Figure 11.

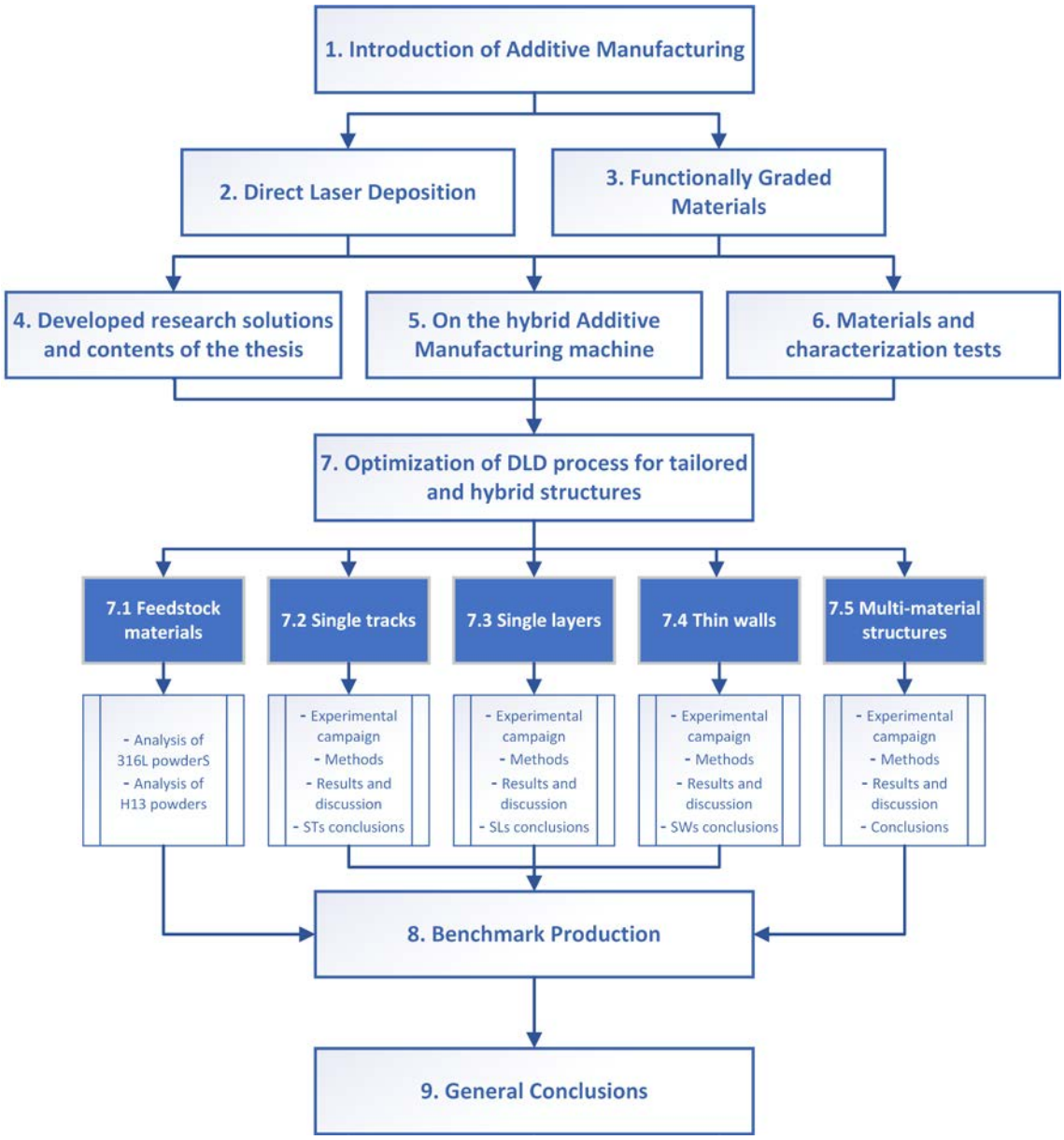

Figure 11: Organization scheme of the chapters.

Chapter 1 defines the framework of Industry 4.0, based on nine core pillars, whose the one of interest is Additive Manufacturing. An introduction giving some information about the origin of AM in combination with the advantages of AM over conventional manufacturing technologies will be provided. Since AM processes can be classified according to the starting material and the most widely used are polymers/composite and metals, a brief overview of AM for these two types of materials has been given, followed by a description of the most commonly used processes. In particular, Fused Deposition Modeling for polymers, Continuous Filament Fabrication for composites, Selective Laser Melting and Electron Beam Melting for metal powder-bed technologies.

Chapter 2 illustrates the Direct Laser Deposition process that belongs to metal powder-AM technologies and that uses a laser beam as a heat source to melt the powder. The difference between Direct Laser Deposition and Selective Laser Melting is the mode used to build every layer. Direct Laser Deposition uses a focused laser beam to fuse metallic powders as they are being deposited on a substrate. In contrast, in Selective Laser Melting, a pre-laid powder bed of the height ideally set equal to the layer thickness, is selectively melted by the laser source. DLD technology can be adopted to produce new parts with tailored local composition and properties, as well as to upgrade or repair existing damaged parts, providing advantages compared to the SLM that cannot be used for the latter purposes. In all cases, DLD has the potential to vary the chemical composition within a build to produce functionally graded materials. For these purposes, proper management of process parameters is a crucial issue. For this reason, an overview of the process parameters involved is given, with a more detailed description of the most influential process parameters.

Chapter 3 gives a description of the functionally graded materials, some information about the origin, and clarifies the advantages with respect to metals or alloys.

Chapter 4 explains the research objectives and the developed solutions, namely to generate new knowledge through an experimental approach that will contribute to enrich the actual landscape of DLD production of FGMs components with custom and tailored properties.

Chapter 5 describes in detail the DLD machine employed in the present work: a five-axis hybrid AM machine DMG MORI LASERTEC 65. Particular attention is paid to the powder feeding apparatus, based on a rotating disk system, due to the importance of the transport of the powders in the DLD process. The AM machine is equipped with CAD/CAM associated software that allows to design the 3D CAD model, manage the tool operations through the CAM section, and obtain a G-Code File to insert in the machine. After the explanation of the CAD/CAM workflow, the next section describes the most important toolpath parameters.

Chapter 6 describes the feedstock materials used: stainless steel 316L and hot-worked tool steel H13. Such a choice for two main reasons: i) they are an example of the production of FGMs with tailored properties, such as a gradient in hardness and microstructures; ii) they are also a combination of great interest in the die and mold industry. Indeed, DLD can be used to both coat or repair components in case of a premature failure of these high-added-value parts instead of replacing them. When upgrading an existing component with a new AM part, several intermediate layers are commonly employed as buffer material. Once again, the optimization of the process parameters is needed to ensure the best adhesion and integration of the added part, and the related properties. Moreover, it was summarized the characterization tests employed in each step of the process parameters optimization.

Chapter 7 points out the importance of the optimization of the process parameters and the steps to follow, organized in a workflow. The first step is represented by the characterization of both powders, to prove the compliance of the actual chemical composition, size, and shape, with respect to the nominal ones and to search for internal defects. Then, it is followed by the Single Tracks (STs) analysis. The different processing conditions explored in the STs experimental campaign were designed by defining and then varying the most influent process parameters, i.e. Laser Power, Powder Feed Rate and Scanning Speed. Particular attention is paid in this section to the analysis procedure, highlighting the gap of knowledge in the literature concerning the scientific rigor to determine the optimum in terms of process parameters for evaluating STs. Detailed guidelines are then provided, based on quantitative characterizing geometrical parameters, metallurgical considerations and hardness values. After the selection of the best combination of process parameters that matches the above-mentioned criteria explained in detail in section 7.2, the following step was represented by the production of Single Layers, with the introduction of other process variables, i.e. the deposition strategy and overlap. Also, the procedure to deposit and analyze the SLs is described and discussed, referring to the literature. Therefore, in section 7.3, guidelines to determine the proper results are provided, in combination with the process parameters that respect the geometrical, hardness, and metallurgical criteria. A parallel step to the deposition of SLs is the one of Thin Wall (TW). This step has pointed out some further technological issues that need to be solved before effective TW can be produced with this technique. An additional and separated experimental campaign, which lies out of the scope of this piece of work, is needed to create thin structures. At this point, on the basis of the outcomes of the previous step, in section 7.5 is described the deposition of FGMs structures, precisely two FGMs are considered: graded structures with a gradient in the chemical composition from the bottom, composed of 100% 316L that gradually decreases as H13 increases, to the top, made up of 100% H13. In other words, 316L decreases as H13 increases from the bottom to the top and vice versa. The second item was named Wafer, and it is made of an alternation of single layers of 316L and H13. Both cases are investigated considering the influence also of the two deposition strategies employed. Beyond metallurgical and microhardness analyses, three-point bending tests were carried out in order to study the mechanical behavior.

Chapter 8 describes the production of FGMs cubes intended as a benchmark of the developed knowledge to validate the manufacturing guidelines provided in Chapter 7, verifying the proper management of the process parameters.

Following the preliminary conclusions for each of the steps studied, more general conclusions are drawn in Chapter 9, relating both to the main experimental results and the main limitations highlighted with respect to the manufacturing guideline.

Chapter 5. On the hybrid Additive Manufacturing machine

5.1 The machine: DMG MORI LASERTEC 65 3D

DMG MORI LASERTEC 65 3D hybrid machine (LT 65 3D hybrid, DMG MORI AG, Pfronten, Germany) has been employed for all laser deposition experiments; it is located at ProM Facility Laboratory[1] (Figure 12), and hereinafter indicated as “Lasertec 65”. It is a five-axis hybrid system that merges Direct Laser Deposition technology with milling operations. It is equipped with a Coax 14 powder nozzle, a diode laser with wavelength λ=1020 nm and a maximum power of 3000 W. The spot diameter was 3 mm, with a top-hat beam profile and a focal length of 13 mm [42]–[44].

Figure 12: DMG MORI Lasertec 65 3D Hybrid machine used for all laser depositions.

As mentioned above, the Lasertec 65 has 5 degrees of freedom (DoF): three of them allow the laser head to move linearly according to the axes X, Y and Z in the building volume (Figure 13). The other two axes are used for the rotating movement of the worktable, in particular, the C-axis is the rotation around the Z-axis, it allows the worktable to swive left and right (yawing), while the A-axis allows the worktable to tilt forward and backward (pitching) from -120° to +120°, as illustrated in Figure 13.

[1] https://promfacility.eu

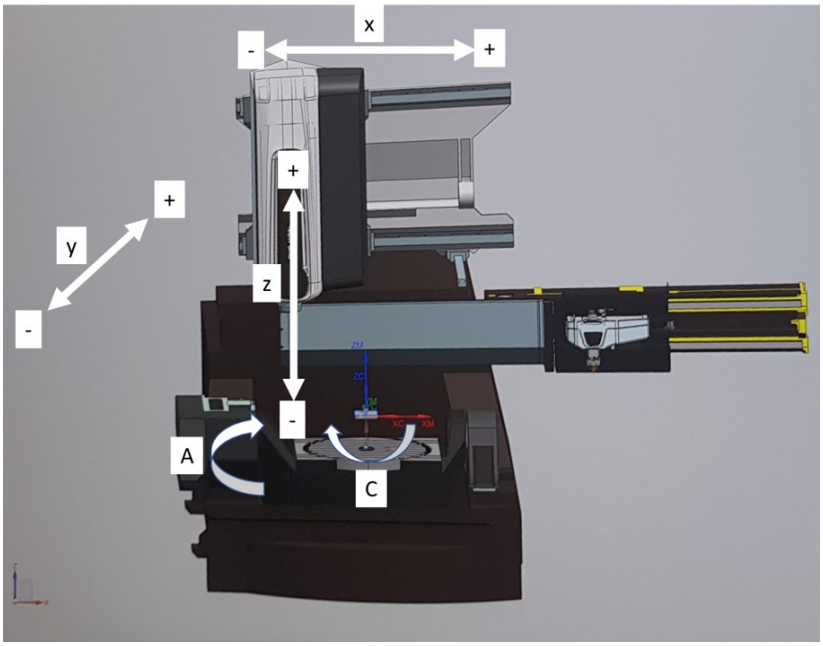

Figure 13: The five DoF on a schematic representation of the DMG MORI Lasertec 65 machine.

The building volume associated with the AM process is equal to a cylinder with a 500 mm diameter and 400 mm height. The worktable is powerful enough to handle objects weighing up to 600 kg. The machine is equipped with a software, Celos®, developed by DMG MORI, installed on an onboard computer. It includes useful apps to facilitate the management of procedures by the operator. Moreover, it is used to monitor the DLD process and allows manual changing parameters, such as laser power and powder feed rate, during the deposition by means of the touch-screen pc visible on the right in Figure 12. The machine also includes two powder hoppers (Figure 14).

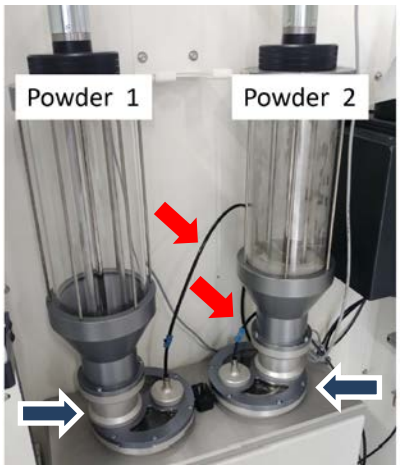

Figure 14: Powders feeders of the DMG MORI LASERTEC 65.

The cylinders are used both for storage and for metal powder transportation. The Lasertec 65 uses a rotating disk system to define the powder that is fed to the nozzle.

A stirrer is situated inside each cylinder and moves the powders on a spiral path inside the disks at the basis of the hoppers and indicated with the blue arrows in Figure 14, then the powders are transported by the carrier gas through the black pipes, indicated by the red arrows. With the setting of the correct stirrer rate, disk rate (velocity of the disk at the basis of the hoppers) and gas flow rate, it is possible to build functionally graded materials with gradual changes in the composition of the item layer by layer or deposited two different material layer by layer. It is worth recalling that, currently, this is the only technology that can offer these options. The gas flow rate imposed is used for the metal powder transportation and to cover and protect the molten materiel with a shield of inert gas, in the present work, pure Argon.

5.2 CAD/CAM workflow

As above-mentioned, AM process is based on material incrementing; the primary step is represented by a Computer-Aided Design (CAD) model that translates the design into a three-dimensional object [45]. The 3D source data can be obtained in several ways, including 3D scanning of existing physical parts, a design expert via a user interface, specialized software, or a combination of the previous methods. In the present work, professional CAD solid modeling software has been used to describe the external geometry fully. Computer-Aided Manufacturing (CAM) is the use of a software to manage the machine tool in the manufacturing process to obtain the shape defined during the CAD step. This is the principle of CNC machining technology in general; in particular, the machine employed in this work was equipped with dedicated software for the milling operations, but to actually operate in the Lasertec 65, Siemens developed a new section also for AM operations (Siemens NX CAD/CAM system) that is used both for add and remove material. The CAD/CAM workflow is illustrated in Figure 15. It starts with designing the necessary CAD models, then continues importing them in the CAM section. At this step, it is important to apply all required constraints to fix both baseplate and parts to build in the correct and real position that they will have in the CNC machine (in the present work, the Lasertec 65). The next step is modifying the components according to the operations to be performed and then choosing the toolpath parameters. In the case of graded or multi-material depositions, information like the kind of material (and its relative feeder), its position and quantity should be added in the CAM section. The last step is creating and exporting a G-Code file, which is then used in the CNC machine.

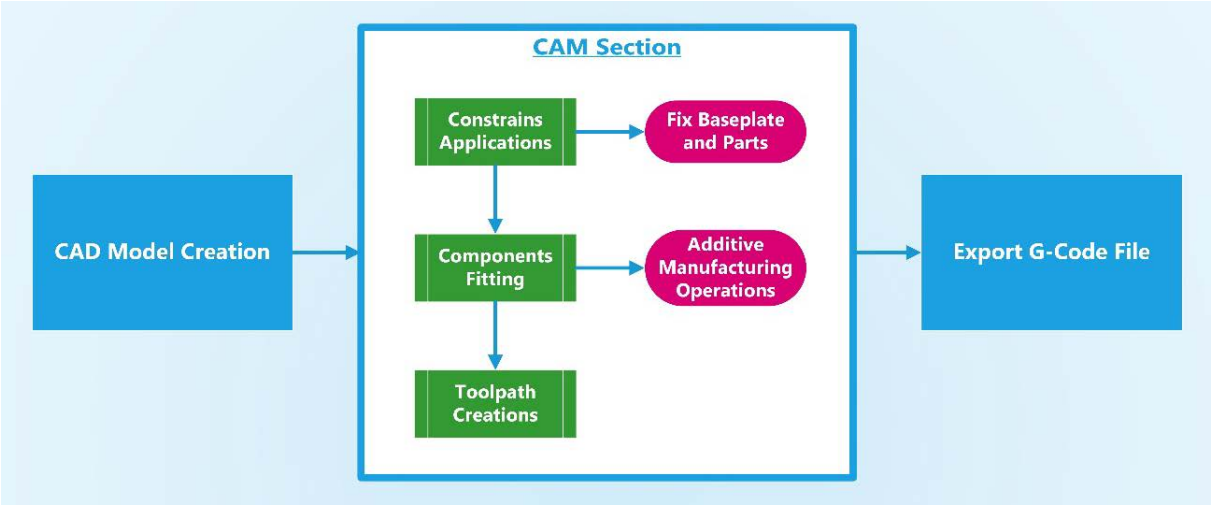

Figure 15: CAD/CAM workflow.

The software Siemens NX can simulate the process by showing the 3D model and the entire programmed process; this means that NX can display both additive and subtractive operations. The correct position of every model in the virtual building volume is essential and must be in agreement with the physical position in the Lasertec 65 (Figure 16) in order to check that no impacts between the tool and the part in construction occur during the actual process. It is possible to check the feasibility of adding material on complex shapes and/or geometry, or the possibility of achieving them with machining operations and, consequently, the necessity to add over-metal in the initial design of the part [46].

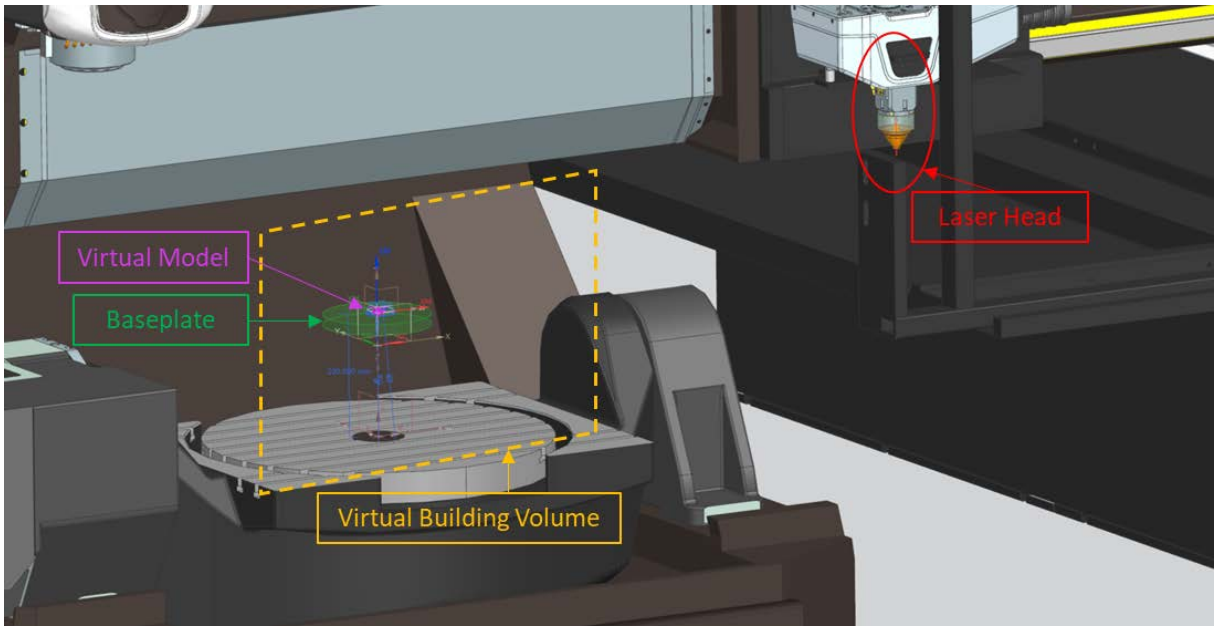

Figure 16: Virtual visualization by using Siemens NX of the Laser head, baseplate, the model to print, and the building volume with the required constraints to simulate the physical position in real Lasertec 65.

5.3 Toolpaths parameters

All the laser depositions in the Lasertec 65 are carried out following a G-Code file generated by Siemens NX that produces the toolpath to use [47]. This section describes the options available in Siemens NX for the design of a workpiece.

Considering that Lasertec 65 is a hybrid machine, the parameters are chosen according to the operations to do (additive or milling) and the characteristics of the model, such as the geometry, material (or materials, in case of multi-materials components), size, presence of channels, etc. Hence, the first step is choosing additive operation in Siemens NX. The second step concerns the choice of the deposition strategy (operation subtype in Siemens NX, Figure 17). The first four strategies are for deposition on planar surfaces, the following three are on rotary surfaces, the successive three for freeform, and the last two for tubes. For each of the described substrates, it was suggested the proper strategies according to the operation: coatings, the printing of thin walls, the printing of tubes, the printing of 3D structures.

Figure 17: Deposition strategies available in Siemens NX.

The first option was chosen in the present work, “Planar Additive Profile with ZigZag Fill”. Therefore, the software gives the opportunities to select many process parameters, the most important are:

- *Layer Thickness*: the height of the layer.
- *Overhang*: the amount of the deposited material that can flow beyond the edges of the solid model. This is useful, for example, to deposit enough material for later post-processing.
- *Minimum and Maximum Step-over*: the overlap between two adjacent passes, the complementary parameter of the well-known hatching distance (Figure 18). It can be set both in the percentage of the single track width or in millimeters.

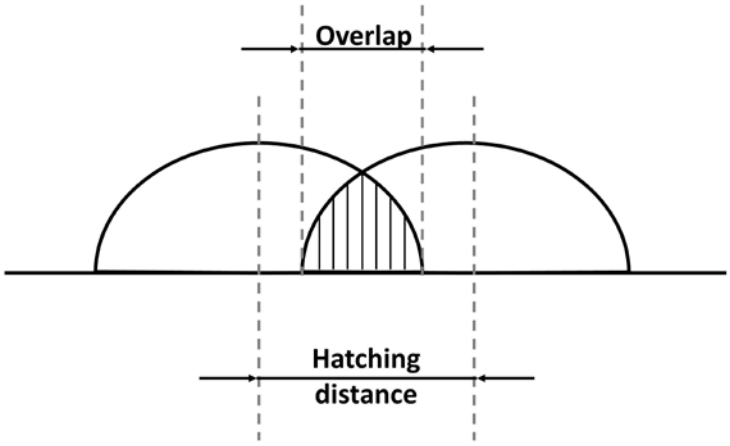

Figure 18: Overlap and Hatching distance.

- *Infill orientation*: inside the strategy selected, it is possible to choose the orientation of the laser passage in the layers, and so if unidirectional or in an alternate direction, respectively named Zig and ZigZag (Figure 19). The dot-lines represent the movement of the laser head with the beam laser turned off. The arrows represent the movement of the laser head during the deposition process, in particular, the orientation of the arrows indicates the deposition direction.

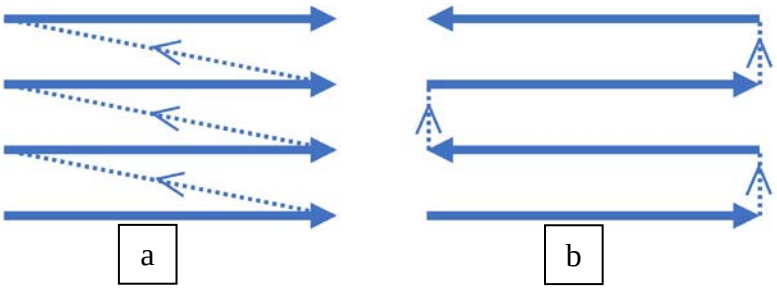

Figure 19: Deposition strategies in DLD process: a) Zig and b) ZigZag.

- *Infill Angle*: direction of the infill between each layer (in the present work, it was set equal to 90°, see Figure 20.
- *Pattern*: the possibility of choosing between the use of a contour deposition strategy or only the infill. Three options to select are given, i.e. Infill and Finish passes, Infill Only and Finish Passes Only.
- *Non-Deposition Moves*: settings of how the approach, the departure, and the fast movements should be made during the processing.
- *Gas Feed*: gas flow rate to move powder from the rotating disk to the nozzle and shielding gas velocity.

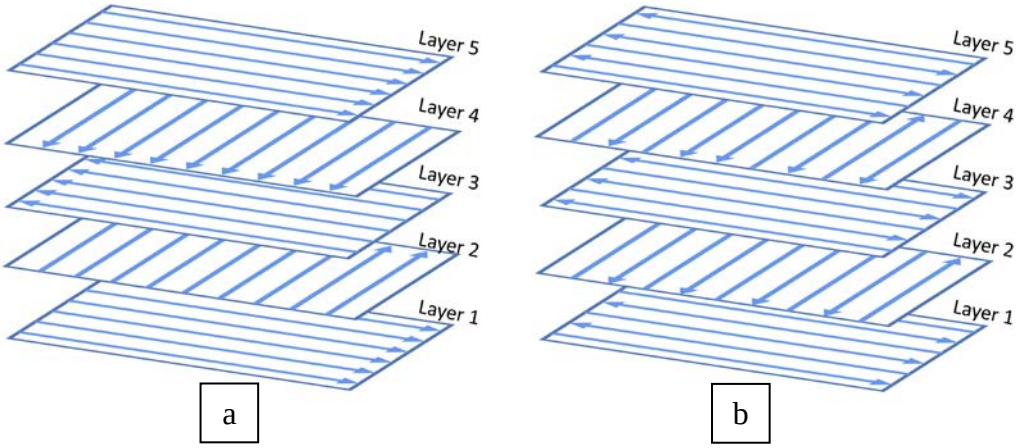

Figure 20: Example of Infill angle of 90° for a) Zig strategy and b)ZigZag strategy.

- *Stirrer Speed*: the speed of the stirrer located inside the hoppers.
- Powder Feed 1: the speed of the rotating disks for metal powder transport of the first cylinder (Figure 14), measured in revolutions per minute (rpm). After fixing the gas "Gas Speed" and the "Stirrer Speed", the speed of the disk must be calibrated to obtain the desired powder flow rate (in grams per minute).
- *Powder Feed 2*: the speed of the rotating disks for metal powder transport of the second cylinder (Figure 14). Siemens NX, indeed, allows changing material from model to model or even blending two powders to obtain composition gradients between the two materials.
- *Initial Laser Power*: the value of the power of the first layer. It is possible to set also the step-size, according to an increasing or decreasing trend, for the successive layer. Otherwise, the laser power is kept constant during all the process.

Chapter 6. Materials and characterization tests

6.1 Materials

The materials used in the DLD experimental campaign are stainless steel 316L and hot-work tool steel H13. They are used for the production of FGMs with tailored properties, such as a gradient in hardness or microstructures, but they are also a combination of great interest in the die and mold industry. Indeed, DLD can be used to both coat or repair the component in case of a premature failure of these high-added-value parts instead of replacing them. When upgrading an existing component with a new AM part, intermediate layers are commonly employed as buffer material. The optimization of the process parameters is needed to ensure the best adhesion and integration of the added part and the related properties.

6.1.1 316L Stainless Steel

One of the materials employed is AISI 316L, an austenitic stainless steel. In the family of stainless steels, shown in Figure 21, the austenitic ones represent the most used and produced category thanks to their excellent ability to resist aggressive environmental conditions, in particular to corrosion, combined with good mechanical properties [48], [49]. An element that greatly influenced the evolution of this category of steel was carbon; the first austenitic stainless steels contained an average percentage of carbon equal to 0.25% and due to this high carbon content, they were extremely sensitive to intergranular corrosion. To reduce or remove the occurrence of corrosive phenomena, they began to implement measures and modifications to the chemical composition, resulting in today's corrosion-resistant austenitic stainless steels. Currently, carbon usually is present in quantities ranging from less than 0.03% to over 1.0% in certain grades. Moreover, the austenitic stainless steel includes the iron-chromium-nickel grades corresponding to both standard AISI 300-series alloys and modified versions of these alloys. These alloys contain 16 to 26% Cr, 10 to 22% Ni, and small amounts of other alloying elements, such as molybdenum [50]. In particular, these improvements led to the origin of steel 316L; this differs from 316 for the even lower carbon content (around 0,03%), which allows the attenuation of the possible combination of carbon with chromium, which is, therefore, free to form the passivating layer of chromium oxide that provides protection from corrosion. The other elements present in the two alloys are equivalent.

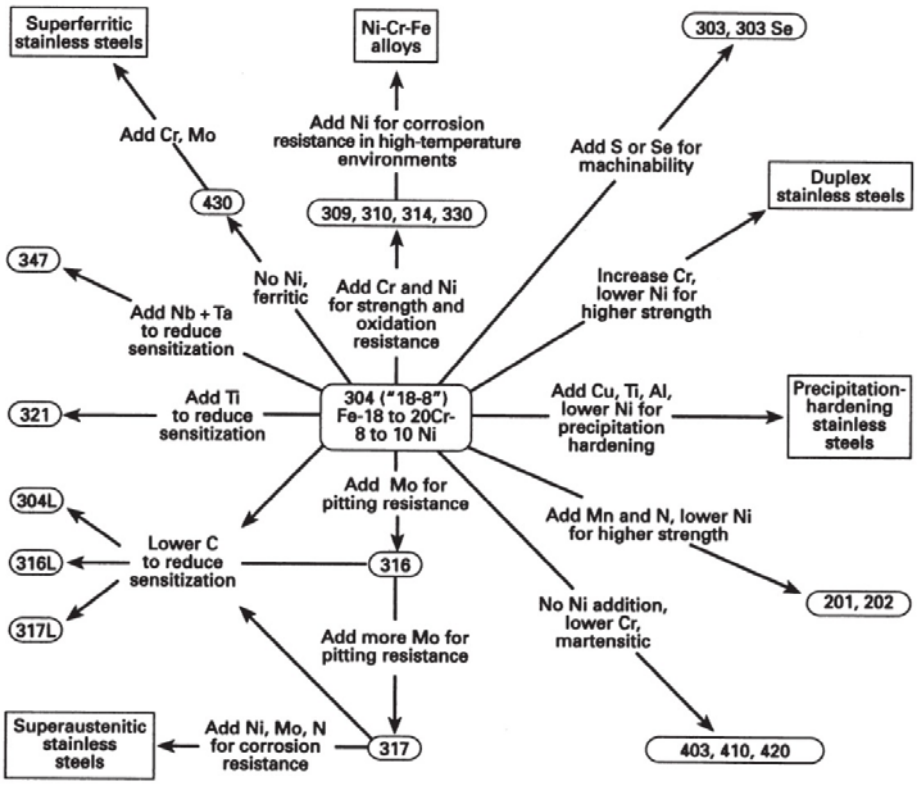

Figure 21: Composition connections in the stainless steel family of alloys [48].

6.1.2 H13 Tool Steel

Another material used for the depositions is the AISI H13, a hot-work tool steel. Tool steels belong to a particular category of steel alloys developed for the manufacture of tools, dies, and molds used to form and cut other steel alloys. They are also used for many nonferrous metals and, in some cases, nonmetals such as machinable ceramics and polymers. Considering a large number of available tool steel, they have been classified by the American Iron and Steel Institute (AISI) according to a prominent characteristic or function, for example, according to alloying (e.g. tungsten or molybdenum high-speed steels), application (e.g. cold-work or hot-work tool steels), or heat treatment (e.g. water-hardening or oil hardening tool steels) [51]. Figure 22 shows the main groups of tool steels and their associating letters. In general, tool steels can be described by a mixture of several properties: attainable hardness, which is the ability to achieve a certain level of hardness due to heat treatment; red hardness, which is the capability to preserve hardness at elevated temperatures; toughness, that is the ability not to fracture, chip, or crack when subjected to impact; and wear resistance, that is the capability to withstand the effects of erosion and abrasion.

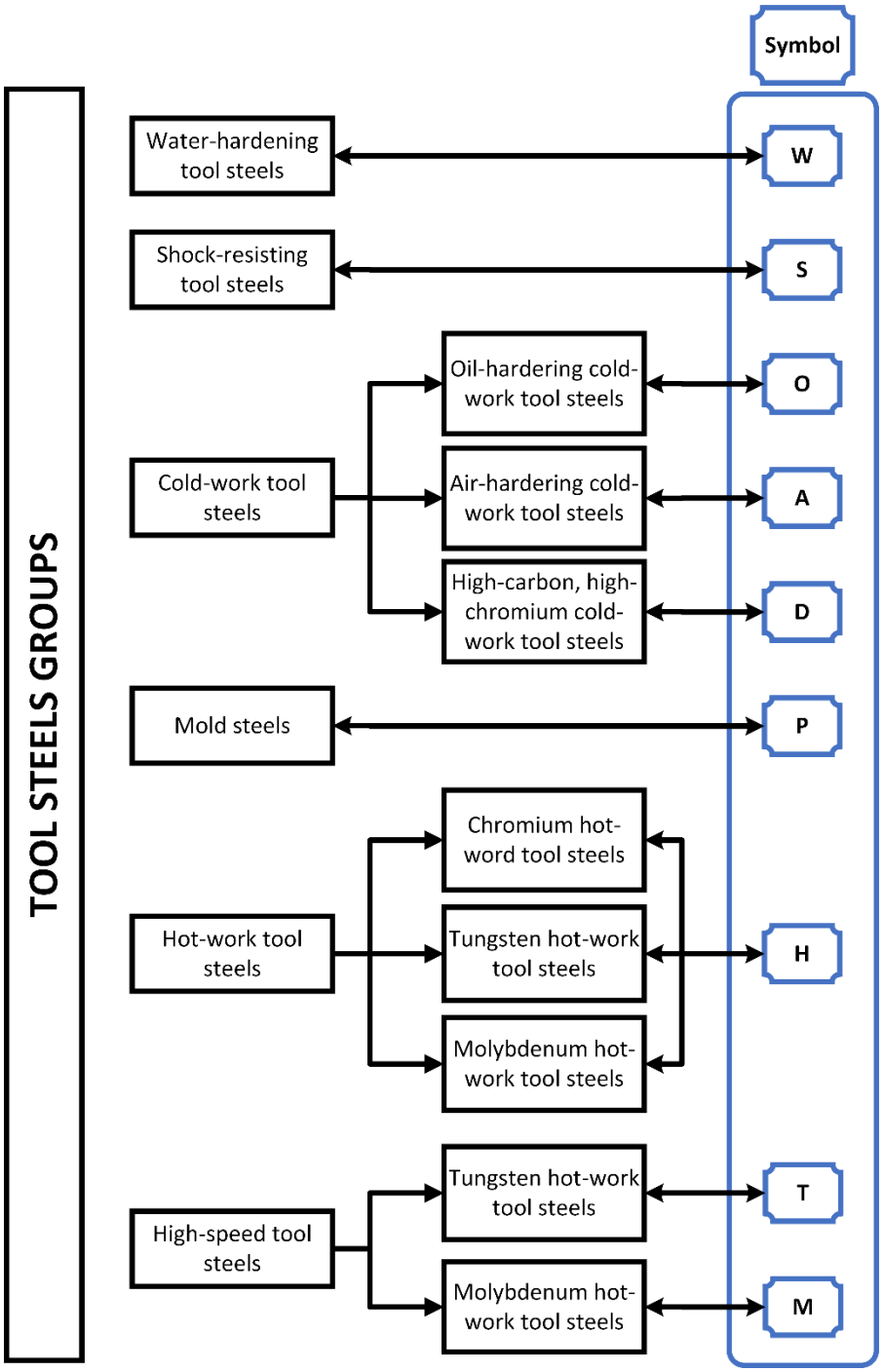

Figure 22: Main groups of tool steels and their identifying symbols.

In particular, hot-work tool steels are divided into three minority groups: chromium hot-work steels (from H10 to H19), tungsten hot-work steels (from H21 to H26), and molybdenum hot-work steels (from H42 and H43). Specifically, the material of our interest, H13, is a chromium hot-work tool steel that must have excellent resistance to high-temperature impact, high temperature softening and thermal fatigue. These requirements are achieved by using a medium-carbon content and relatively high concentrations of chromium and other strong carbide-forming elements.

6.2 Characterization tests

6.2.1 Confocal Microscopy

The instrument used for the surface metrological analysis of the samples is the Leica DCM3D laser confocal microscope (Figure 23). Confocal microscopy is getting more and more attention due to its capability to provide areal surface information in comparison to probe profilometry [52]. Townsend et al. [53] have given an excellent overview of the surface characterization problems related to metal-AM surfaces, explaining that the traditional surface characterization techniques used in the past are no longer suitable for metal-AM surfaces, or at least, not exhaustive enough to obtain the correct information about the surface state. On the basis of non-contact acquisition, some of the problems of stylus profilometry are considered, as well as the possibility of performing acquisition stacks and the availability of surface texture indicators. On this premise, Confocal Microscopy was used to obtain the necessary surface information presented in the following sections of Chapter 7 for the various issues of interest.

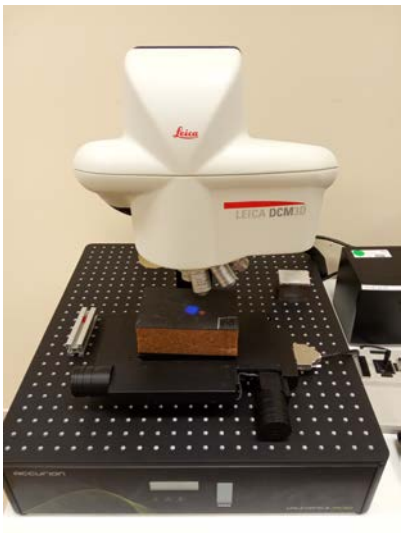

Figure 23: Leica DCM3D confocal microscope.

The acquired area changes according to the surface of interest. For the single tracks analyses (section 7.2), a 6x6 mm^2 area has been acquired; for the single layers analyses (section 7.3), a 10x10 mm^2 area has been acquired. Table 1 lists the specific parameters used to capture the surfaces of the samples, which required the technical specifications of the Leica DCM3D. That the z-scan (depth of the acquired surface, starting from the upper peaks) was set to a higher value than the actual expected values to ensure the complete acquisition of the surface and to compensate for possible tilts of the sample positioned under the lens and slight shape errors. In addition, a velocity value of 1x indicates that within the z-scan, each optical section plane has been considered to acquire the surface points.

Magnification	10x (x-y resolution: 0.94 µm, z resolution: 0.47 µm)
Z-scan	1800 µm
Speed	1x
Light	Auto

Table 1: Leica DCM3D measurement set-up used for single tracks and single layers analyses.

6.2.2 Scanning Electron Microscopy/Energy Dispersive X-ray Spectroscopy

Scanning Electron Microscopy (SEM) has been used in order to study the microstructures of the powders employed for the depositions, to find defects (such as irregular shapes or agglomeration of the powders, as well as porosities and cracks regarding the cross-sectioned samples), and to study the influence of the process parameters on the microstructure evolution of the samples. With this aim, micrographs at different magnifications have been acquired using a Hitachi TM3000 SEM, reported in Figure 24. Moreover, the SEM was equipped with a SWIFT ED3000 probe for Energy Dispersive X-ray Spectroscopy analysis (EDX), used to analyze the chemical composition, and particularly useful for the multi-material analyses (see section 7.5).

Figure 24: Hitachi TM3000 Tabletop SEM.

6.2.3 Optical Microscopy

Optical Microscopy (OM) analyses have been performed on the samples to study the influence of the process parameters on the DLD depositions. Moreover, it has been employed to find specific geometrical characteristics of the single tracks by taking measurements on the images acquired using ImageJ® software (a more detailed explication is given in section 7.2). After preparing the samples for cross-sectional observation, which has been carried out according to the standard metallographic procedure [54], optical macrographs have been taken at 200x magnification for each of the studied

samples. An optical microscope Zeiss Axioplan 2 has been used to perform the analyses (see Figure 25).

Figure 25: Zeiss Axioplan 2 Optical Microscope.

6.2.4 Vickers Microhardness

Vickers microhardness analyses have been performed in each step of the optimization process of DLD parameters. In the Vickers hardness test, a Vickers indenter, i.e a square base diamond pyramid Vickers hardness indenter, was employed to apply a determined force, for a dwell time of about 15 seconds, according to ASTM E92-82 [55]. After the indentation is completed, the resulting indentation is analyzed optically to measure the lengths of the diagonals to determine the size of the indentation. The Vickers microhardness (HV) is, indeed, calculated according to the following formula:

$$HV=1.854\left(\frac{F}{d_1 * d_2}\right) \quad (1)$$

Where F is the applied loads, measured in gram force (Kgf), d_1 and d_2 are the diagonal lengths measured in millimeters (mm). The microhardness machine used has been a Tecmet 2000, shown in Figure 26.

Figure 26: Vickers Microhardness instrument: Tecmet 2000.

6.2.5 Mechanical analysis

Three-point bending tests have been carried out by using a Galdabini QUASAR 50 testing machine equipped with a 50 kN load cell, shown in Figure 27. Tests have been carried out at room temperature and with a testing speed set to 1 mm/min. According to international standards, the software associated with the Galdabini machine, LabTest™, allows for programming the tests.

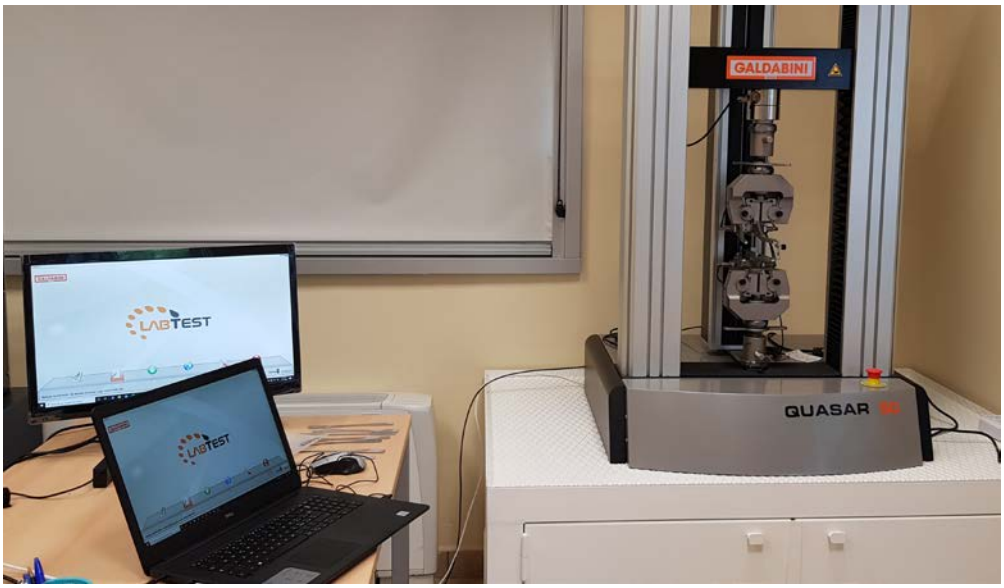

Figure 27: Universal testing machine Galdabini QUASAR 50.

6.2.6 Chart of the performed tests

For the sake of clarity, all the tests performed are presented synthetically in Table 2 below. The purpose of the table is to highlight in which case a particular characterization test was performed.

	Test Performed				
Samples	Confocal Microscopy	SEM-EDX analysis	Optical Microscopy	Microhardness analysis	Mechanical analysis
Metal Powders		X			
Single Tracks	X	X	X	X	
Single Layers	X	X	X	X	
Single Walls		X		X	
FGM structures		X	X	X	X

Table 2: Chart of the performed tests.

Chapter 7. Optimization of DLD process for tailored and hybrid structures

The direct laser deposition process consists of the deposition of metallic powder on a substrate, involving many transport phenomena [56], [57] that affect the result and are related to the process parameters. It is necessary to set them appropriately in order to achieve the desired final requirements. It is worth saying that DLD deposition is an additive manufacturing technology that is usually based on prototype machines or hybrid systems composed of parts from different manufacturers, and also in the case of a commercialized machine, suggestions of process parameters to use are provided for a limited number of materials. Due to the lack of standardization, optimization of process parameters is often a required step to develop an efficient build process.

In the literature, it was concluded that there are four most influent process parameters [58]–[62]:

- Laser Power [W],
- Powder Feed Rate [g/min],
- Scanning Speed [mm/min],
- Spot Size Diameter [mm].

The fourth parameter has not been considered since, for the DMG MORI LASERTEC 65, both the laser length and the laser spot size are fixed, respectively, set to 13 mm and 3 mm. The study of the 3D printing process has been organized and will be presented following a criterion of increasing complexity: the influence of the other three parameters has first been investigated, successively also the effect of the overlap distance and the scan strategy adopted has been included in the optimization process of the parameters. Figure 28 shows the workflow used to find the process parameters for three-dimensional depositions of FGM structures. Moreover, due to the lack of scientific rigor in the methodology to characterize single tracks and single layers, processing guidelines are provided in this section.

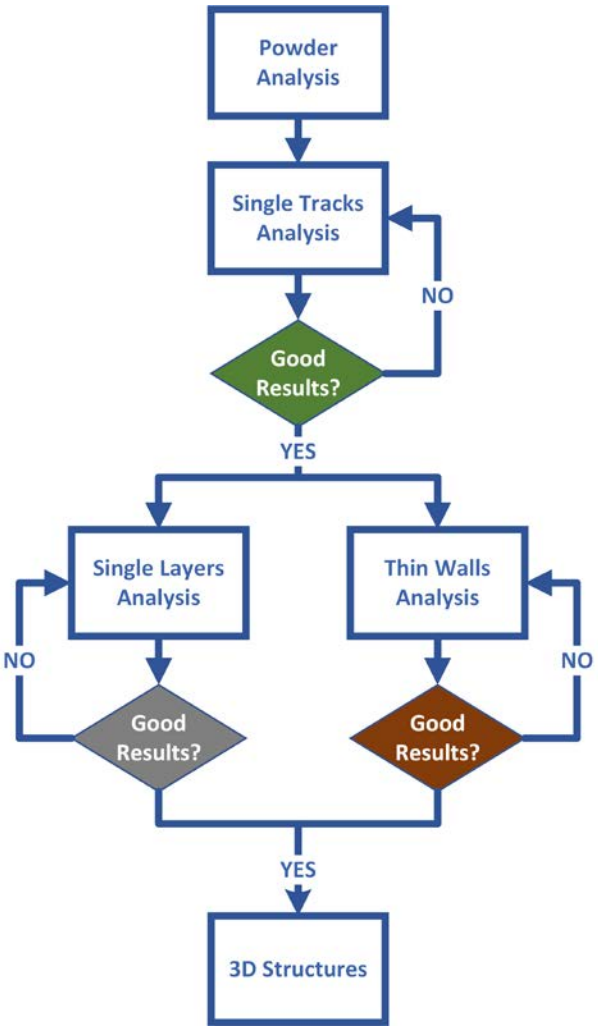

Figure 28: Scheme of the optimization workflow of the process parameters in DLD technology.

The study of the correct process parameters to print 3D structures begins with powder analyses. Indeed, the characterization of the material is crucial to reach good results in terms of mechanical properties, microstructure, geometrical accuracy, and in the case of FGM, also in terms of miscibility of materials and absence of internal defects [63]–[65].

The analyses of single tracks represent the successive step. The results of the STs analysis can be considered good if they satisfy the geometrical and hardness requirements, in combination with the absence of macroscopic defects. Specifically, STs should reach hardness values, at least, comparable to those obtained in literature with conventional and AM processes, and provide the best trade-off between geometrical characteristics -wetting angle major than 100°, aspect ratio major than 5, dilution between 10% and 30%, shift minor than 50µm -, described with major detail in following sections.

Then, according to the final product to be built, the study continues with single layers analyses (if the purpose is to print bulk 3D structures) or with thin walls analyses (if the final item is a thin-wall structure). The first case is the one of interest; once again, the results of the SLs analysis can be considered good if they satisfy the hardness, geometrical, and defect-free requirements. Specifically,

the waviness should be as low as possible in combination with hardness at least comparable to those obtained in literature with conventional and AM processes.

At this point, the printing of 3D structures represents the final step to assess the validity of the outcomes of the previous analyses and confirm the proper management of the process parameters.

7.1 Feedstock materials

In this work, the feedstock material is represented by metal powders, which for AM are typically manufactured and commercialized by suppliers starting from well-established methods such as water, gas or plasma atomization, hydride-dehydride process, mechanical grinding and electrolytic reduction of metal oxides (it is possible to see a detailed list in Figure 29) [41], [66]–[68]. The choice of a particular manufacturing process depends mainly on the desired powders characteristics (shape, dimensions, microstructure, chemical composition), as well as on the reactivity of the powder with the atmosphere and the resulting formation of oxides, which adversely affect the weldability of the powder particles and, consequently, the density and mechanical properties of the finished parts [69], [70]. In the case of the most oxidation-sensitive alloys, such as titanium and aluminum, even the choice of atomization gas used has an impact on the powder properties, especially on the microstructure. Moreover, the effects of powder properties on the macro level, such as shape and size distribution, are different according to the AM process used. In general, in all these AM technologies, a spherical powder form is preferred for the starting material, but in particular, powder shape and dimensions influence the layer distribution, flowability and powder packaging above all in the powder bed technologies [71]. On the other hand, some researchers have highlighted that DED processes, such as DLD, are less sensitive to non-spherical powder, depending on the powder feeder used and the powder loading in the carrier gas, where even irregular particulate can be smoothly fed into the laser melting zone [72], [73] .

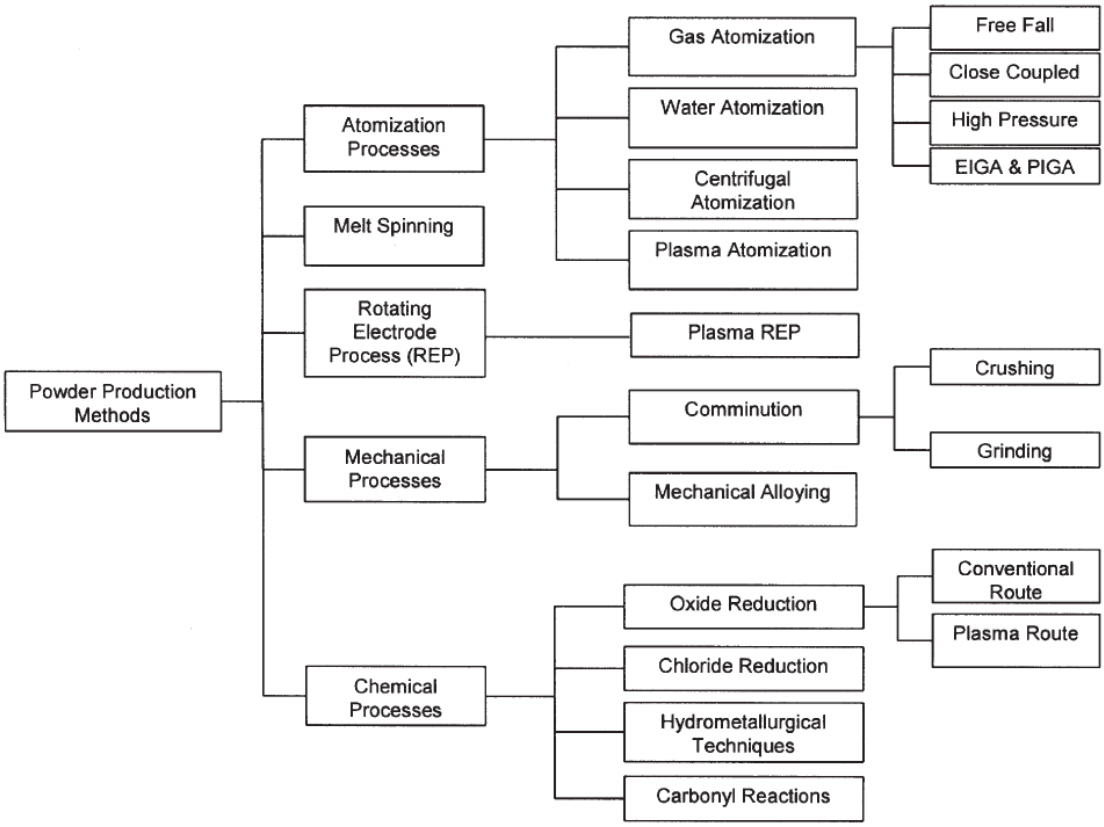

Figure 29: Classification of powders production processes [66].

7.1.1 Analysis of 316L powders

In this work, one of the materials employed to print FGMs is gas-atomized 316L stainless steel powders provided by Voestalpine Böhler Welding GmbH. The nominal chemical composition of the pre-alloyed SS powder is given in Table 3.

C	Si	Mn	Cr	Mo	Ni	Fe
0.03	1.0	2.0	16-18	2.0-3.0	10-14	balance

Table 3: Chemical composition (in wt%) of 316L stainless steel powder.

The powder particle size that can be processed in Lasertec 65 varies from about 50 μm to 150 μm. The provided 316L powders granulometry ranges from 45 μm to 105 μm (D10=45, D50=71, D90=105), characterized according to the ASTM B822-17 [74]. This different size can affect how the powder is transported to the nozzle and the amount of energy required to melt the particles – since the surface/ volume ratio changes considerably [75]. Another critical factor that can influence the flowability and the absorbed energy by the powders is the shape of the single particle.

For this purpose, powders have been characterized according to the ASTM F3049 [76], starting from a morphological characterization. Indeed, in Figure 30 is possible to note the SEM micrographs of

316L powders at different magnifications to appreciate both morphology and defects [77]. In this case, most of the powders are spherical, although some irregular particles have been depicted. Some defects are highlighted by the red arrows in the SEM image on the right of Figure 30, such as open pores and smaller particles embedded in the bigger ones.

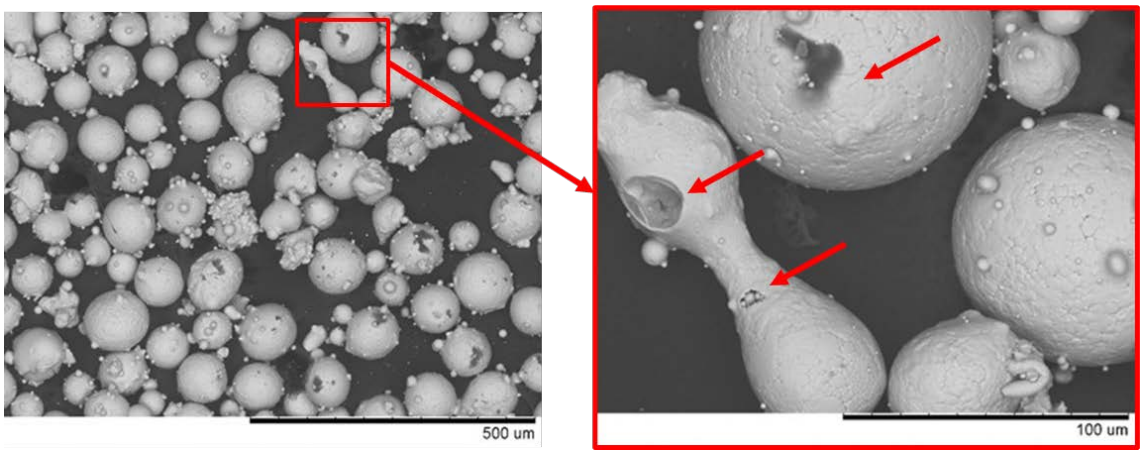

Figure 30: SEM images of 316L powders used for depositions at different magnifications, 500X on the left and 1000X on the right.

In particular, in Figure 31, other imperfections are highlighted by red arrows: adhesion phenomena on the left, and voids on the right.

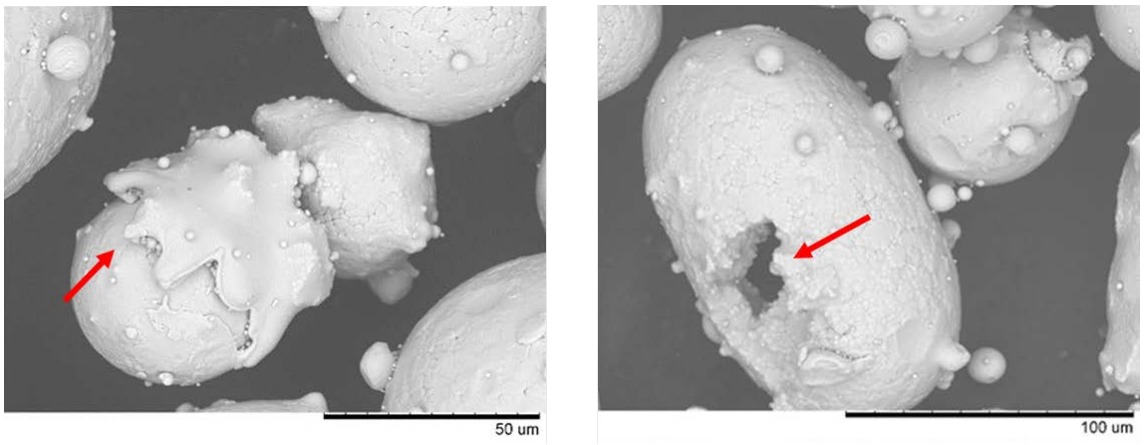

Figure 31: Micrographs of 316L powders at different magnifications showing several defects: adhesion phenomena (left), internal voids (right).

Then, an EDX analysis was conducted, and it was observed that the powder particles were chemically homogeneous.

In addition, powders have been mounted, lapped, and polished with a custom-made metallographic preparation for a cross-section investigation. The near-spherical shaped geometry is also evident in Figure 32, in which the cross-section of 316L single powder is shown. The microstructure is made of equiaxed grains, typical of gas-atomized steel powders, and an internal porosity can be observed.

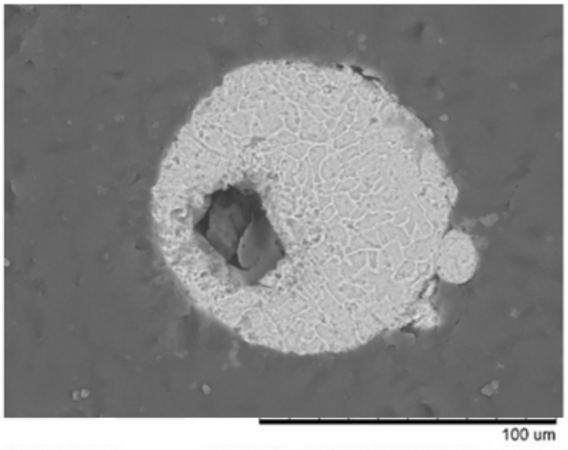

Figure 32: Micrographs of the cross-section of 316L single powder.

7.1.2 Analysis of H13 powders

The other material of interest is the H13 hot-work tool steel. Gas-atomized AISI H13 powders are provided by Voestalpine Böhler Welding GmbH. The nominal chemical composition of the above-mentioned steel powder is given in Table 4.

C	Si	Mn	Cr	Mo	V	Fe
0.35	0.8-1.2	0.2-0.5	5-5.5	1.1-1.75	0.8-1.2	balance

Table 4: Chemical composition (in wt%) of H13 tool steel powder.

The particle size ranges from 75 μm to 151 μm (D10=75, D50=107, D90=151). The powders are slightly larger in size than those analyzed in section 7.1.1, promoting better mixing when powders are deposited together.

According to ASTM F3049 [76], also the H13 powders have been characterized. The shape of the particles can be observed in the SEM image, Figure 33, on the left. The majority of the powders are rounded, even if it is possible to note some particle agglomerations, off-spherical shapes, and acicular powders, visible in detail in Figure 33, on the right.

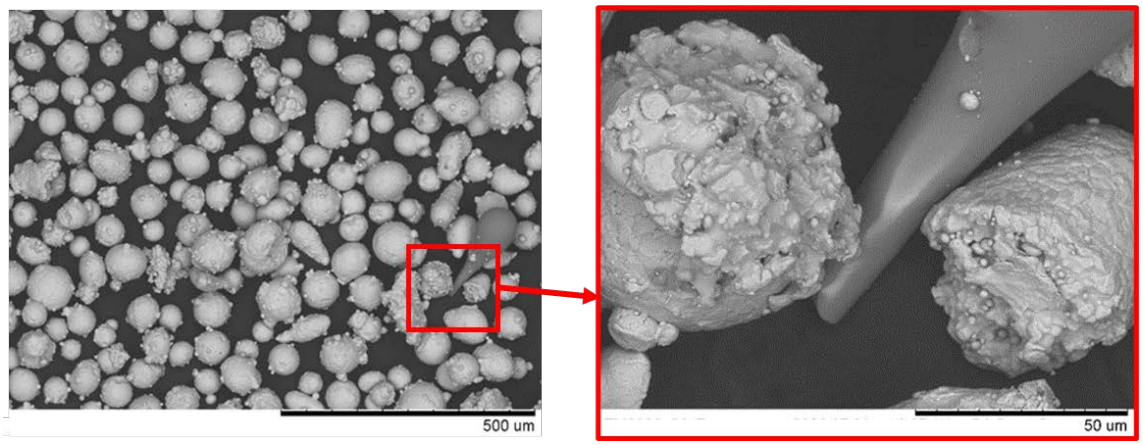

Figure 33: SEM images of H13 powders used for depositions at different magnifications, 500X on the left and 1500X on the right.

Other defects have been found during the morphological analysis, such as fragmented particles, irregular shapes, and surface cracks, as indicated by red arrows in Figure 34.

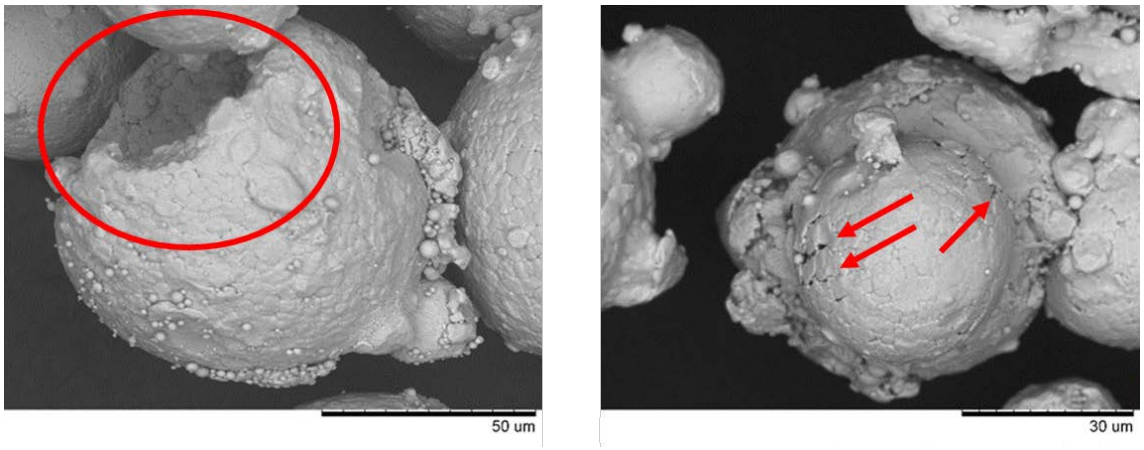

Figure 34: Micrographs of H13 powders at different magnifications showing several defects: fragmented particle (left), surface cracks and agglomerations (right).

Moreover, in the SEM examination, some darker powders have been noticed (Figure 35), and a punctual EDX analysis has been conducted. The point analyzed is indicated by the red arrow and by "Spectrum 1" in the figure), which has pointed out that they are rich in silicon.

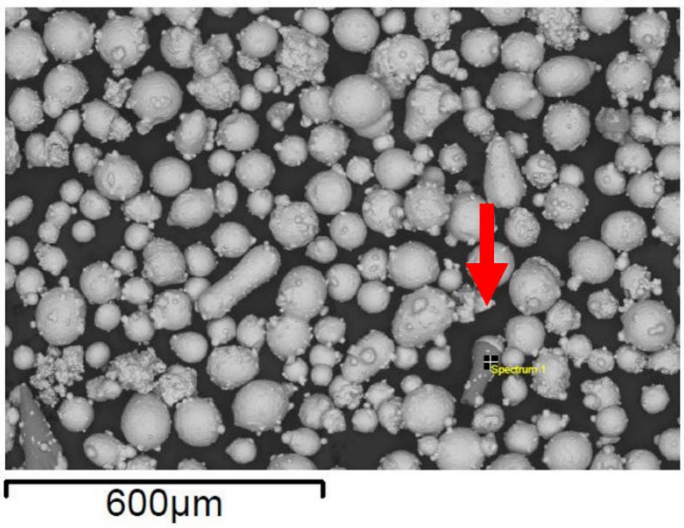

Figure 35: SEM image of H13 powders for punctual EDX analysis on darker particles.

Finally, powders have been mounted, lapped, and polished with a custom-made metallographic preparation. Figure 36 shows the cross-section of H13 particles. The geometry is similar to the 316L one. Also in this case, the microstructure is made of equiaxed grains, typical of gas-atomized steel powders.

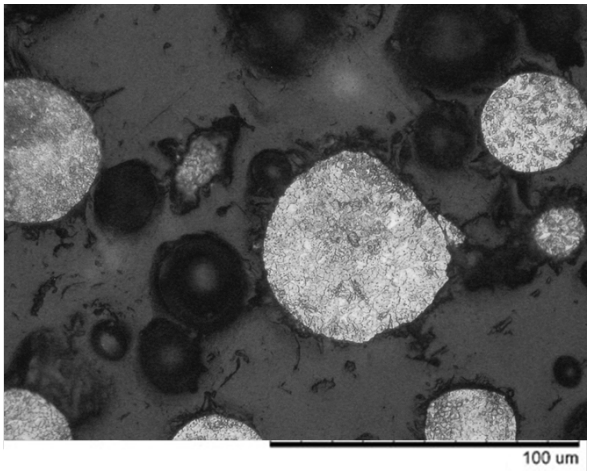

Figure 36: Micrographs of cross-sections of H13 single powders.

7.2 Single tracks

The process parameters can affect the quality of three-dimensional printed parts or cladding parts. As introduced in a previous section, there are many parameters involved in the DLD process, such as laser power, powder feed rate, scanning speed, carrier gas flow, preheat temperature, working distance, etc [56], [57], [78]. The correct use of all these parameters is essential to achieve a good deposition; nevertheless, the first three are the most relevant and provide the largest windows for changes and improvements. As declared by many authors, such as Bax et al. or Kapil et al., the first stage for optimizing the process parameters map is the assessment of single tracks for the material of interest [58], [79].

For the AISI 316L, the process parameters provided by the manufacturer have been employed. On the other hand, no suggestions have been supplied to deposit AISI H13 for the DMG MORI Lasertec 65. Although H13 has received great attention worldwide as one of the most attractive materials in hot-forming applications (e.g. die casting tooling, extrusion dies), published data on the parameters to process H13 are still insufficient [80]–[82]. Mazumder et al. have highlighted that it is possible to reduce the time for die production by 40% with the use of the DLD process and consequently save costs in the die production industry. He is one of the first researchers to confirm the processability of H13 by means of DLD [80]. Recently, Wołosz et al. have investigated the influence of technological parameters, providing that geometry, microstructure, hardness and deposition efficiency are dependent on the LENS technological parameters, in particular laser power, laser spot diameter, scanning velocity and powder feed rate [83]. Amirabdollahian et al. have investigated the influence of post-process heat treatment on the as-built DLD H13 in order to obtain a redissolution of carbides [84]. Moreover, stemming from the outcomes of previous research work [85], in which it is clear that changing the AM machine and using the optimum in terms of process parameters provided by the manufacturer, the results are different, this gap of knowledge is reinforced by the lack of research works on the Lasertec 65 about the deposition of H13. In this section, an experimental campaign has been conducted in order to fill this gap, providing indications on the process parameters to be used and using a 316L substrate to investigate the behavior of H13 on 316L. In addition to the single tracks, also single layers, thin walls, and cubes have been analyzed in further sections.

7.2.1 Experimental campaign

The influence of four levels of laser power (P), three levels of powder feed rate ($\dot{m}_p$) and two levels of scanning speed (v) have been investigated. The values of the process parameters investigated have been chosen on the basis of preliminary experiments in order to identify the range within which the DLD H13 can be performed. These process windows are shown in Figure 37 and Figure 38. On the

other hand, the following parameters remained constant throughout the experiments: the spot diameter of 3 mm, focal length of 13 mm, high purity Argon gas that has been used for both career gas and shielding gas with a flow rate of 5 l/min and 6 l/min, respectively.

The laser power levels have been: 1400 W, 1600 W, 1800 W and 2000 W. For each laser power value, the powder feed rate has been varied from 9 to 15 g/min, with a step size of 3 g/min. Every combination of these values of P and $\dot{m}_p$ have been deposited with a scanning speed of 1000 mm/min and 1200 mm/min.

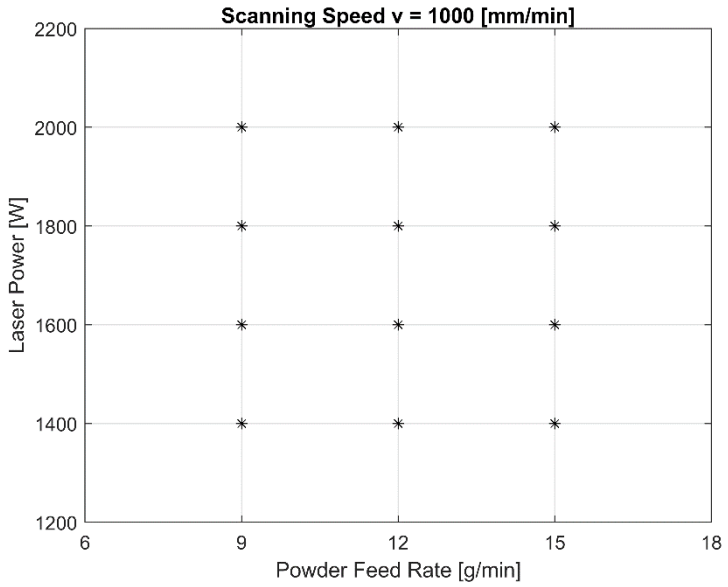

Figure 37: Investigated process parameters windows for processability of H13 via Direct Laser Deposition, keeping scanning speed constant at 1000 mm/min.

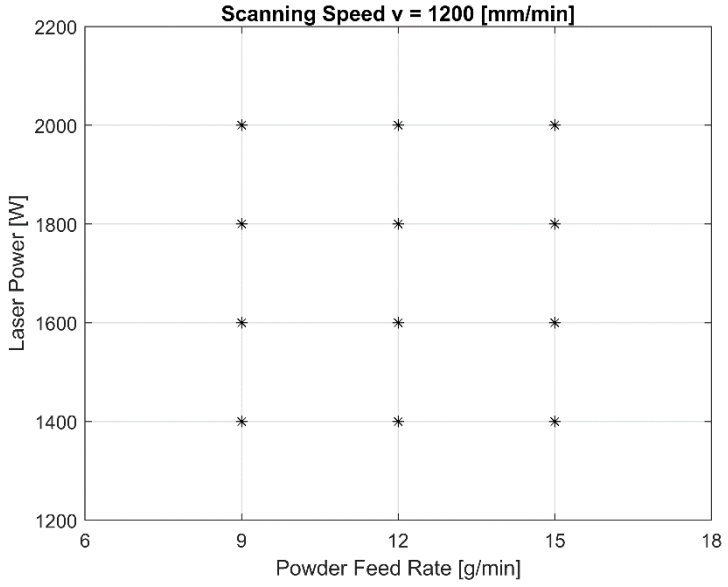

Figure 38: Investigated process parameters windows for processability of H13 via Direct Laser Deposition, keeping scanning speed constant at 1200 mm/min.

7.2.2 Methods

7.2.2.1 H13 single tracks fabrication via DLD process

Siemens NX has been employed to produce the G-code for depositions in Lasertec 65 (Figure 39). The substrate used is 316L stainless steel with a dimension of 200x80x20 mm^3. It has been sandblasted and degreased with acetone before the deposition process.

Figure 39: Laser head of Lasertec 65 during the first H13 single track deposition on 316L substrate.

Then, 24 different single tracks have been deposited adjacently, 25 mm in length and with an inter-bead distance of 10 mm, varying parameters as shown in Table 5. In the above-mentioned table, *ST no.* represents the order of the single tracks; the *DLD order* is the sequence in which they have been deposited in the Lasertec 65.

ST no.	**DLD order**	**Parameters**			**ST no.**	**DLD order**	**Parameters**		
		P [W]	**V [mm/min]**	**$\dot{m}_p$ [g/min]**			**P [W]**	**V [mm/min]**	**$\dot{m}_p$ [g/min]**
1	22	1400	1200	15	**13**	21	1400	1000	15
2	3	1400	1200	12	**14**	7	1400	1000	12
3	24	1400	1200	9	**15**	20	1400	1000	9
4	12	1600	1200	15	**16**	15	1600	1000	15
5	16	1600	1200	12	**17**	14	1600	1000	12
6	11	1600	1200	9	**18**	18	1600	1000	9

7	9	1800	1200	15	**19**	6	1800	1000	15
8	23	1800	1200	12	**20**	1	1800	1000	12
9	5	1800	1200	9	**21**	17	1800	1000	9
10	10	2000	1200	15	**22**	2	2000	1000	15
11	19	2000	1200	12	**23**	13	2000	1000	12
12	4	2000	1200	9	**24**	8	2000	1000	9

Table 5: Run order and parameter settings of H13 single tracks.

7.2.2.2 Characterization

Single tracks have been cut and cross-sectioned via electrical discharge machining (EDM) in the middle of the straight line to ensure the analysis of the section in which the process is stable. Then, the specimens were hot mounted in an acid-proof resin. The metallographic preparation has included water-cooled silicon carbide paper (200 mm diameter) for the grinding stage; the grit size selected also depends on the technique used to generate the cut surface. The used grit sequence was 240, 320, 400 and 600-grit, with a grinding time of 2 minutes. Then, specimens were polished in three stages, with 9, 6 and 1 μm diamond abrasive suspension to the polishing cloths. The polishing time was 4 minutes [54].

Microstructure characterization has been performed on polished metallographic cross-sections after chemical etching with modified Vilella's reagent (ethanol, picric acid and hydrochloric acid), employing OM and SEM. Microhardness Vickers measurements have been conducted on the metallographic cross-sections with a dwell time of 15 s, as suggested by the standard ASTM E92-82 [55].

7.2.2.3 Theoretical background

In this section, the effect of P, v and $\dot{m}_p$ on the following ST geometrical features have been evaluated: the clad height (h), the penetration depth (d), the width of the track (w) [86], and the wet angle (α) [87] (illustrated in Figure 40), dilution (DIL) (explained in the following), and aspect ratio (AR), i.e. the width to height ratio [88]. A confocal microscope (section 6.2.1) has been employed to evaluate the height before STs were cross-sectioned. The other geometric characteristics, i.e. *d* and *w*, have been determined by the measurements performed on the cross-section with the software ImageJ™. The α angle has not been directly measured on the photographs of the cross-sections of the samples since this method leads to systematic errors and considerable dispersion of data, as declared by Shayanfar et al. [59], but five arbitrary profiles have been chosen to be analyzed using the software Leica Map™ after confocal acquisitions.

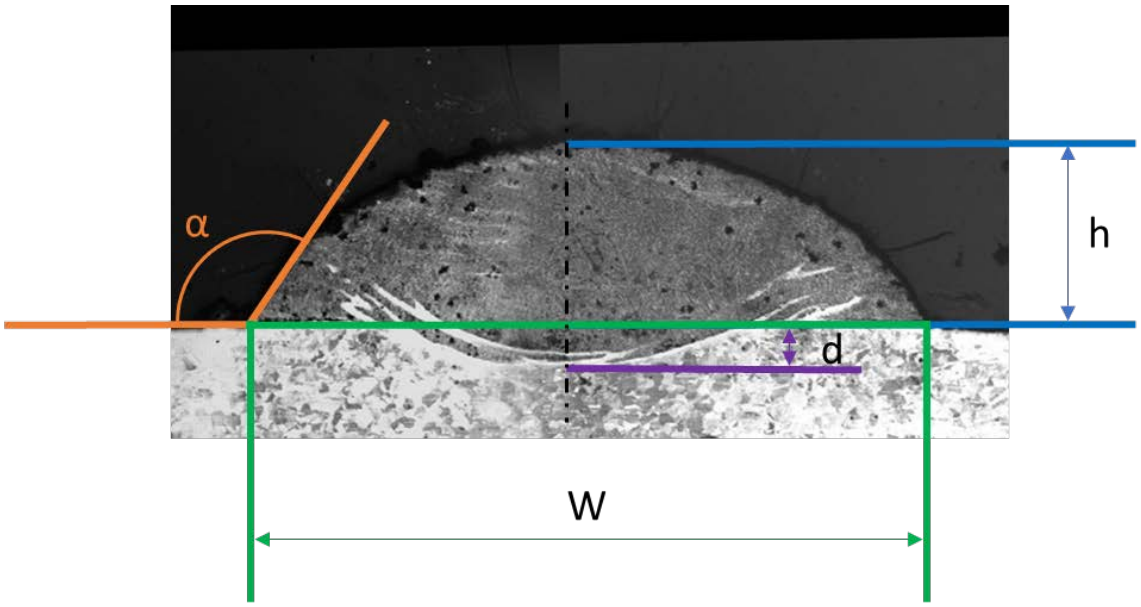

Figure 40: Geometric characteristics of a single track, h: height of the ST deposition, w: width of the ST deposition, d: penetration depth, α: clad angle.

The dilution is a crucial parameter that affects the chemical composition of a cladding [89], as the quality of the bonding [90], and it is calculated as the ratio of the transverse cross-sectional area of melted material under the base metal surface (A_m) to the sum of A_m and the melted material above the base metal surface (A_c) [91]. The recognized models of Carslawand Jaeger [92] and Rosenthal [93], stemming from the evaluation of the deposited cross-sectional material, suggested to approximate it as an ellipse with a variable aspect ratio, which is considered a more favorable approximation than a circle or a rectangle. In particular, Bhardwaj et al. have explicitly suggested the use of the following simplification [86]:

$$dilution = \frac{A_m}{A_m + A_c} = \frac{d}{d + h} \qquad (2)$$

Where $A_m=\pi wd$ and $A_c=\pi wh$. A new approach is proposed in the present work, considering two novel geometrical characteristics: the shift (s) and the actual width of A_m (w'), as illustrated in Figure 41. Specifically, it has been assessed that under the base metal surface (indicated by the dotted line in the figure), the molten material was not situated at the center of both the upper and down the surface line. Consequently, the distance between the center of A_c and the center of A_m has been evaluated and named shift. Moreover, it has been considered that also the width of A_m did not always correspond to the width of A_c, consequently also *w'* has been calculated.

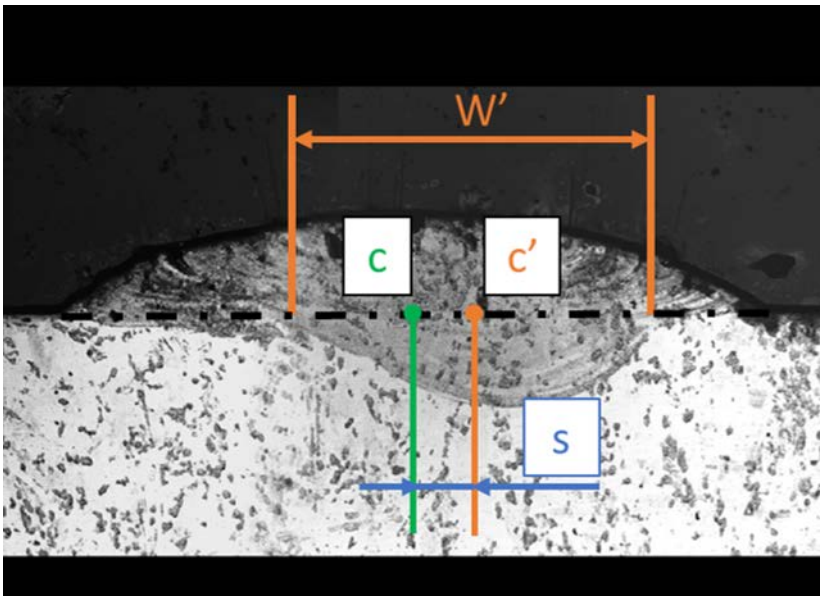

Figure 41: New geometric characteristics of a single track, w': width of A_m, s: shift of the centers of the melting material.

The new dilution formula (3) has been used, based on the previous considerations and different from equation (2):

$$dilution\ [\%] = \frac{A_m}{A_m + A_c} * 100 = \frac{w'd}{w'd + wh} * 100 \qquad (3)$$

where $A_m = \pi w' d$ and $A_c = \pi w h$.

7.2.3 Results and discussion

The first step in obtaining high quality results in terms of material deposition is to examine the individual traces. Single tracks with poor adhesion to the substrate, strong convex shape, or too high dilution cannot be used [58], [78]. The first result is that all investigated process parameters for the deposition of H13 led to 24 successful depositions. As shown in Figure 42, no one has peeled off during or after the DLD process. Each line is numbered according to the ST order described in Table 5.

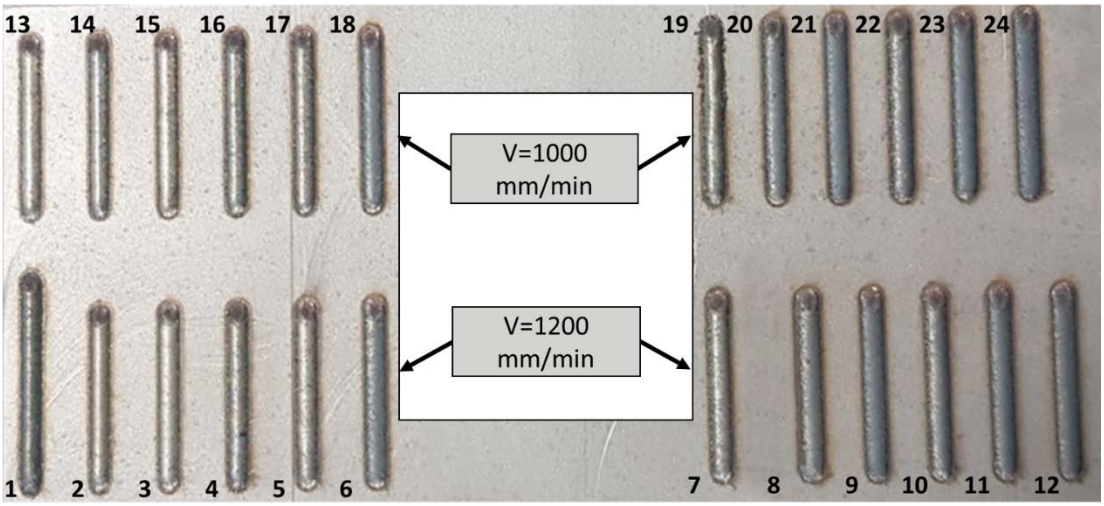

Figure 42: DLD H13 single tracks.

The cross-sections obtained according to the metallographic procedure described in section 7.2.2.2 are shown in Figure 43 and Figure 44. The single tracks in Figure 43 were produced keeping constant the scanning speed at 1200 mm/min, while the ones in Figure 44 with the fixed scanning speed set at 1000 mm/min.

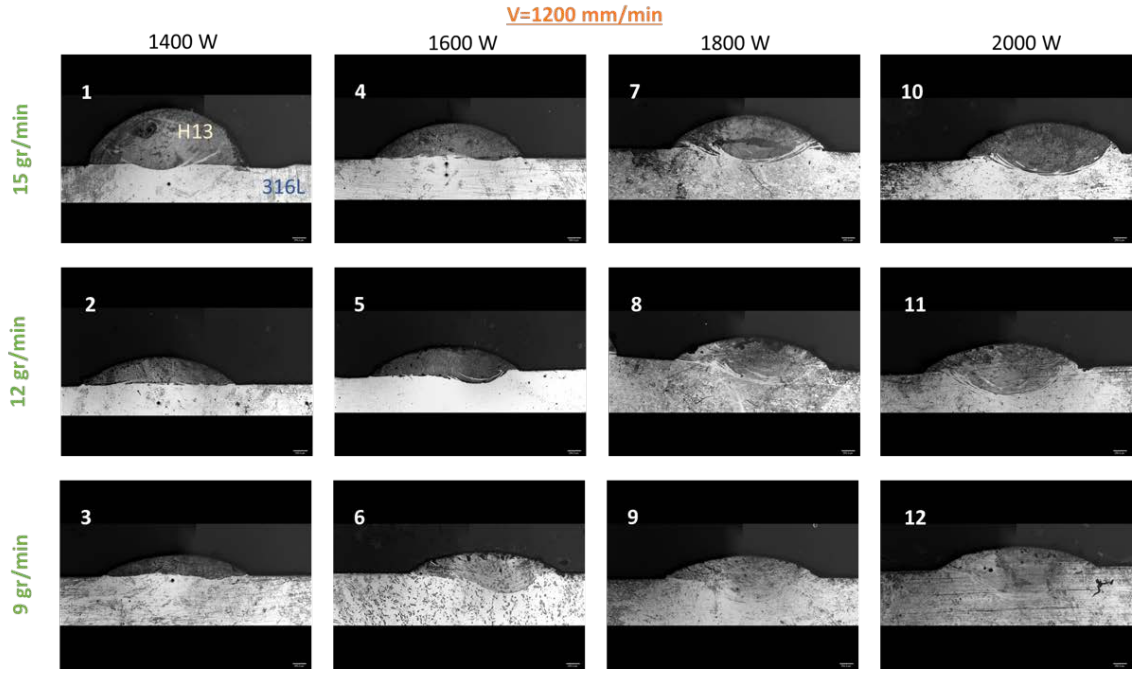

Figure 43: Cross-section of H13 single tracks deposited with a constant scanning speed of 1200 mm/min.

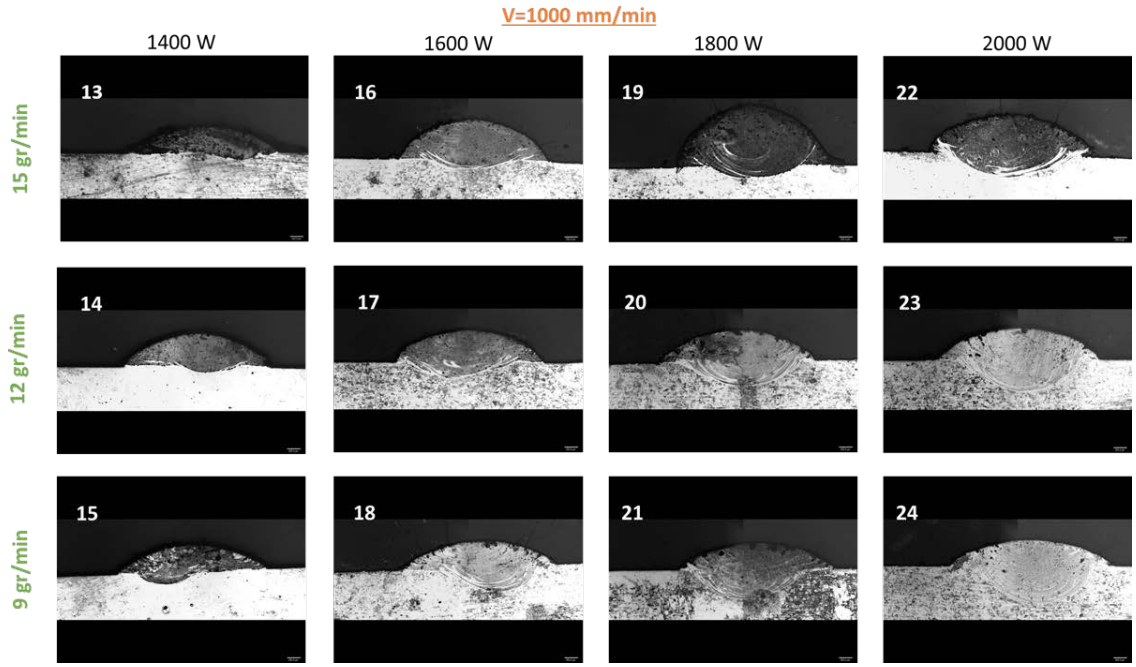

Figure 44: Cross-section of H13 single tracks deposited with a constant scanning speed of 1000 mm/min.

7.2.3.1 Geometrical analysis

The first stage of this section's characterization consists of STs qualitative inspection by means of OM, as suggested by Mazzucato et al. [62]. In the present experimental campaign, all the combinations of the process parameters led to acceptable results that ensure both proper metal bead formation and continuous deposition, as shown in Figure 42. The STs have exhibited stability, and no discontinuities have been found, also in the case of high values of P and low v. This is an essential step, considering that the wavy and irregular edge profile of the STs can affect the successive step, represented by the deposition of single layers composed of closer STs. Indeed, the presence of spattering phenomena and/or lack of fusion can bring internal defects (such as cracks or pores) and inaccurate shapes (for example, due to over-depositions). Moreover, cracks have not been observed during the analysis of STs.

After a qualitative analysis, a quantitative analysis has been carried out. The results in terms of height, width, depth, width' and wet angle are revealed in Table 6. The laser power has mainly influenced ST depth and width, reaching the *d* and *w* maximum values at 2000 W and 1200 mm/min, with 9 g/min. On the other hand, as declared by Bax et al. [58], the clad height generally increases with the increasing powder feed rate. In relation to the wetting angle, Costa et al. [87], in their work, have also studied the influence of the wetting angle, assessing that to avoid porosity through the overlapping clad tracks for the formation of layers, the α angle (Figure 40), must exceed 100°. Also Shayanfar et al. [59] have asserted that to obtain high-density laser depositions, it is required to have a wetting

angle over 100°. In all the 24 STs obtained in this experimental campaign, the wetting angle α is major than the inferior limit suggested by the literature, as it is possible to note in Table 6.

ST no.	**Parameters**			**Outputs**				
	P	**V**	$\dot{m}_p$	**h**	**w**	**d**	**w'**	**α**
	[W]	**[mm/min]**	**[g/min]**	**[µm]**	**[µm]**	**[µm]**	**[µm]**	**[°]**
1	1400	1200	15	985	2896	104	1054	119
2	1400	1200	12	496	2754	0	0	141
3	1400	1200	9	362	2573	81	777	146
4	1600	1200	15	619	2669	58	692	122
5	1600	1200	12	500	2708	204	1160	135
6	1600	1200	9	400	2768	380	1604	151
7	1800	1200	15	608	2896	269	1940	130
8	1800	1200	12	506	2754	324	1751	141
9	1800	1200	9	431	2573	423	1808	143
10	2000	1200	15	485	2708	462	2012	116
11	2000	1200	12	608	2669	350	2077	136
12	2000	1200	9	415	2768	583	1796	142
13	1400	1000	15	454	2708	143	996	140
14	1400	1000	12	565	2594	139	988	124
15	1400	1000	9	485	2677	227	1135	143
16	1600	1000	15	727	2685	171	1400	122
17	1600	1000	12	562	2654	296	1862	120
18	1600	1000	9	465	2764	450	1604	143
19	1800	1000	15	1112	2846	227	1627	105
20	1800	1000	12	562	2837	481	2257	139
21	1800	1000	9	515	2820	512	2065	144
22	2000	1000	15	731	2896	406	2019	100
23	2000	1000	12	588	2903	588	2188	128
24	2000	1000	9	477	2988	692	2054	134

Table 6: Detected Single Tracks geometrical characteristics.

This parameter can be linked with a dimensionless one, i.e. the aspect ratio. As mentioned in section 7.2.2.2, the AR is the ratio between the width and height of a clad, and both α and AR play an essential role during multi-layer overlaps since they affect the inter-track porosity [94]. To prevent this type of

defect, Paul et al. [60] have experimentally studied that the aspect ratio should be greater than 5, in order to avoid inter-run porosity due to the lack of a fusion zone at bead roots during the DLD deposition. The AR values that have been calculated from the STs analysis are shown in Figure 45 and Figure 46. It is difficult to distinguish clear trends; in general it is possible to say that from v=1000 mm/min to v=1200 mm/min, there is an increment in AR values.

In both Figure 45 and Figure 46, there is a dotted line representing the AR threshold defined before, i.e. AR> 5; the solutions under this value have not been taken into account.

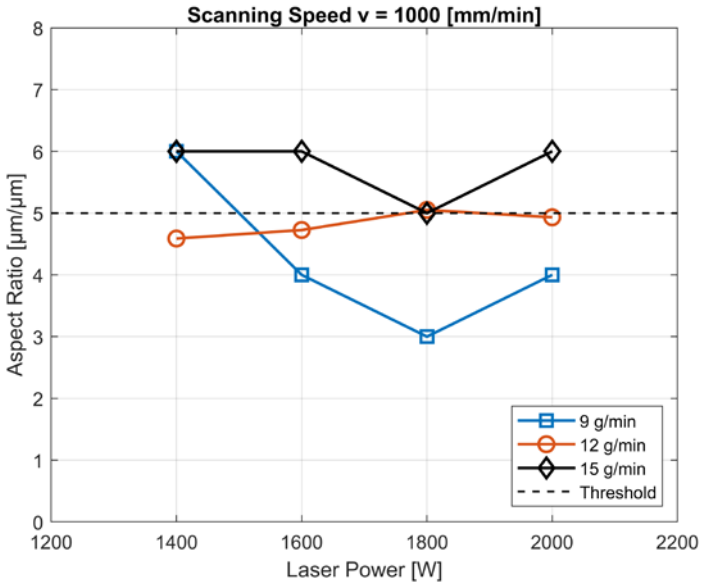

Figure 45: Aspect Ratio of H13 Single Tracks versus laser power, varying the powder feed rate and with a constant scanning speed set at 1000 mm/min.

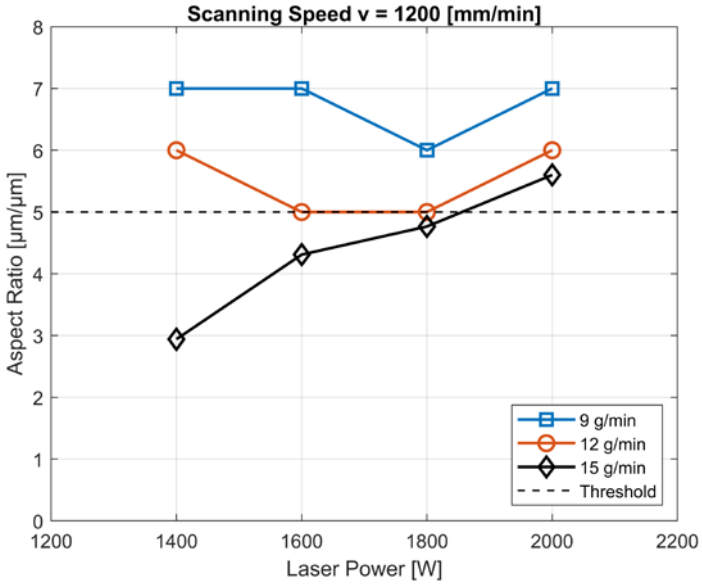

Figure 46: Aspect Ratio of H13 Single Tracks versus laser power, varying the powder feed rate and with a constant scanning speed set at 1200 mm/min.

Another aspect related to the geometrical features and essential for the selection of the proper process parameters is the dilution. The DIL values have been calculated using the formula (3), and displayed in Figure 47 and Figure 48. The DIL increases with the increment of the laser power and decreases with the increment of the powder feed rate. Moreover, the DIL was not affected by varying laser power and remains constant from 1400 W to 1800 W when v and $\dot{m}_p$, respectively, are fixed at 1000 mm/min and 15 g/min.

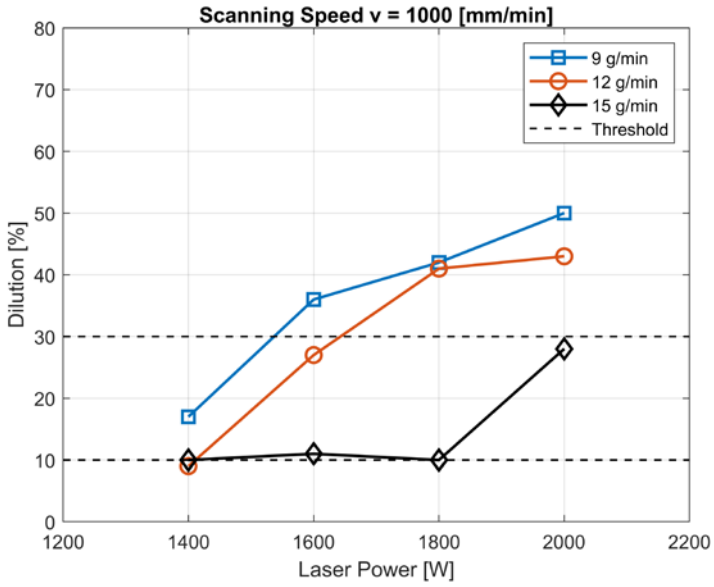

Figure 47: Dilution of H13 Single Tracks versus laser power, varying the powder feed rate and with a constant scanning speed set at 1000 mm/min.

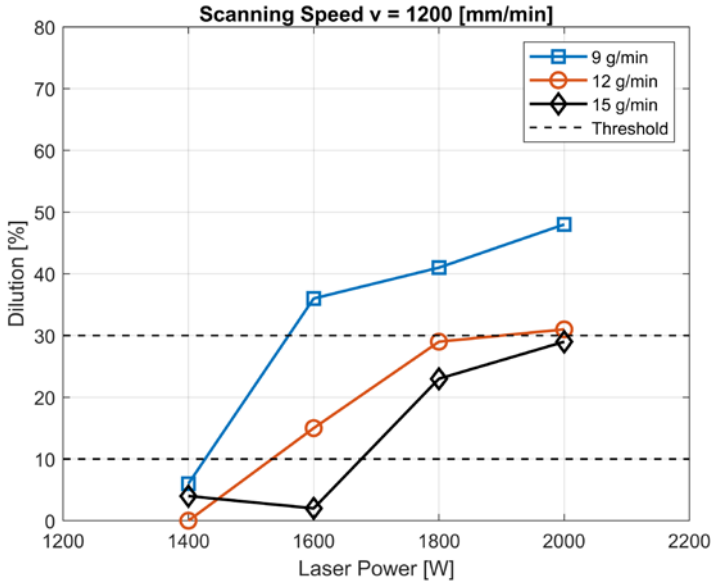

Figure 48: Dilution of H13 Single Tracks versus laser power, varying the powder feed rate and with a constant scanning speed set at 1200 mm/min.

The investigated windows of process parameters have been carried out to a fascinating and wide range of possible dilutions that can be used both for cladding and depositions of 3-D structures. An

interesting consideration is that the combination of P=1400 W, $\dot{m}_p$=12 g/min and v=1200 mm/min imply the absence of the molten material below the surface of the base-material (DIL=0), in this case, the bonding between the deposition material and the substrate is not ensured, although no detachment has been detected in the present work. In the case of laser cladding target, it was reported by many authors, such as Campanelli et al. [95], to use low values of dilution to reduce the mixing between the coating material and the base material. Specifically, Ocelík et al. [96] have suggested a dilution that ranges from 5% to 15% for this purpose. Otherwise, higher values of this unique parameter can permit stronger bonding that is the desired effect in the case of DLD repairing. The typical values of dilution adopted in the DLD process range from 10% to 30%, as reported by Dass et al. [97]. Below DIL=10%, there is the risk of lack of fusion porosity; above DIL=30% there is the risk of keyhole porosities. The dot-lines in Figure 47 and Figure 48 highlighted the defined DIL thresholds.

Finally, it was considered a new geometric parameter, i.e. the shift, defined as the distance between the center *c* of the clad width *w* and the center *c'* of the penetration width *w'*. The results are shown in Figure 49 and Figure 50. In all cases, the shift decreases when laser power increases, save for two exceptions: P=1400 W, v=1200 mm/min, $\dot{m}_p$=12/15 g/min.

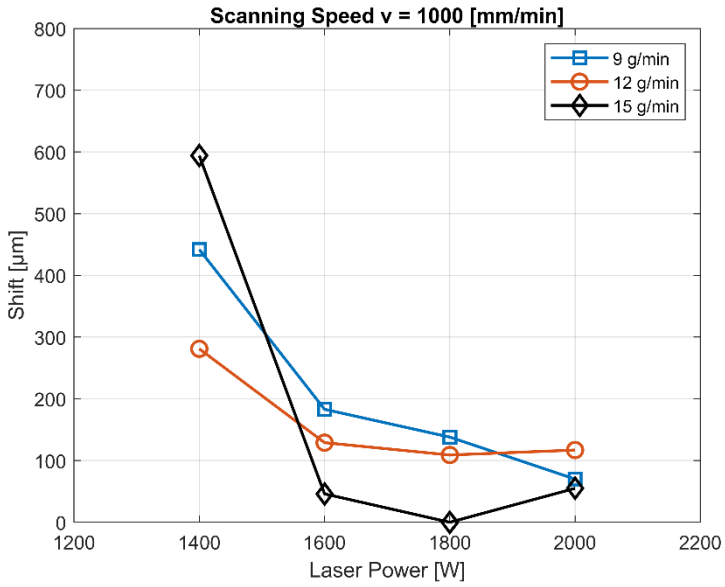

Figure 49: Shift of H13 Single Tracks versus laser power, varying the powder feed rate and with a constant scanning speed set at 1000 mm/min.

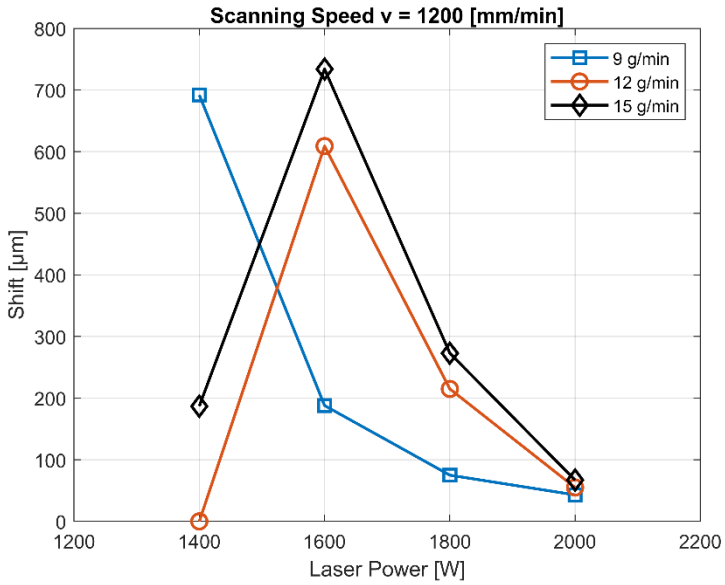

Figure 50: Shift of H13 Single Tracks versus laser power, varying the powder feed rate and with a constant scanning speed set at 1200 mm/min.

Moreover, as visible in the cross-section images (Figure 43 and Figure 44), the shift does not have the same orientation, but can be located either leftward or rightward, although a dwell time of 20 minutes and random DLD order have been used between one deposition and another. At the same time, it is worth considering that there are many phenomena involved in the DLD process, as discussed by Thompson et al. [56], as well as the micro-roughness of the substrate, that can affect the shift. As a consequence, low values of the shift are suggested in the present piece of work. In particular, it is possible to note that, for the process windows with v=1000 mm/min, the lowest values are referred to the case with $\dot{m}_p$=15 g/min, regardless of the power; on the other hand, for the process windows with v=1200 mm/min, the lowest values are generally referred to the case with P=2000 W, regardless of the powder feed rate.

7.2.3.2 Microhardness analysis

A microhardness analysis has been carried out and the mean values have been shown in Figure 51 and Figure 52. The results obtained are better than the microhardness of H13 produced with conventional processes, considered as the reference value (380-560 HV [51]). In the DLD fields, these values are comparable or better to the ones obtained by other authors: Cottam et al. [98] have found a microhardness that ranges from 580 to 650 HV, in the study of Mazumder et al. [99], microhardness ranges from 450 to 580 HV, in the one of Choi et al. [100], it ranges from 520 to 580 HV, in Bohlen et al. [101], it ranges from 400 to 750 HV, in Park et al. [102], it ranges from 550 to 600 HV. In this case, particularly in the process windows with a fixed v equal to 1000 mm/min,

microhardness ranges from 473 to 742 HV; in those with v=1200mm/min, microhardness ranges from 425 to 762 HV.

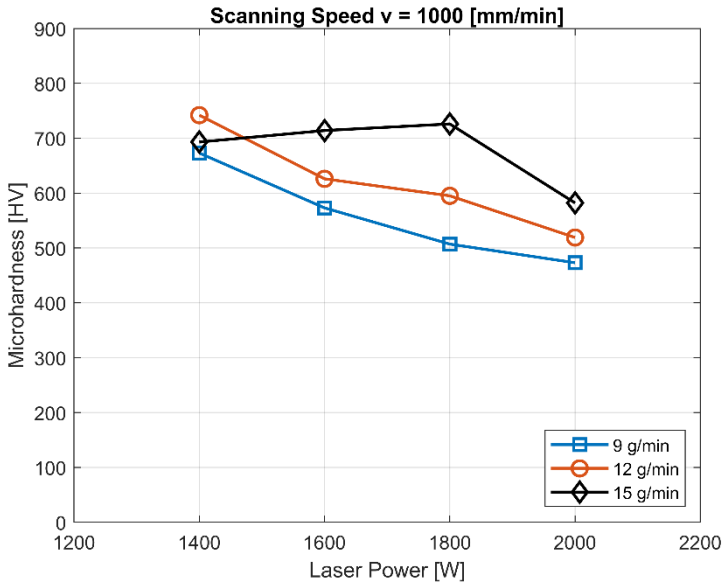

Figure 51: Microhardness of H13 Single Tracks versus laser power, varying the powder feed rate and with a constant scanning speed set at 1000 mm/min.

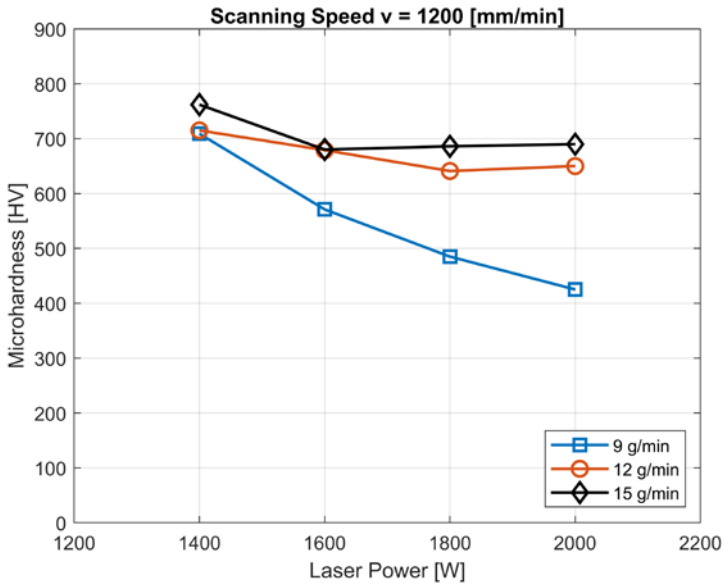

Figure 52: Microhardness of H13 Single Tracks versus laser power, varying the powder feed rate and with a constant scanning speed set at 1200 mm/min.

The HV values mentioned above have been summarized in Table 7.

Type	Microhardness [HV]	References
Wrought H13	380-560	[51]
DLD H13	580-650	[98]
DLD H13	450-580	[99]
DLD H13	520-580	[100]
DLD H13	400-750	[101]
DLD H13	550-600	[102]
DLD H13	425 -762	Present work

Table 7: Comparison of microhardness values of H13.

Generally, the microhardness decreases with the increasing of laser power, and increases with the increasing of powder feed rate. In any case, satisfactory values for microhardness have been obtained for the majority of the depositions. These results are strongly related to the thermal behavior of the process and the material and the related microstructures, which are analyzed in the following section.

7.2.3.3 Metallurgical analysis

All 24 single tracks are characterized using the HITACHI TM3000 SEM. The micrographs of the first ST are shown in Figure 53, showing the evaluation of the microstructure at the center of the line, along a vertical line that begins from the interface of H13 and 316L till to the top of the single track. The cross-section microstructures are revealed by the modified Vilella's reagent and show how strongly the grain morphology is affected by the heat flux vector direction, as explained by Thompson et al. [56], and by the cooling rate [97]. As shown in Figure 53a, d and e, in the bottom-middle part of the ST, it is possible to find a blend of dendritic and cellular structures due to the solid/liquid interface that promotes a unidirectional heat flow occurring from the molten pool to the substrate. On the other hand, on the top of the single track (Figure 53b and c), grains are finer and more equiaxed, indicative of a high cooling rate and of more uniform heat flux. It is possible to note the absence of cracks and the presence of micro-porosities only in the boundary grains.

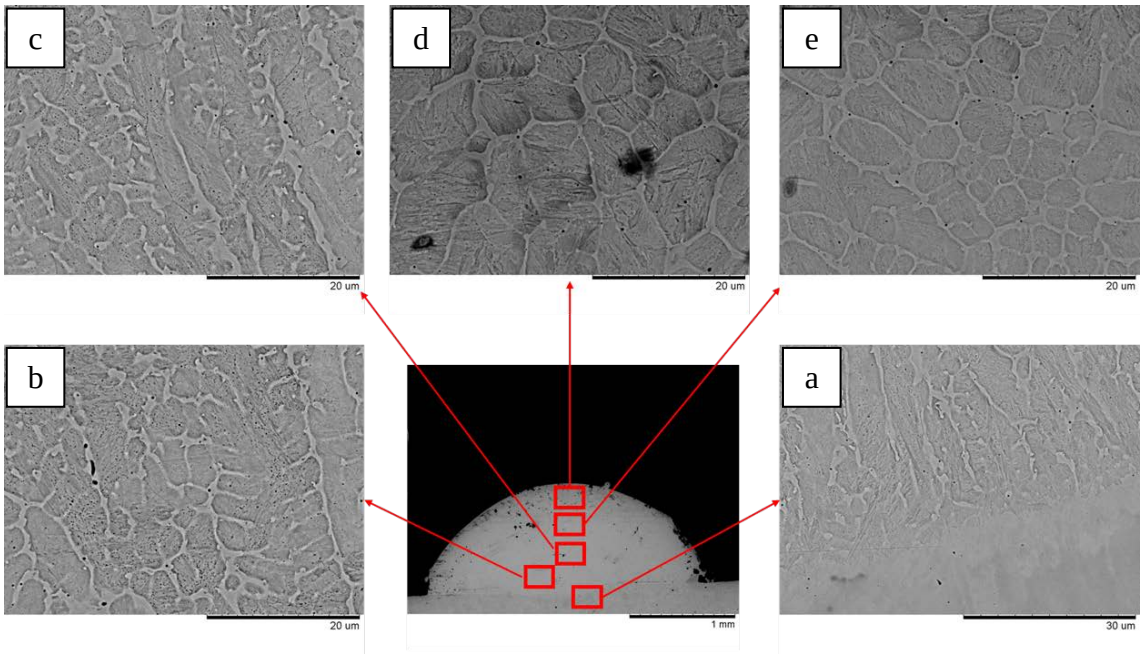

Figure 53: SEM micrographs of Single Track cross-section: a) interface of the deposited material H13 and the substrate316L, b)bottom, c) middle, d) middle/top, e) top of the H13.

Moreover, it is possible to observe lath martensite in the matrix of grains, surrounded by retained austenite in the boundaries. In Figure 54, red arrows highlight the presence of brighter particles, and EDX analysis indicates that they are regions rich in molybdenum, and it can be assumed to be carbides rich in molybdenum.

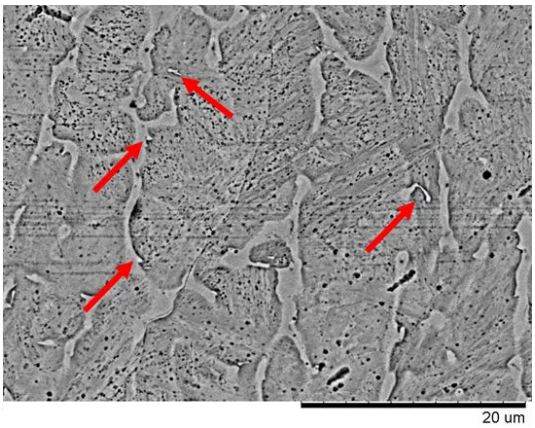

Figure 54: SEM micrographs of ST cross-section.

In order to chemically investigate the interface between the deposited material and the substrate, an EDX line-scan analysis has been carried out, specified in Figure 55a) by the white straight line. It is worth remembering the chemical composition of the materials of interest in Table 3 and Table 4, and considering that Ni is present in 316L and that the amount of Cr is quite lower in H13 rather than in 316L, it was chosen to investigate the presence of these two elements from the top to the bottom of the ST with an EDX line scan analysis. The results are shown in Figure 55b) and c): in both, there is

a first peak highlighted by the dotted line that matches with the light grey curved line indicated by the red arrow in Figure 55a). This peak is probably related to the Marangoni effect that also involves the small presence of Ni detected in the H13 part of ST analyzed (left side of Figure 55b). The second peak reveals the start of the base-plate material, i.e. 316L; between these two peaks, the chemical composition changes gradually, demonstrating complete and successful miscibility without deformations or defects.

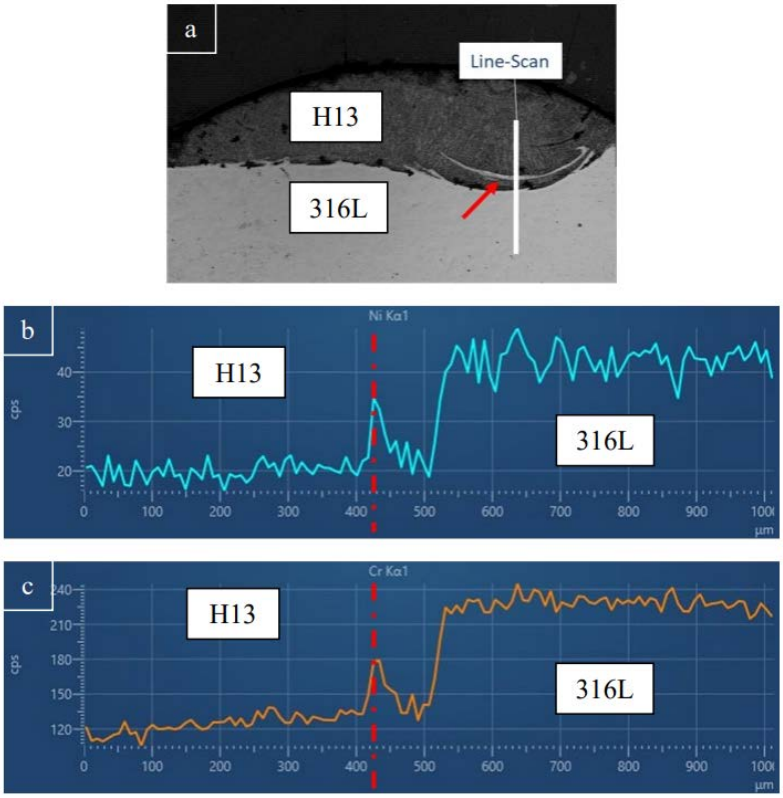

Figure 55: a) Position of the line analyzed by EDX probe on the ST cross-section, b) EDX spectrum for Ni, c) EDX spectrum for Cr.

7.2.4 Single Tracks Conclusions

This section will report the main conclusions of a wide experimental campaign on DLD of hot-work tool steel H13 powders on a 316L stainless steel substrate. Specifically, twenty-four combinations of process parameters have been investigated, varying four levels of laser power, three levels of powder feed rate and two levels of scanning speed. Based on the above mentioned campaign, it is possible to assert that:

- All the STs obtained are compliant with the first requirement concerning the qualitative parameters: no excessive spattering phenomena, lack of fusion, or too wavy STs edges have been detected.
- All the tracks have exceeded the lower limit of the wetting angle ($\alpha > 100°$).

- Concerning the aspect ratios, it is difficult to assess clear trends, but it is possible to say that from v=1000 mm/min to v=1200 mm/min, there is a general increment in AR values. In relation to the dilution, it generally increases with the increase of the laser power. On the other hand, increasing the last one, the shift decreases.
- EDX analyses have shown good miscibility of the H13 and 316L and the presence of heavy carbides on the grain boundaries, while SEM images have pointed out the absence of cracks and detachments and the typical microstructures of the material processed via DLD.
- Suggestions based on a rigorous approach have been provided in order to fill the lack of methods in the literature related to the characterization of single tracks in the DLD field. Precisely, it has been recommended to balance the process parameters to offer the best trade-off between the microhardness values – that should be at least comparable to those present in literature, for the H13, the value is approximately 700HV - and the geometrical requirements - observing specific thresholds of the wetting angle ($\alpha>100°$), Aspect Ratio (AR>5), Dilution (10%<Dil>30%), and Shift (s<50µm).
- On this basis, two combinations of process parameters have been obtained to widen the knowledge of the correct process parameters for printing H13 powders via DLD. The two combinations are P=1600 W, $\dot{m}_p$=15 g/min, v=1000 mm/min ($\alpha>100°$, A.R>5, DIL= ~11%, Shift=45µm, HV= ~710); and P=2000 W, $\dot{m}_p$=15 g/min, v=1200 mm/min ($\alpha>100°$, A.R>5, DIL= ~29%, Shift=50µm, HV= ~700).

7.3 Single Layers

Optimization of the DLD process parameters is a survey in which the second stage is represented by the study of the single layers, printed based on understanding from the single tracks experiments in the previous section 7.2. The single layer is composed of multiple ad adjacent single tracks depositions, and the investigation of the proper process parameters is crucial to avoid inaccurate shapes, such as too high peaks and deep valleys, and ensure homogeneity on the top surface. As also stated by Zhang et al. [35], it is important to achieve a good geometrical accuracy to reduce both the waste of material and time during the machining operation in the hybrid machine. Moreover, in the present work, it is important to consider the difficulties in the cutting post-process operations of the H13 tool steel. For this purpose, after fixing the combination of laser power, powder feed rate and scanning speed, a new parameter is investigated in this section: the overlap distance. The overlap is the complementary parameter of the step-over distance, defined as the distance between one track and the successive one (also known as scan-spacing and hatching distance, for more details see section 5.3). Moreover, another factor that affects the deposition has been taken into consideration: the scanning strategy, defined as the pattern to be followed during the deposition process. The best parameters for multi-layer depositions will be provided at the end of this section.

7.3.1 Experimental campaign

Two combinations of laser power (P), powder feed rate ($\dot{m}_p$) and scanning speed (v) have been used in the investigation of the better process parameters for single layers, based on the findings of section 7.2. Other fixed values are the spot diameter of 3 mm, focal length of 13 mm, high purity Argon gas used for both career gas and shielding gas with a flow rate of 5 l/min and 6 l/min, respectively. Four levels of overlap distance (OV) have been investigated for each combination. In literature, there are different values of overlap and step-over used: in some works, it has been suggested a step-over equal to 2/3 of the width [79], [103]; Mazzucato et al. [62] have indicated 50 and 70% of overlap distance; in the study of Ocelík et al. [96] a 33% of overlap has been employed. It has been decided to use the overlap rather than the hatching distance because it is the value to be inserted in the software Siemens NX. A wide range of OV was investigated in the present work: from 30% to 75%, with an increment of 15%.

7.3.2 Methods

7.3.2.1 H13 single layers fabrication via DLD process

Siemens NX has been employed to generate the code for depositions in Lasertec 65 (Figure 56). In Siemens NX, there is the possibility to insert the values of OV in percentages and millimeters, therefore to ensure the respect of the experimental campaign, based on the width values detected in section 7.2 (Table 6), specific overlaps have been used: OV=30%=0.8 mm, OV=45%=1.2 mm, OV=60%=1.6 mm, OV=75%=2.0 mm. The substrate used is 316L stainless steel with a dimension of 200x200x20 mm^3. It has been sandblasted and degreased with acetone before the deposition process.

Figure 56: Deposition of the H13 single layers on 316L base-plate.

Then, squares of 40x40mm^2 and spaced 10 mm in the y-direction and 20 mm in the x-direction, for a total of 16 different single layers, have been printed. Premising that combinations A and B are the process parameters chosen on STs results (illustrated in Table 8), single layers have been deposited adjacently by changing the other two variables, the overlap and the deposition strategy.

Process parameters			
Combination	**P [W]**	**v [mm/min]**	**$\dot{m}_p$ [g/min]**
A	1600	1000	15
B	2000	1200	15

Table 8: Laser Power, Scanning Speed and Powder Feed Rate in Single Layers experimental campaign.

The run order and the summarized parameters are illustrated in Table 9. A dwell time of 30 minutes has been used between one deposition and the successive one. In Table 9, *SL no.* represents the order of the single layers, *DLD order* is the sequence in which they have been deposited in the Lasertec 65. Precisely SLs from number 1 to 12 have been deposited on a first substrate plate, and the SLs from number 13 to 16 have been deposited on a second substrate. In this experimental campaign, a contour strategy has not been adopted, and each sample was printed twice on the other two 316L plates.

SL no.	**DLD order**	**Process parameters**		
		Fixed Parameters	**OV [%]**	**Deposition Strategy**
1	6	Combination **A**	30	ZIG
2	12	Combination **A**	45	ZIG
3	1	Combination **A**	60	ZIG
4	5	Combination **A**	75	ZIG
5	9	Combination **A**	30	ZIG ZAG
6	4	Combination **A**	45	ZIG ZAG
7	10	Combination **A**	60	ZIG ZAG
8	3	Combination **A**	75	ZIG ZAG
9	7	Combination **B**	30	ZIG
10	2	Combination **B**	45	ZIG
11	8	Combination **B**	60	ZIG
12	11	Combination **B**	75	ZIG
13	16	Combination **B**	30	ZIG ZAG
14	13	Combination **B**	45	ZIG ZAG
15	15	Combination **B**	60	ZIG ZAG
16	14	Combination **B**	75	ZIG ZAG

Table 9: Run order and parameter settings for the deposition of H13 single layers.

7.3.2.2 Characterization

The first stage of the characterization was represented by the waviness analysis, conducted using the confocal microscope Leica DCM3D (section 6.2.1). After that, in order to investigate the microhardness and the metallurgical aspect, single layers have been cut and cross-sectioned in the perpendicular direction to the deposition one via electrical discharge machining to obtain three profiles for the characterization, as shown in Figure 57.

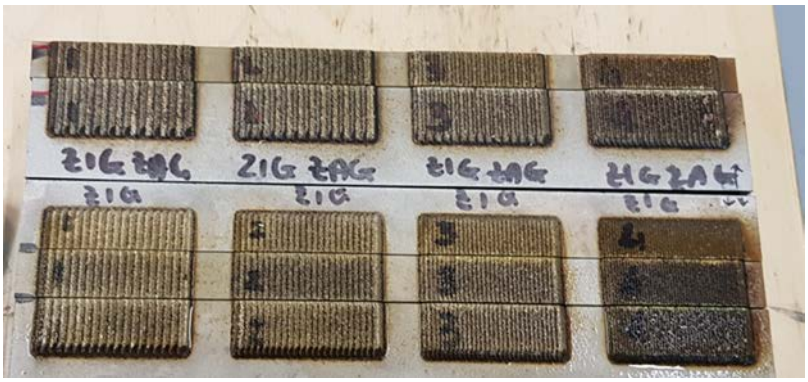

Figure 57: EDM cuts in single layers.

Then, the specimens have been hot mounted in an acid-proof resin. The metallographic preparation is similar to the one described in section 7.2.2.2, and it has included water-cooled silicon carbide paper (200 mm diameter) for the grinding stage. The used grit sequence was 240, 320, 400 and 600-grit, with a grinding time of 3 minutes. Then, specimens have been polished in three stages, with 9, 6 and 1 μm diamond abrasive suspension to the polishing cloths. The polishing time has been 5 minutes [54]. Microstructure characterization has been performed by means of OM and SEM analyses on polished metallographic cross-sections after chemical etching with modified Vilella's reagent (100ml ethanol, 1.6gr picric acid and 8.5ml hydrochloric acid). Microhardness Vickers measurements were conducted on the metallographic samples with a dwell time of 15 s, as suggested by the standard ASTM E92-82 [55], and with a distance of 2 mm between each indentation in the horizontal direction and with a distance of 0.5 mm in the vertical direction. Concerning the relationship between the input parameters and the experimental outputs, i.e. waviness and microhardness, the process effects have been analyzed by means of the software *Minitab*®. The data have been analyzed through the Analysis of Variance (ANOVA), the statistical significance of the terms (i.e. process parameters) of the applied model has been evaluated through the analysis of different descriptors such as the p-value with a confidence interval (C.I.) of 95% and the adjusted determination coefficient (R-sq (Adj)) [104].

7.3.2.3 Theoretical background

Concerning the surface analysis, an area of 10x10 mm^2 has been acquired from the center of the sample; this value has been chosen as representative of the entire region on the basis of the previous acquisition. Figure 58 shows the required operations for the surface analysis. Starting with the acquisition of the surface sample by means of the confocal microscope, a ".mpf" file named "*studiable*" has been generated and, then, elaborated using the software Leica Map™. Five arbitrary profiles have been analyzed. As mentioned previously, detecting the waviness values in single layers is an essential step to ensure the stability of the process through successively deposited layers and thus reduce the error in geometric accuracy, since too wavy SLs can result in inaccurate shapes or edge collapses. Moreover, another reason for obtaining surfaces as flat and homogeneous as possible is that less material has to be removed, producing less waste. On the other hand, the final product obtained through DED processes is a kind of semi-finished product that needs to be machined in a post-processing step (e.g. by milling operations). Considering the previous premise, it is now possible to understand why the roughness analysis is not valuable for the optimization process context. Only the waviness has been used for surface characterization. In the following are reported the surface parameters utilized in this work, with their definitions [105]–[107]:

- **W_a**: the arithmetic mean of the waviness profile deviations, Z_i , obtained from the filtered primary profile and it is calculated from the formula:

$$W_a = \frac{1}{N}\sum_{i=1}^{N}|Z_i| \tag{4}$$

where N is the number of measurement points of the profile.

- **W_{sk}**: the slope of the waviness profile and it is calculated from the formula:

$$W_{sk} = \frac{1}{W_q^3}\frac{1}{N}\sum_{i=1}^{N}Z_i^3 \tag{5}$$

This parameter can be positive, negative or zero, and is unit-less since it is normalized by W_q. The W_{sk} parameter describes the shape of the topography height distribution. The skewness is zero for a waviness profile with a random (or Gaussian) height distribution with a symmetrical topography. The skew's direction depends on whether the bulk of the material is above (negative skew) or below the mean line (positive skew). In Equation (6), W_q is the square mean of the waviness deviations, which is defined as the square mean of the ordinates of the z_i profile, and it is calculated from the formula:

$$W_q = \sqrt{\frac{1}{N}\sum_{i=1}^{N} Z_i^2} \tag{6}$$

Referring to Figure 58, the acquisition of the real surface is followed by the selection of the proper filters to evaluate the waviness profile, in combination with the choice of the correct cut-off, which is a kind of filter size.

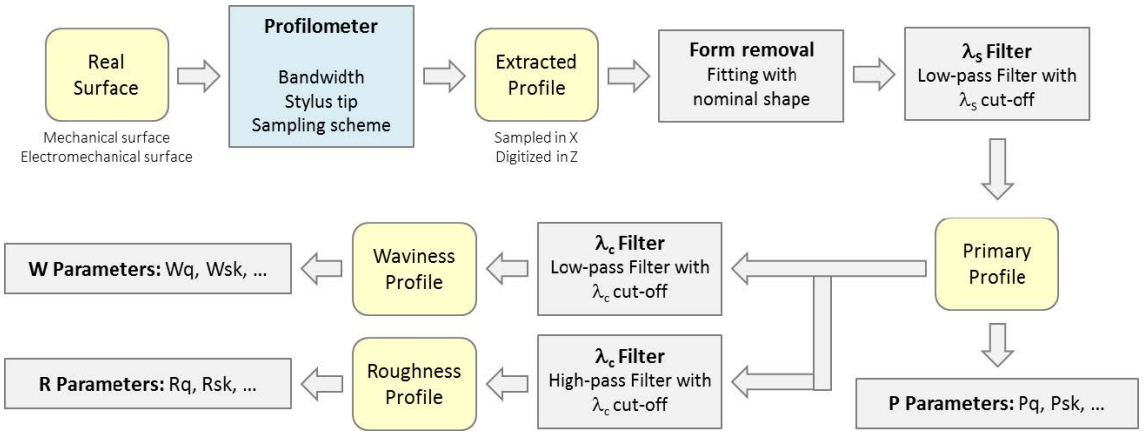

Figure 58: Operation for the surface analysis [108].

Filtering in metrology is an operation that converts a profile or a surface by removing components of the surface topography that are below or above a given scale. The most common form of filtering is to split data frequencies (or wavelengths) into two parts, the first one having the long wavelengths or low frequencies (waviness), the other one having the short wavelengths or high frequencies (roughness) [109]. The waviness and roughness phenomena are separated mathematically and lead to different results (Figure 59). The separation criterion is a wavelength threshold called the cut-off. The filter distributes the large wavelengths above the cut-off to the waviness, and the small wavelengths below the cut-off to the roughness. The quality of the separation depends both on the type of filter and the cut-off value.

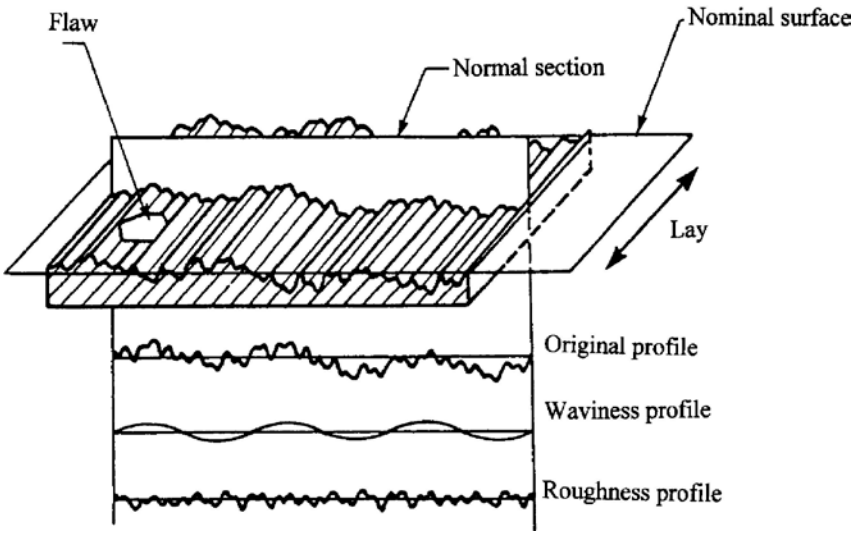

Figure 59: Original, waviness and roughness profile of a surface [110].

Leica Map™ allows selecting the following filter:

- Gaussian filter (ISO 16610-21 for profile, ISO 16610-61 for surfaces)
- RC2 filter
- RC2-PC filter
- Cubic Spline filter (ISO 16610-22 for profiles, ISO 16610-62 for surfaces)
- Double Gaussian filter (ISO 13565-1 for profiles)
- Robust Gaussian filter (ISO 16610-31 for profiles, ISO 16610-71 for surfaces)

The Gaussian filter is the one of interest in the present work. It appeared in 1996 in the ISO 11562 and was then replaced by ISO 16610-21 [111]. As confirmed by Raja et al. [105], it is the most widely employed filter nowadays and has replaced the obsolete RC2 filter. It is a low-pass filter, and its weighing function and transmission characteristics are given by equations (7) and (8) :

$$S(x) = \frac{1}{\alpha\lambda_c}\exp\left(-\pi\left(\frac{x}{\alpha\lambda_c}\right)^2\right) \quad (7)$$

$$\frac{A_{OUTPUT}}{A_{INPUT}} = \exp\left(-\pi\left(\alpha\frac{\lambda_c}{\lambda}\right)^2\right) \quad (8)$$

Where, respectively, $\alpha = \sqrt{ln\ 2/\pi} = 0.4697$, x is the position from the origin of the weighing function, λ_c is the long-wavelength roughness cut-off, and λ is the wavelength of different sinusoidal profiles on the surface [109]. The Gaussian filter attenuates the spectral components by 50% at the cut-off and does not shift the phase of the filtered surface (one of the significant drawbacks of the RC2 filter). Moreover, it is not affected by accidental or local peaks and valleys of a profile, but not so strongly as the Robust Gaussian filter.

The successive step consists in choosing the cut-off. The cut-off is the limit wavelength between waviness and roughness, as mentioned above. The standard values are 0.08 mm; 0.25 mm; 0.8 mm; 2.5 mm; 8 mm, but the software Leica Map™ allows custom values. In the present work, a cut-off equal to 0.8 mm has been employed. Moreover, the use of the Gaussian filter with the associated cut-off implies, by default, that half of the length of a cut-off is removed from both edges of a filtered profile. With the application of a particular algorithm, present in the Leica Map™, it is possible to filter the whole *studiable* up to its edges. If this option is chosen, and this is the case, the filtered surface has the same size as the original surface.

7.3.3 Results and discussion

The second step to achieving high-quality 3D depositions is the study of single layers. The first result is that all the process parameters investigated to process H13 SLs led to successful depositions, as shown in Figure 60, and no one has peeled off during or after the DLD process.

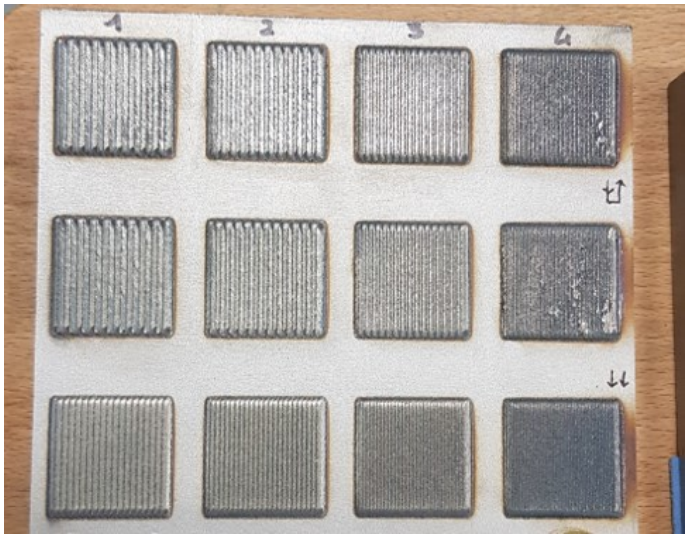

Figure 60: H13 single layers.

7.3.3.1 Surface analysis

The results of the acquisitions of the confocal microscope of the real surfaces before the filtering phase are shown in Figure 61, Figure 62, Figure 63, Figure 64. With a preliminary inspection, it is possible to observe that in all figures, at 30% of overlap, the single tracks can be clearly seen, and it seems that more wavy builds have been generated using gradually larger hatch spacings.

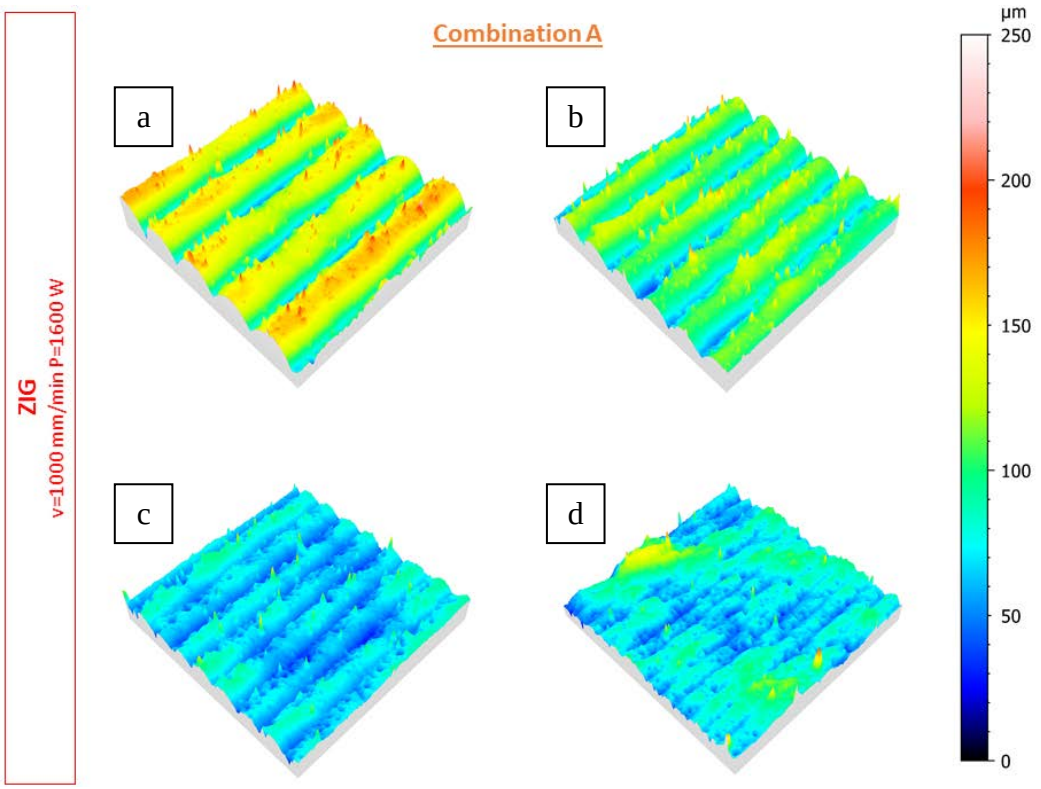

Figure 61: Comparison between the 3D surfaces of the Single Layers of combination A, deposited with ZIG strategy, characterized by, respectively, an overlap of a)30%, b)45%, c)60% and d)75%.

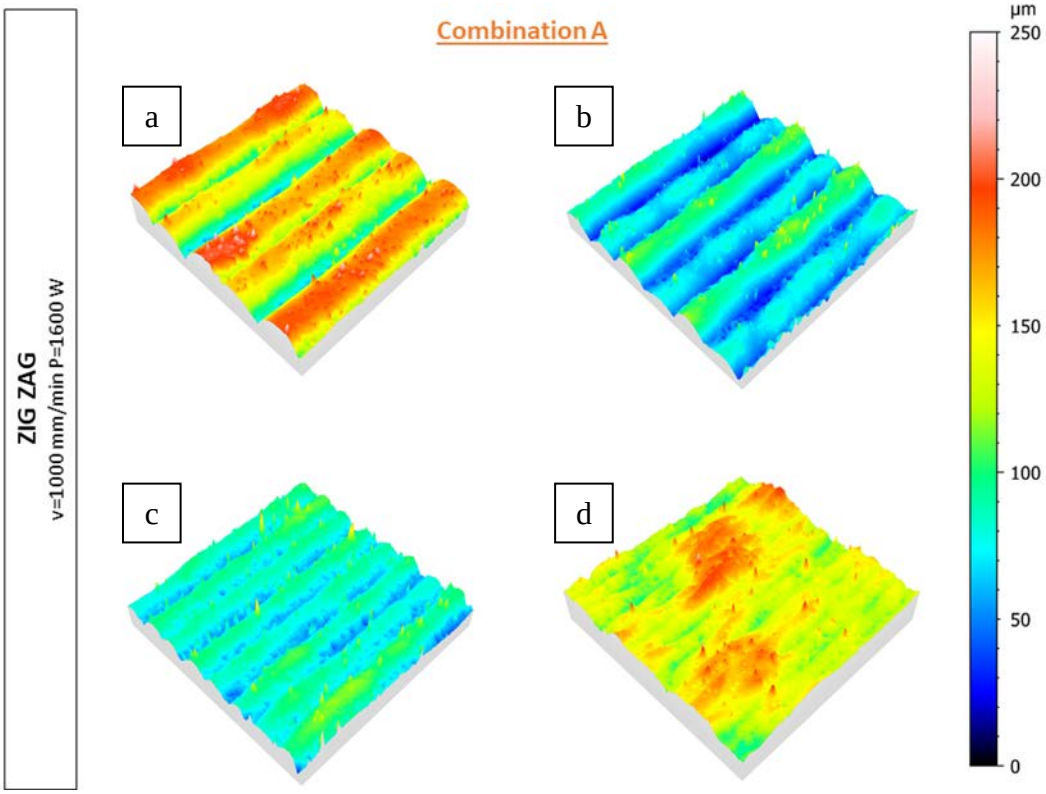

Figure 62: Comparison between the 3D surfaces of the Single Layers of combination A, deposited with ZIGZAG strategy, characterized by, respectively, an overlap of a)30%, b)45%, c)60% and d)75%.

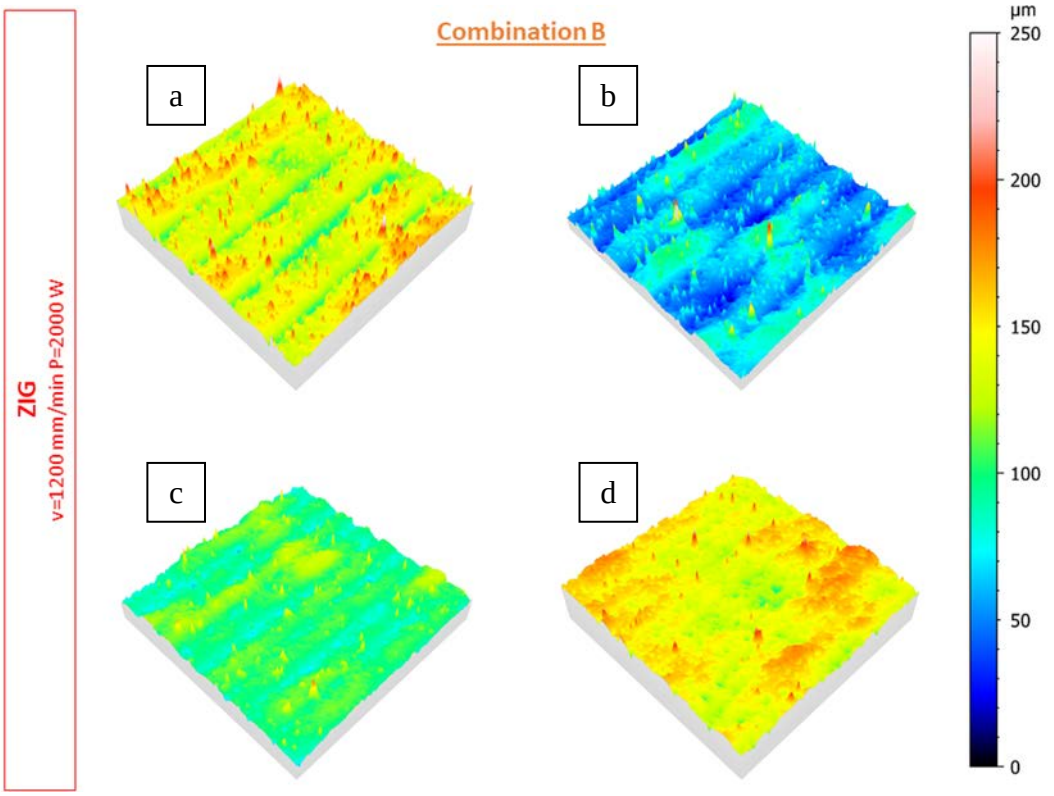

Figure 63: Comparison between the 3D surfaces of the Single Layers of combination B, deposited with ZIG strategy, characterized by, respectively, an overlap of a)30%, b)45%, c)60% and d)75%.

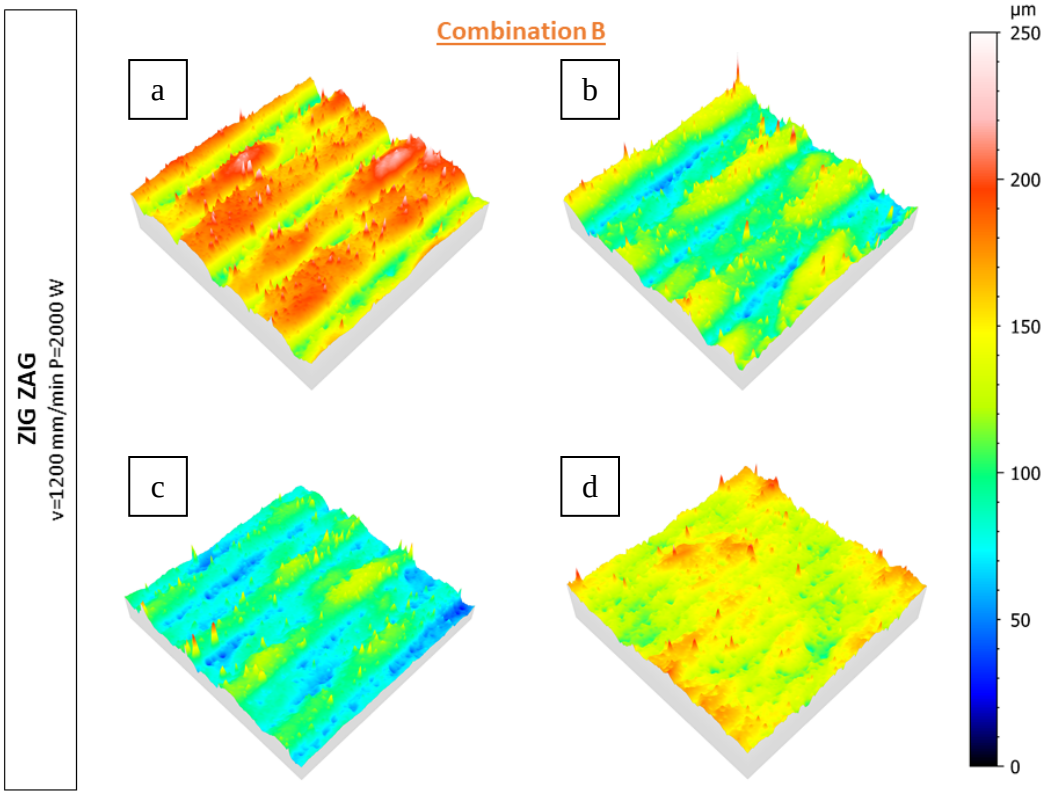

Figure 64: Comparison between the 3D surfaces of the Single Layers of combination A, deposited with ZIGZAG strategy, characterized by, respectively, an overlap of a)30%, b)45%, c)60% and d)75%.

Figure 65, Figure 66, Figure 67, Figure 68 show all SLs conditions for process parameters A and B, and ZIG and ZIGZAG strategy. The figures aim to illustrate the effect of the applied filter and cut-off with respect to the original profile. In particular, the blue line is the primary profile, and the red line is the waviness profile. A Gaussian low-pass filter has been applied with a cut-off of 0.8 mm. It is possible to note that the correct selection of the cut-off has allowed to faithfully reproduce the waviness surface trend, generating a mean line that is undisturbed by accidental or local features of the primary profile. It is worth highlighting that the algorithm for managing the edges has been applied; it represents an important aspect to avoid the loss of valuable data.

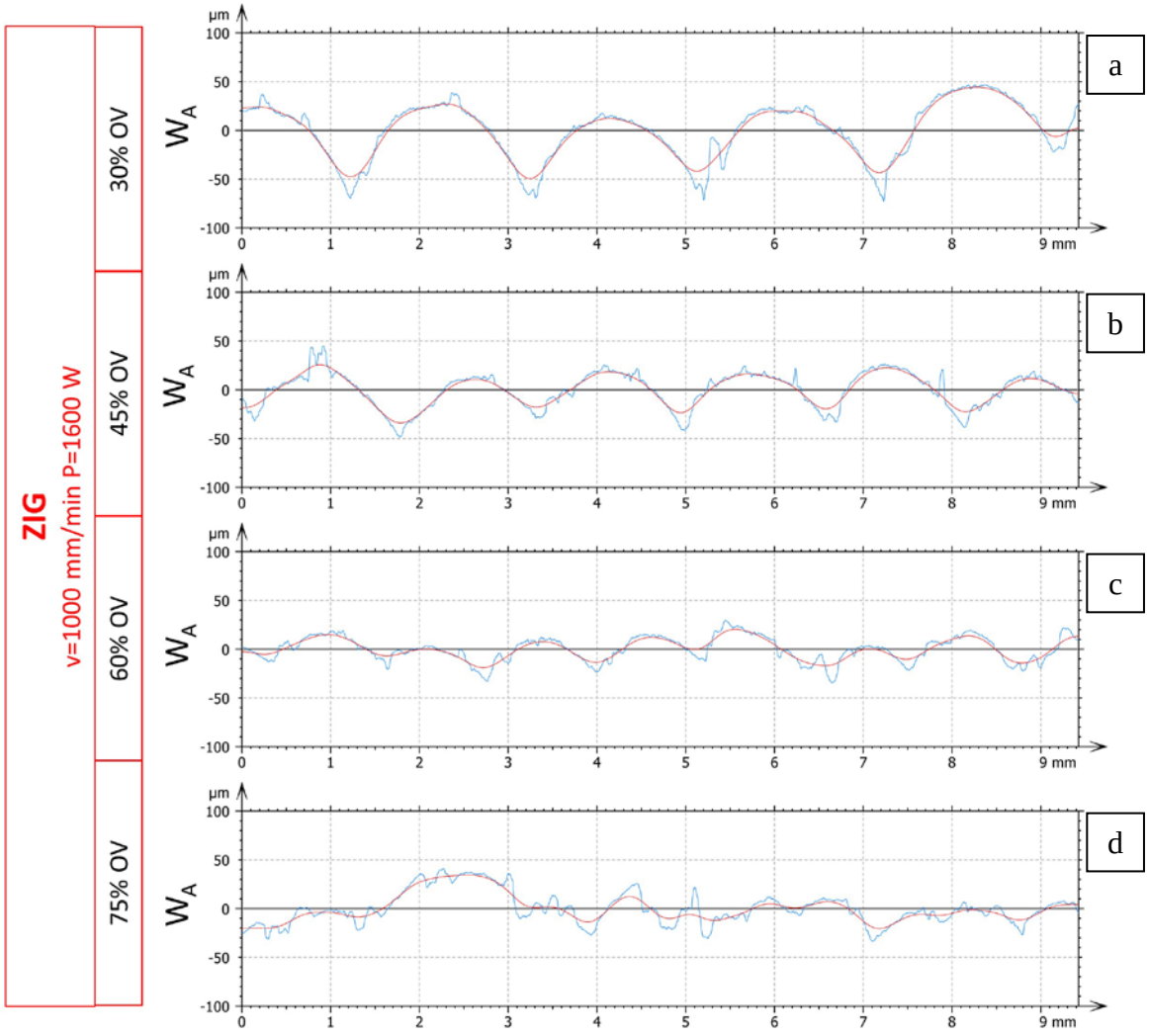

Figure 65: Primary and waviness profile, respectively in blue and red, of the Single Layers deposited with process parameters combination-A, ZIG strategy, an overlap of a)30%, b)45%, c)60%, d)75%.

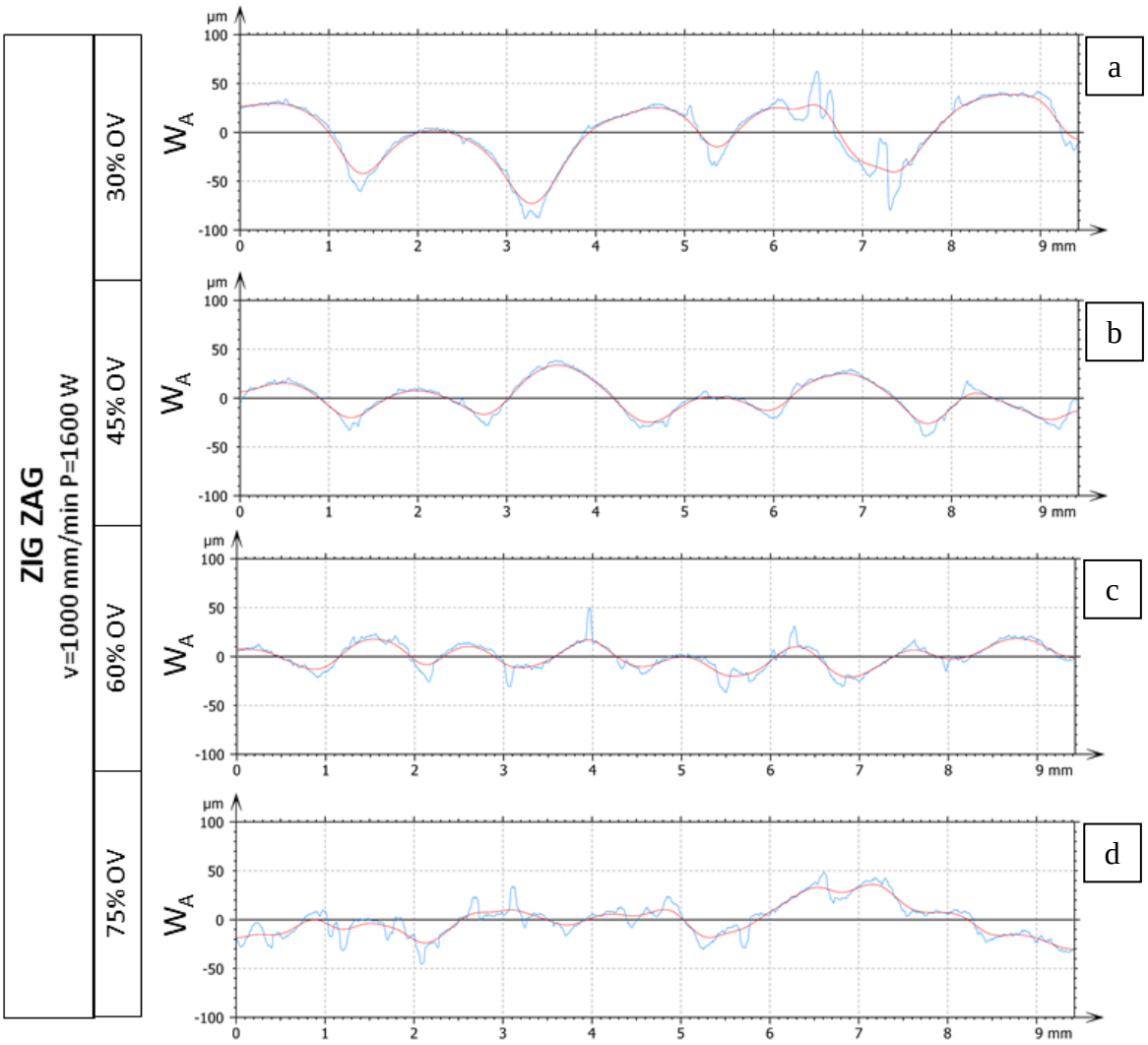

Figure 66: Primary and waviness profile, respectively in blue and red, of the Single Layers deposited with process parameters combination-A, ZIGZAG strategy, an overlap of a)30%, b)45%, c)60%, d)75%.

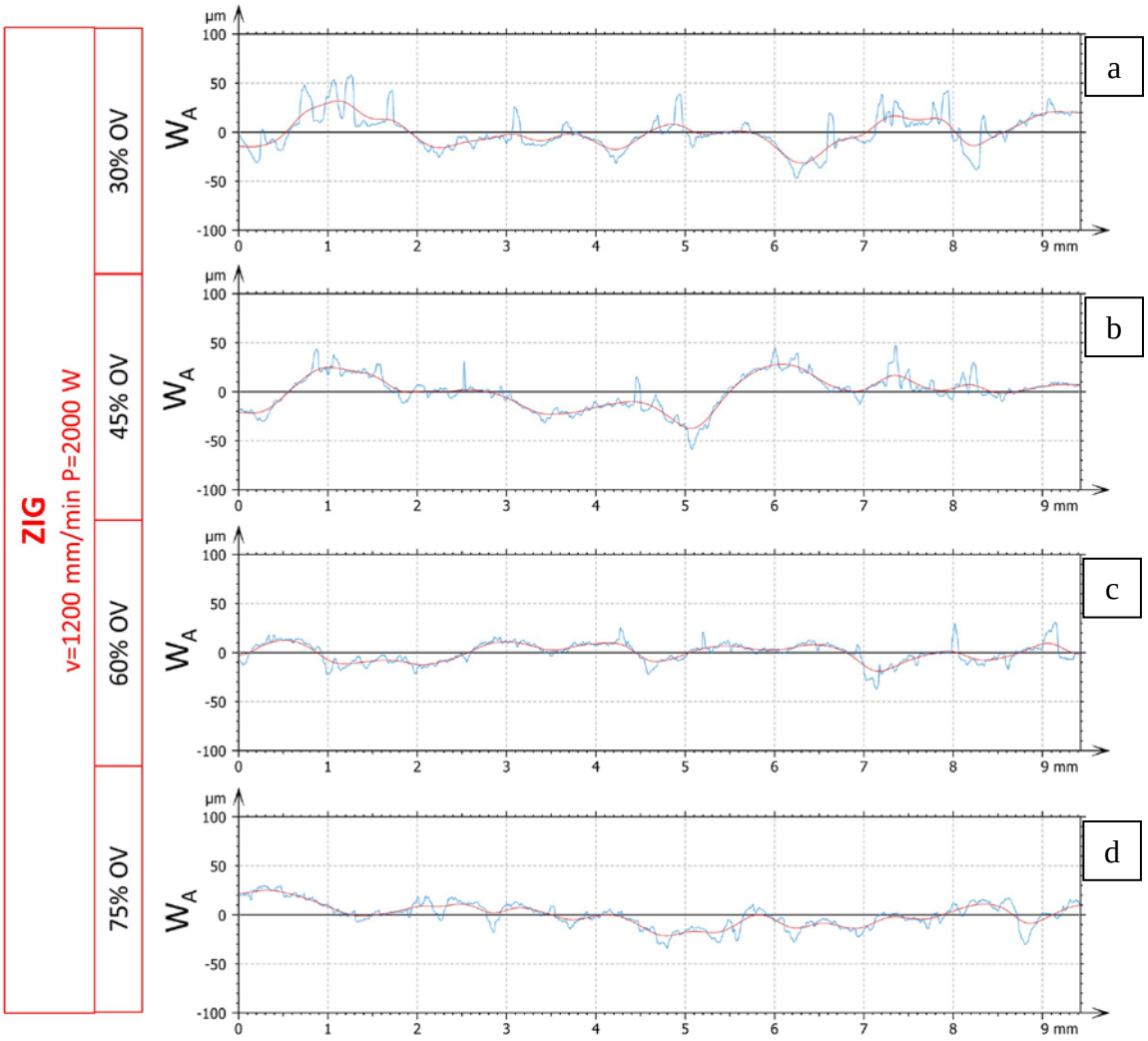

Figure 67: Primary and waviness profile, respectively in blue and red, of the Single Layers deposited with process parameters combination-B, ZIG strategy, an overlap of a)30%, b)45%, c)60%, d)75%.

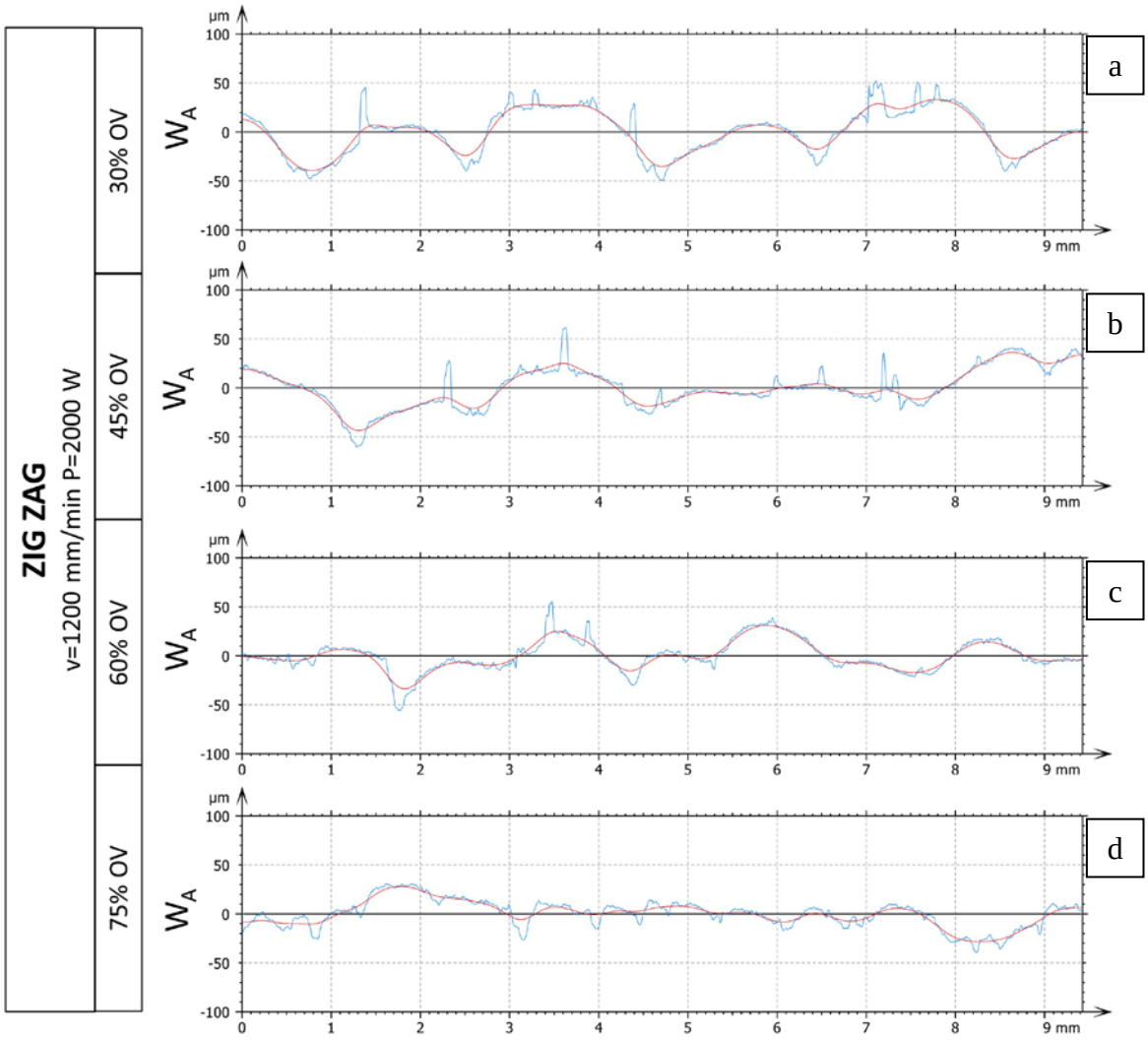

Figure 68: Primary and waviness profile, respectively in blue and red, of the Single Layers deposited with process parameters combination-B, ZIGZAG strategy, an overlap of a)30%, b)45%, c)60%, d)75%.

The results of the waviness analyses are shown in Figure 69 and Figure 70 about, respectively, process parameters combination-A and combination-B. In all cases, the maximum value of W_a has always been reached at OV=30%, so when the hatching distance is equal to 2 mm; after that, the waviness decreases as overlap increases, followed by a final increment of W_a for the highest OV, i.e. 70%. It is due to the fact that, in the beginning, a hatching distance of 2 mm for width tracks is excessively large, so the overlapping of material is not sufficient to avoid a strong wavy effect on the surface. Increasing the overlapping, the surface of single layers becomes flatter until OV = 60% (HD=1.2mm), when the minimum waviness value has been reached. On the other hand, the final rise of W_a is due to an excessive increment of the OV, which is translated as an accumulation of deposited material between the adjacent and successive tracks, resulting in over-deposition and in phenomena out of control, for both strategies in combinations A and for the ZIG strategy for combination B. A decreasing trend of waviness as OV increases for the entire OV range has been found only in the case

of ZIGZAG strategy-combination B. Moreover, in most cases, for OV=45 and 60%, the standard deviation is lower than the OV=30 and 70%, concluding that the process is more stable for intermediate values of OV.

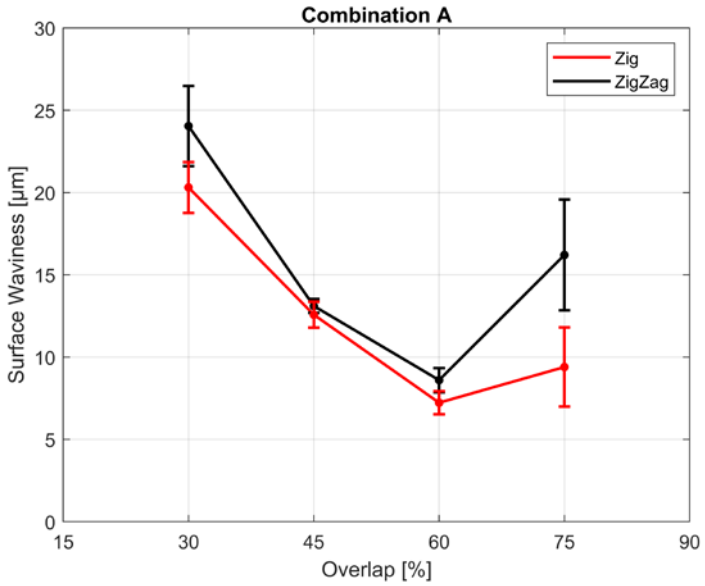

Figure 69: Waviness and Std. Dev. of H13 Single Layers versus overlap, according to the Zig and ZigZag strategy (combination A).

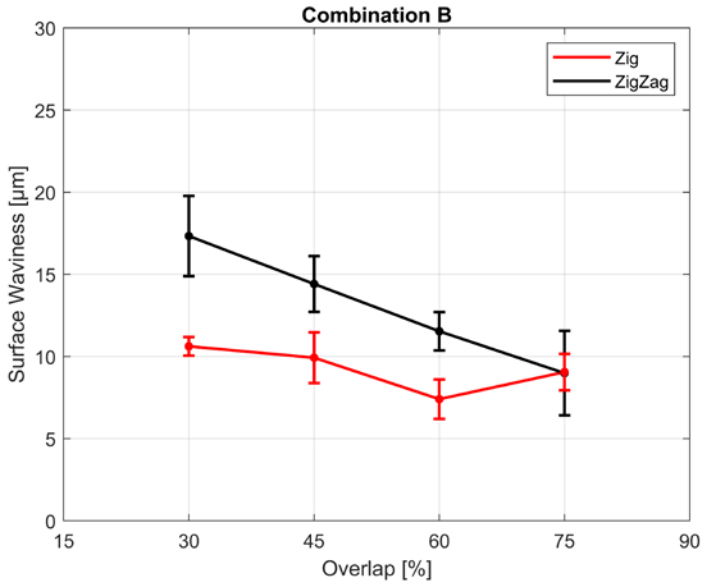

Figure 70: Waviness and Std. Dev. of H13 Single Layers versus overlap, according to the Zig and ZigZag strategy (combination B).

SL no	Process Parameters				Outputs			
	Combination	OV [%]	HD [mm]	Deposition Strategy	W_a [µm]	Std. Dev. [µm]	W_{sk} [µm]	Std. Dev. [µm]
1	**A**	30	2.0	ZIG	20.3	1,5	-0.4	0.1
2	**A**	45	1.6	ZIG	12.6	0.9	-0.3	0.1
3	**A**	60	1.2	ZIG	7.2	0.7	0.1	0.3
4	**A**	75	0.8	ZIG	9.4	2.4	-0.1	1.1
5	**A**	30	2.0	ZIG ZAG	24.0	2.4	-0.5	0.2
6	**A**	45	1.6	ZIG ZAG	13.1	0.4	0.3	0.4
7	**A**	60	1.2	ZIG ZAG	8.6	0.7	0.1	0.7
8	**A**	75	0.8	ZIG ZAG	16.2	3.3	0.4	0.2
9	**B**	30	2.0	ZIG	10.6	0.6	0.1	0.3
10	**B**	45	1.6	ZIG	9.9	1.5	2.6	0.3
11	**B**	60	1.2	ZIG	7.4	1.2	-0.5	0.5
12	**B**	75	0.8	ZIG	9.1	1.1	0.2	0.4
13	**B**	30	2.0	ZIG ZAG	17.3	2.4	-0.4	0.4
14	**B**	45	1.6	ZIG ZAG	14.4	1.7	0.4	0.3
15	**B**	60	1.2	ZIG ZAG	11.5	1.7	0.3	0.2
16	**B**	75	0.8	ZIG ZAG	8.9	2.6	0.0	0.2

Table 10: Surface findings of Single Layers depositions: Waviness and Skewness with the correlated Std. Dev.

In both cases, although in literature usually the most common deposition strategy is the ZIGZAG, it is clear that using the ZIG strategy, a more uniform surface, characterized by lower values of waviness, can be obtained. In particular, both with the combination A and B, the lowest values of W_a are reached by an overlap of 60%. Probably, it is affected by a lower cooling rate that allows a more gradual solidification. Indeed, in the zig strategy, at the end of a deposition track, the laser has been stopped (but not the shielding gas), and the deposition head has returned to the initial position indicated by the program and related to the designed G-code file. Assuming that X_0 is the initial deposition point and that X_1 is the ending deposition point, in the ZIG case, the track is not immediately subjected to another passage of the thermal source, as happened in the case of the ZIGZAG strategy, but during the path of the laser head from X_0 to X_1, there is a range of time in which it can gradually solidify. Instead, in the ZIGZAG case, the repeated passages of the heat source

could affect the shape of the previous track, in which the material is not completely solidified. The exact results of the waviness analysis are summarized in Table 10. The mean value of skewness is nearly zero in most cases, indicative of an excellent symmetry of the waviness in the surface printed in the chosen windows of process parameters.

The analysis of variance is shown in Table 11, it is possible to note that the overlap, the two combinations of process parameters and the adopted deposition strategy significantly affect W_a, specifically the most influential is the overlap, followed by the strategy and then by the process parameters combinations.

R-sq (Adj)	**67%**
Source	**p-value**
Process parameters combinations	0.000
Overlap	0.000
Strategy	0.000

Table 11: Statistical analysis of the SLs tests: Waviness ANOVA test results.

Moreover, what is discussed above about the W_a trend is confirmed in Figure 71, where the average minimum values of waviness can be obtained for process parameters Combination-B, overlap equal to 60% and ZIG strategy. In conclusion, referring to the same graphs, it is possible to note that all the variables statistically affect the results.

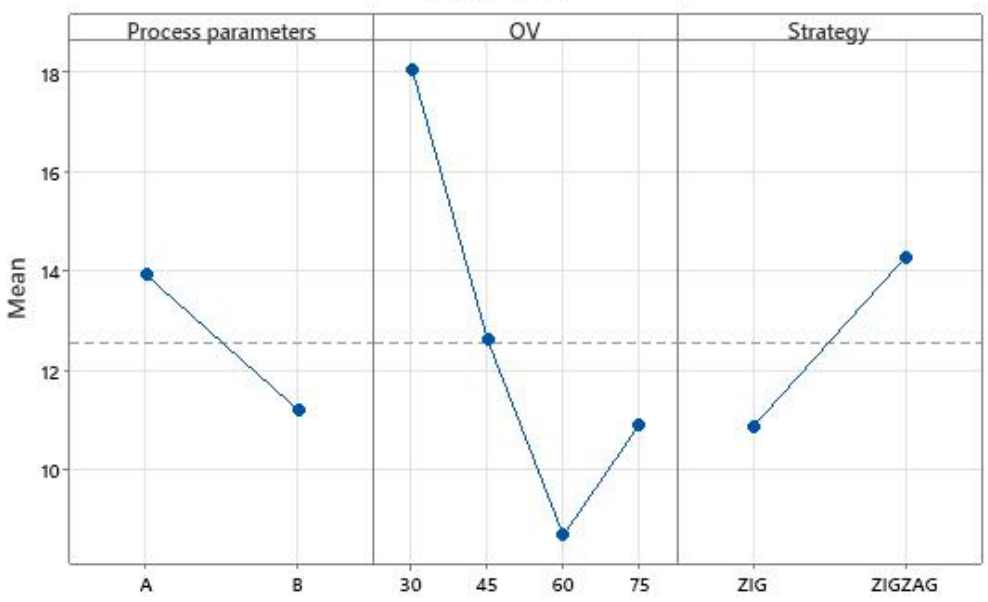

Figure 71: Main effects Plot for W_a.

7.3.3.2 Microhardness analysis

A microhardness analysis was carried out for each sample and along the entire width of a single layer. Figure 72 shows the microhardness in the direction of the width of the SL-2, in the middle of the sample, for a length of 28 mm and with a distance between one measurement and another of 2 mm. Microhardness ranges from 690 to 720 HV, so it is possible to assert that the mean value of HV and its standard deviation could be representative of the microhardness property of each SL (Figure 73 and Figure 74).

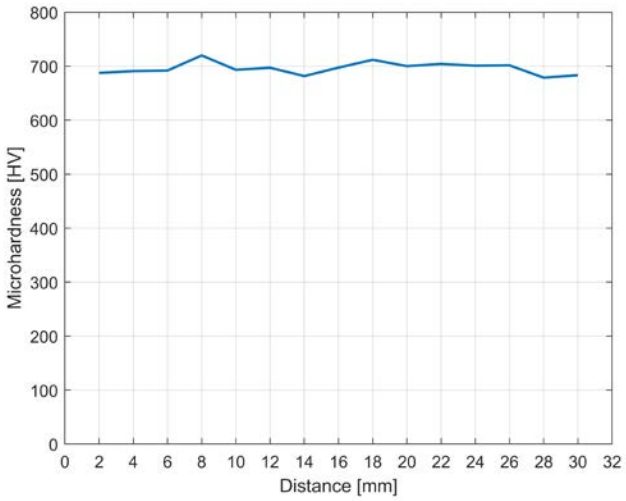

Figure 72: Microhardness values along the width direction of single layer 2.

In Figure 73, the microhardness slightly increases with the increment of the overlap in the range of OV from 30 to 60%, a further increment of the overlap doesn't affect the microhardness behavior and the values are almost the same.

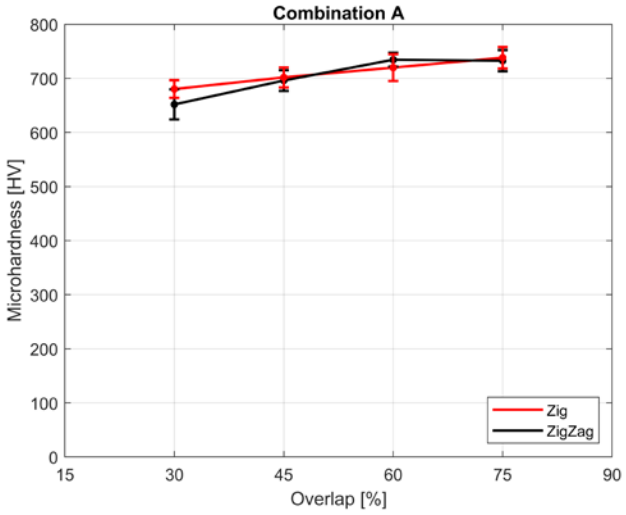

Figure 73: Microhardness and Std. dev. of H13 Single Layers versus overlap, according to the Zig and ZigZag strategy (combination A).

According to what is displayed in Figure 74, instead, the microhardness remains constant, or at least slightly decreases, in the 30%-45% OV range. After this, the microhardness increases with the increase of the overlap.

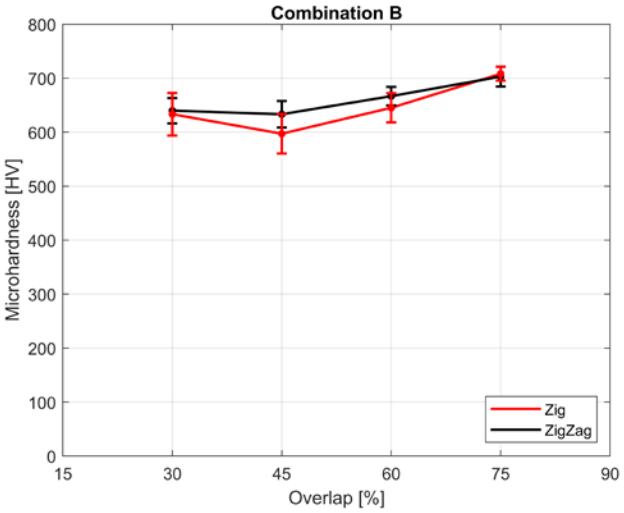

Figure 74: Microhardness and Std. dev. of H13 Single Layers versus overlap, according to the Zig and ZigZag strategy (combination B).

In both cases, the Zig strategy involves lower microhardness. However, referring to Table 7, the results obtained are more than satisfactory in terms of microhardness.

At this point, some considerations can be made: if the final target is a cladding process, the ZIGZAG strategy is suggested, considering higher values of microhardness and a reasonable waviness and related skewness. On the other hand, if the final target is the printing of a metal 3D component, the ZIG deposition strategy is suggested, considering that the samples are characterized by low values of waviness and acceptable skewness, providing hardness values comparable or higher to the ones present in literature.

The analysis of variance is shown in Table 12, it is possible to note that the two combinations of process parameters and the overlap significantly affect HV; on the other hand, the adopted deposition strategies are not statistically influent, as clearly shown in Table 12 by seeing its p-value (major than 0.05).

R-sq (Adj)	**68%**
Source	**p-value**
Process Parameters combinations	0.000
Overlap	0.000
Strategy	0.377

Table 12: Statistical analysis of the SLs tests: Microhardness ANOVA tests results.

This is also confirmed in Figure 75, where the average maximum values of microhardness for process parameters Combination-A and 60-75% overlap are observed to be higher than those for the process parameters Combination-B. In the same graph, it is possible to observe that the deposition strategy is not influent for HV, indeed their average maximum values in these two layouts are comparable. The higher values of HV are found for process parameters B and using an overlap equal to 60% or 75%.

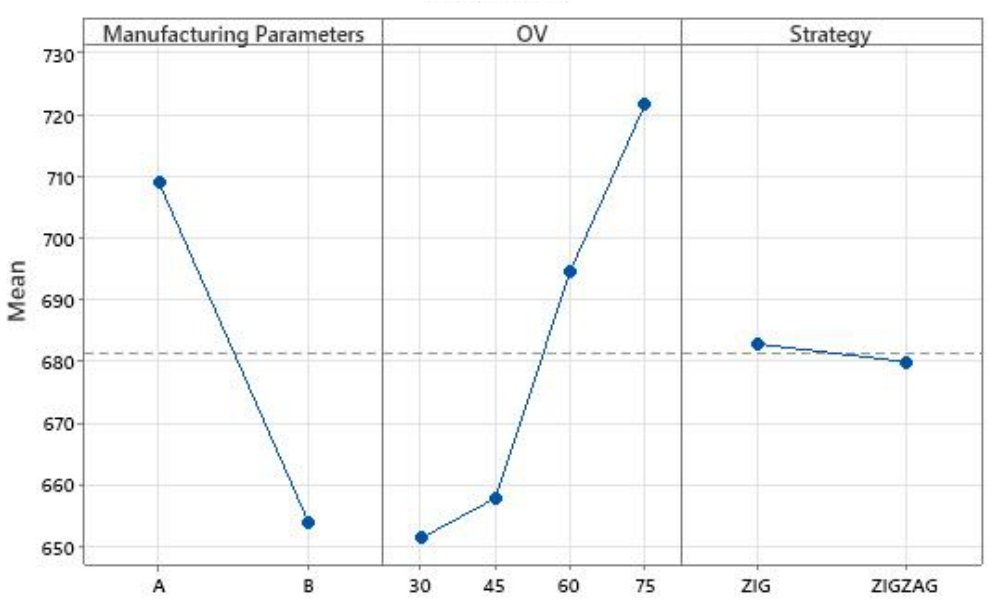

Figure 75: Main effects Plot for HV.

7.3.3.3 Metallurgical analysis

All 16 single layers have been analyzed via OM and using the HITACHI TM3000 SEM. Microstructures have been acquired along the layer's width (from point “a” to point “c” in Figure 76 and in the vertical direction, i.e. from the bottom to the top side of the SL, through the core). No relevant differences have been found in the microstructures between the various layers; consequently, an arbitrary case has been reported to avoid repetition. Specifically, SL deposited with scan strategy ZIG, combination A and OV 45%. Also in this case, it was employed the modified Vilella’s reagent to reveal the cross-section microstructures. The SEM micrographs of the single layer at the top, middle and bottom are shown, respectively, in Figure 77, Figure 78, Figure 79, according to the vertical direction indicated by points a, b and c in Figure 76.

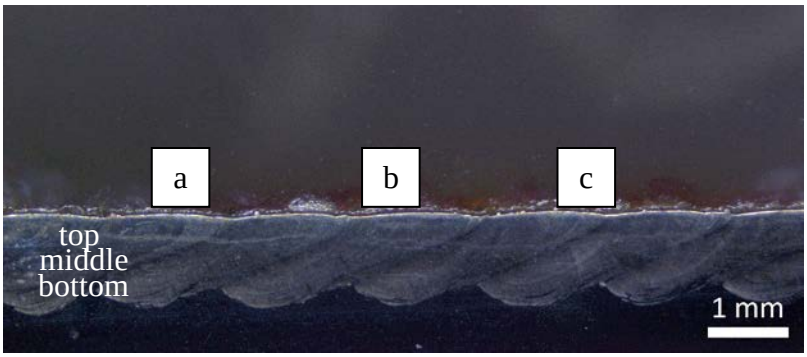

Figure 76: Optical macrograph at low magnification of the cross-section of an H13 single layer. Points a, b and c indicate the acquisition points in the vertical direction.

The considerations are similar to those done for the STs, explained in section 7.2.3.3. SEM micrographs show that the grain morphology is affected by the heat flux vector direction, as confirmed by Figure 80, which shows the microstructure of H13 at the interface with the 316L (not etched by the reagent), affected by the heat transport phenomena. It is evident that the direction of cooling goes from the center of the melting pool to the substrate.

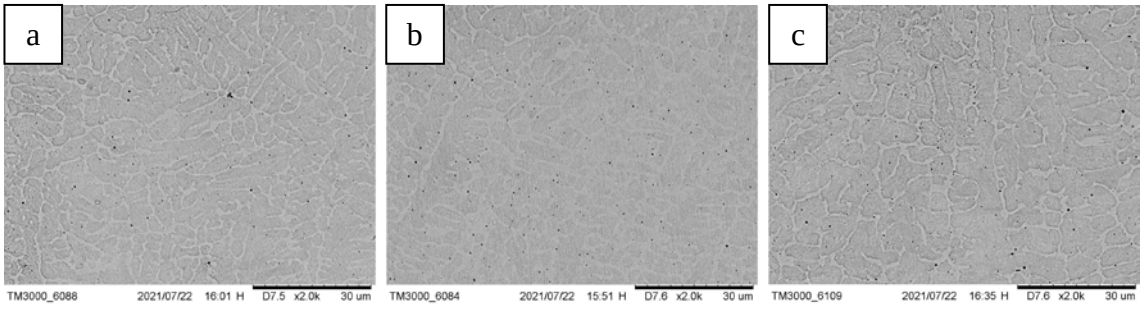

Figure 77: Micrographs at an elevated magnification at the top of the Single Layer; a, b and c indicate the vertical direction.

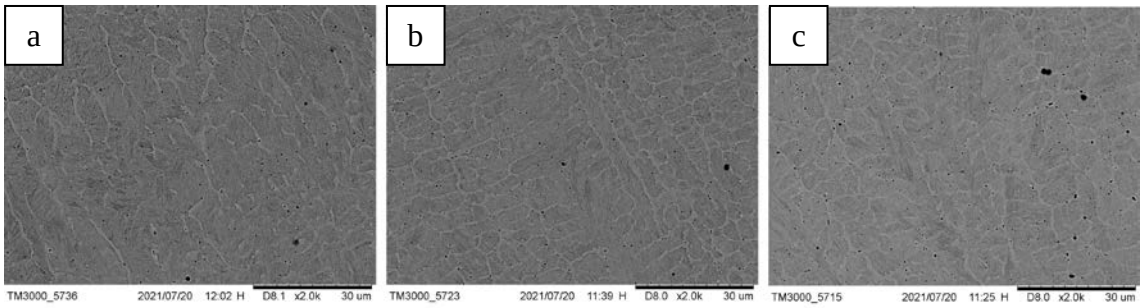

Figure 78: Micrographs at an elevated magnification at the middle of the Single Layer; a, b and c indicate the vertical direction.

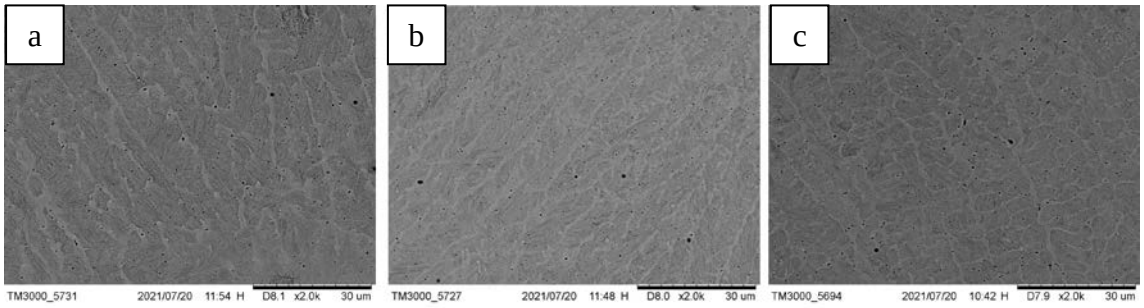

Figure 79: Micrographs at an elevated magnification at the bottom of the Single Layer; a, b and c indicate the vertical direction.

As reported for STs, also in the SL case, the DLD H13 is characterized by dendritic/cellular microstructures both in the bottom and middle regions of the single layers, with the presence of some equiaxed grains in the upper area. Moreover, it is important to highlight that no cracks and large porosities have been detected, but, as in the previous section related to STs, it can be noted the presence of micro-porosities and voids (due to entrained gases) in the grain boundaries.

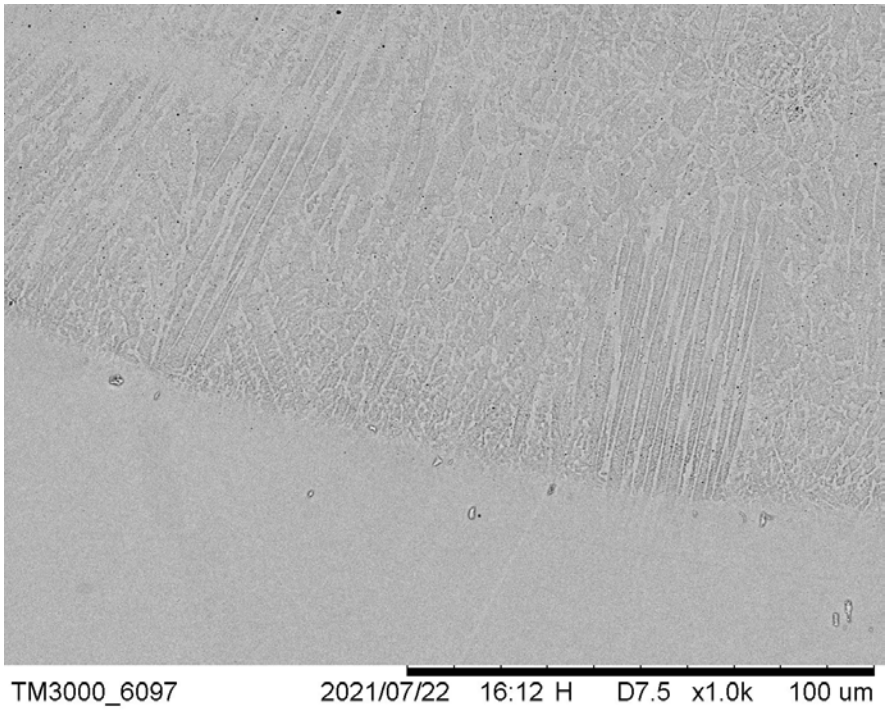

Figure 80: SEM micrograph of the interface between the H13 deposited on the 316L substrate, showing the direction of H13 structure.

In addition, also in the SLs analysis, brighter particles have been found (Figure 81), on which a line-scan EDX has been carried out.

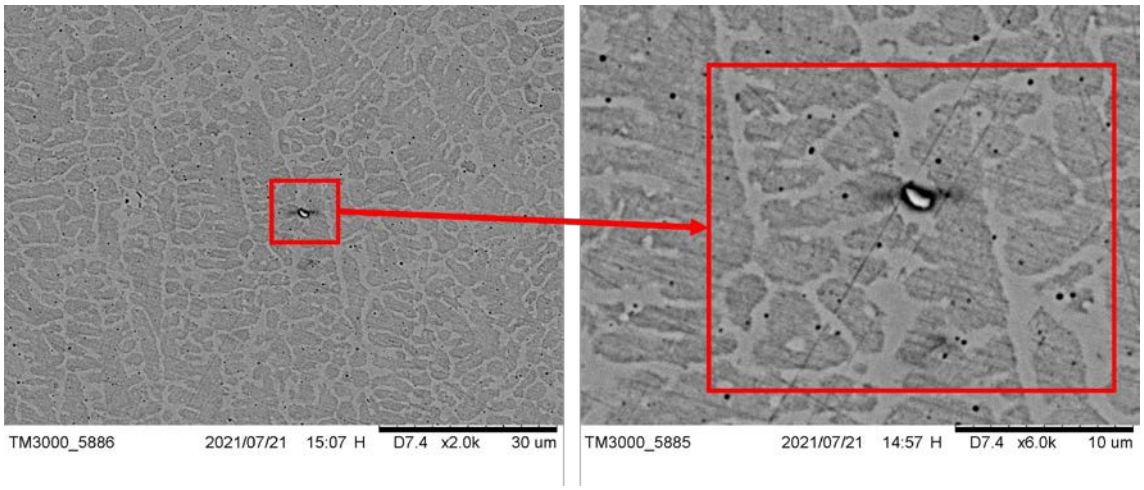

Figure 81: SEM micrographs of the center of a Single Layer at different magnifications, with a close-up on the brighter particle (carbide).

The results are shown the Figure 82. In Figure 82a, the yellow line represents the zone on which the EDX analysis has been conducted; its length is equal to the dimensional scale of the x-axis in Figure 82b. The diagram displayed an increment of Chromium and Molybdenum for the brighter particle, in accordance with the findings of Amirabdollahian et al. [84].

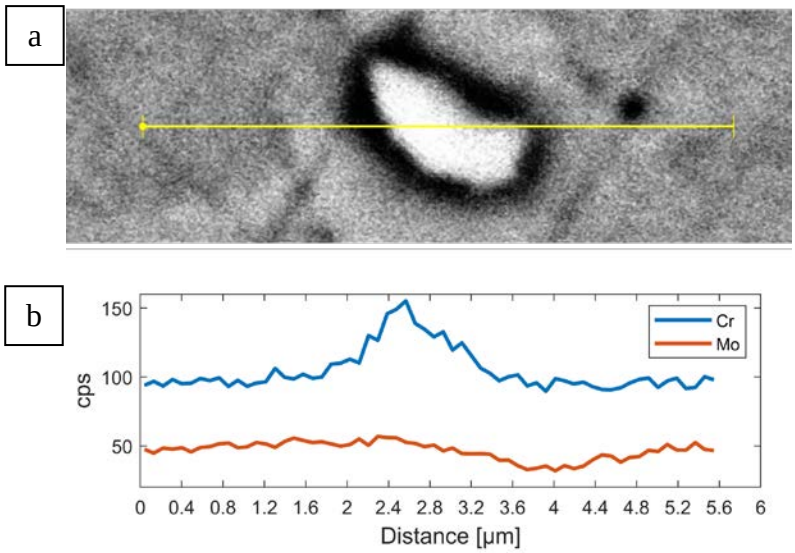

Figure 82: EDX analysis in line-scan form carried out on Cr- and Mo-rich zones.

7.3.4 Single Layers Conclusions

In this section, the main conclusions of a wide experimental campaign carried out on DLD of H13 single layers on a 316L stainless steel substrate will be reported. Based on STs analyses, two combinations of process parameters have been used (called A and B for the sake of brevity), with four different overlap values (30%, 45%, 60%, 75%) and two different deposition strategies (ZIG and

ZIGZAG). The results have been studied considering quantitative surface parameters, namely waviness and skewness, and microhardness, SEM and EDX analyses.

The outcomes have pointed out the following conclusions:

- In general, the waviness decreases as overlap increases until OV=60%, a condition in which the lowest value of waviness is reached, followed by an increment for OV=75%. In all the cases, the related skewness is near zero, ensuring the symmetry of waviness in the surface.
- The process is unstable when the overlap is equal to 75%, due to the over-deposition that strongly affects the waviness and leads to oscillations of the W_a values, as confirmed by the standard deviation that goes to the maximum value.
- Beyond the overlap, which is the most influential variable, the scan strategy and the process parameters A and B affect the waviness profile. Precisely, the ZIG strategy and the combination-B lead to a more uniform surface than the ZIGZAG one and combination-A in terms of waviness. This conclusion is also statistically confirmed.
- In all cases, the microhardness reaches high values, comparable to the literature, ranging from 600 to 700 HV.
- The deposition strategy does not affect the microhardness; on the contrary, the two investigated combinations of manufacturing parameters and the analyzed range of overlap are statistically influential.
- In conclusion, overlap equal to 60%, laser power equal to 2000W, and scanning speed equal to 1200 mm/min are the process parameters suggested to 3D print H13. This combination represents a proper trade-off between the optimum in terms of waviness and hardness, with a good metallurgical bond and with the absence of cracks or big voids.

7.4 Thin walls

This section aims to i) explore the feasibility of printing thin-walled structures using the DLD process, ii) better assess the influence of the deposition strategy, iii) study the influence of layer thickness on the geometrical accuracy and mechanical properties.

7.4.1 Experimental campaign

Two combinations of P, v and $\dot{m}_p$ have been used, i.e. P=1600 W, $\dot{m}_p$=15 g/min, v=1000 mm/min, and P=2000 W, $\dot{m}_p$=15 g/min, v=1200 mm/min (combination A and combination B, see Table 8). Three different layer thicknesses have been investigated: 0.4 mm, 0.5 mm and 0.6 mm, equal to a range from 60 to 90% of the height of the single tracks of the same material deposited with the same process parameters. Moreover, two kinds of deposition strategies have been studied, the Zig strategy and the ZigZag strategy.

7.4.2 Methods

Siemens NX has been employed to generate the G-code for thin walls depositions in Lasertec 65, according to the experimental campaign. Single walls made in H13 have been deposited on a 316L substrate, with a dwell time of 15 minutes between one deposition and another. Single walls have been cut and cross-sectioned via EDM in the middle of single walls to ensure the analysis of the section in which the process is stable. Then, the specimens have been hot mounted in an acid-proof resin, followed by the standard metallographic preparation [54]. The characterization analyses have been conducted on polished metallographic cross-sections after chemical etching with Vilella's reagent, employing OM and SEM, a Hitachi TM3000. Microhardness Vickers measurements have been performed on the metallographic cross-sections with a dwell time of 15 s, as suggested by the standard ASTM E92-82 [55].

7.4.3 Results and discussion

Trial experiments have been conducted before the presented experimental campaign, but the Zig strategy has been detected as not suitable for depositing single walls, due to the collapse of the structure (Figure 83a), a typical defect of thin walls produced via DLD [35]. On the other hand, with the ZigZag properties, only one acceptable result has been obtained (Figure 83b) in terms of shape.

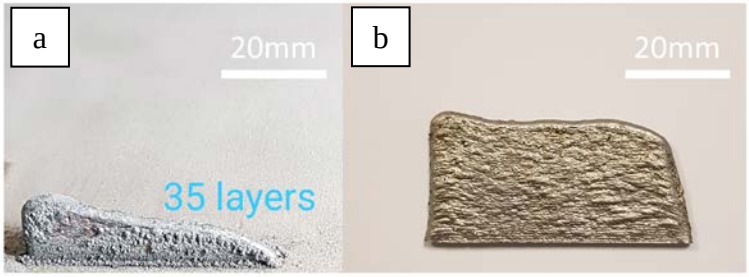

Figure 83: H13 single walls deposited with a) Zig and b) ZigZag Strategies.

The last-mentioned is the single wall deposited with P=1600W, v=1000 mm/min and thickness=0.6 mm. However, characterization analyses have been carried out on all the specimens produced with the ZigZag deposition strategy. All single walls printed with this strategy, after the EDM cutting, are shown in Figure 84.

Figure 84: DLD H13 single walls.

It is clear that the layer thickness influences the final result: the height increases with the layer thickness increase. On the premise that in the design project, the total height of the single wall is always 23 mm, and referring to Figure 84, it is evident that 0.4 and 0.5 mm are too low values for the layer thickness, which implies an incorrect position of the focal point of the laser and, consequently, affects the total height of the wall in combination with irregular shape. As above-mentioned, only one single wall has respected the design data and reached the desired height in combination with an acceptable shape (Figure 83b).

In addition, SEM analysis has pointed out the presence of several defects in each sample, such as cracks, porosities, voids and unmelted powders, as shown in Figure 85.

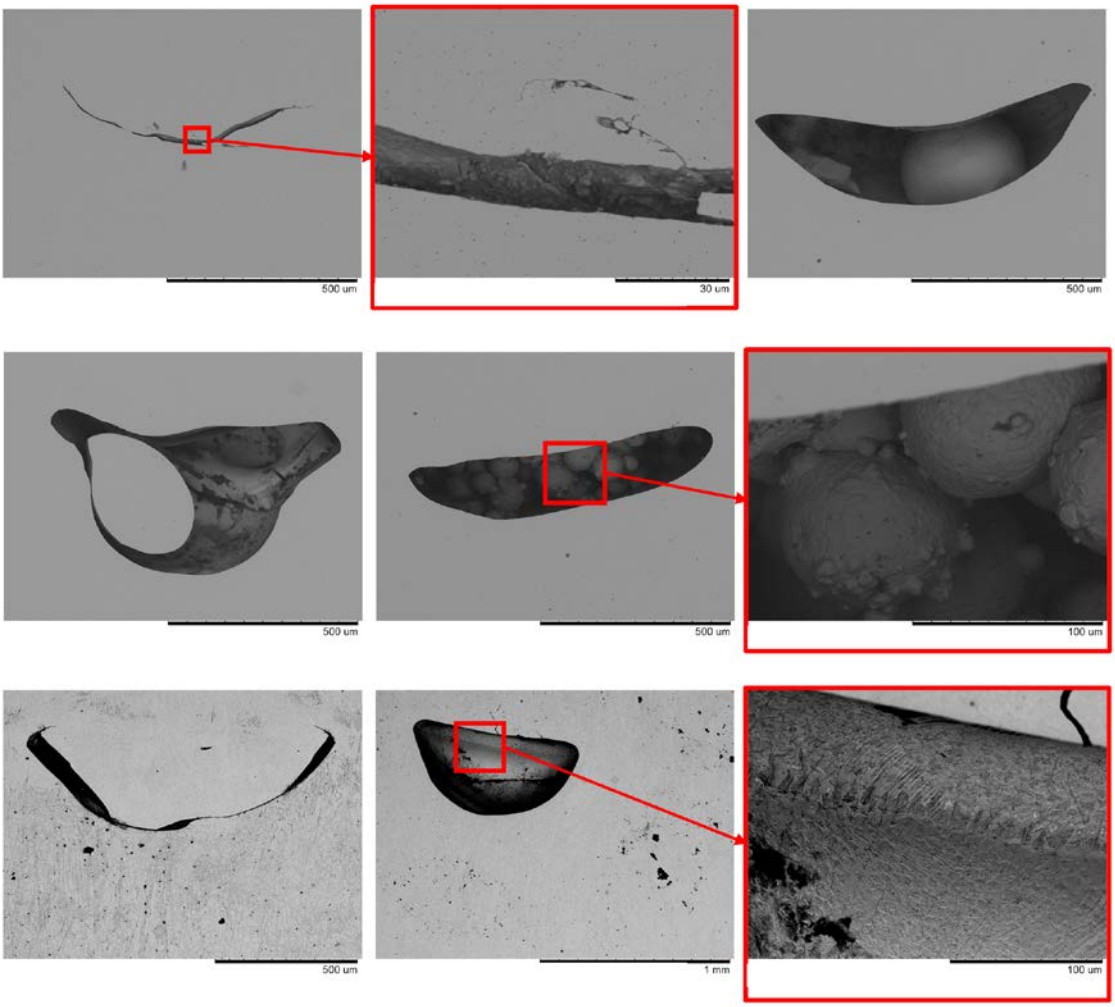

Figure 85: Defects of H13 thin-walled structures.

Although the presence of many defects, the mean value of the microhardness is near to one stated in literature, with an overall mean value of ~600HV, as shown in Figure 86.

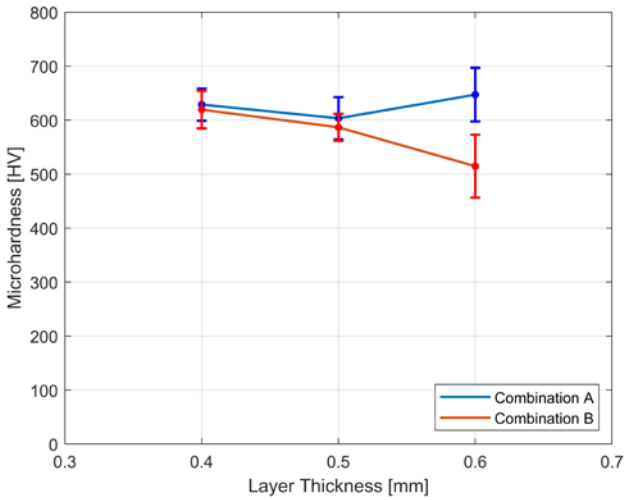

Figure 86: Microhardness and Std. dev. of H13 Single Walls versus Layer Thickness.

7.4.4 Thin Walls Conclusion

In this work, the potentialities of the Direct Laser Deposition process to print thin-walled structures have been investigated. For this aim, single walls of hot-work tool steel H13 have been deposited on a 316L substrate by varying both layer thickness and deposition strategies, with two combinations of process parameters. On the basis of the experimental outcomes, it is possible to answer the open questions designed in the introduction. The following conclusions can be drawn:

i) Thin-walled structures can be printed via DLD, with particular attention to decreasing the laser power in combination with increasing the layer. Specifically, for the H13, a reduction of 100 W for each layer has been assessed starting from the 4^{th} layer in the single walls.

ii) The deposition strategy strongly affects the final workpiece result; in particular, the Zig strategy is unsuitable for thin-wall structures. On the contrary, the Zig Zag strategy is recommended.

iii) The setting of the proper layer thickness is crucial to obtaining an acceptable geometrical accuracy result. The layer thickness suggested is equal to the 90% of the height of the single track deposited with the same process parameters, which is the case with the major microhardness value, ~630HV, in combination with the achievement of the total height stated in the design stage, for what concerns combination A. Nevertheless, on the basis that DLD could be a promising process for thin-walled structures, the experimental analyses have also pointed out several defects, such as voids, cracks and unmelted powders, suggesting the necessity of further research in this field.

In conclusion, the results are not satisfactory in terms of regular shapes and defects. It has been deduced that TWs analysis could not be an indicative step to the determination of three-dimensional bulk buildings, but a further and separated experimental campaign is needed in order to create thin structures.

7.5 FGMs structures

In this section, functionally graded materials have been analyzed. Four kinds of FGM samples have been deposited, with two different scanning strategies and varying percentages of feedstock materials, i.e. 316L and H13. On one side, there are gradual changes in the chemical composition (hereinafter graded structure); on the other side, an alternation of the two materials (hereinafter wafer structure). At the end of the section, several answers to the opening questions will be provided: i) is it possible to print Graded and Wafer structures?, ii) are the properties of the obtained material adequate to the metallurgical and mechanical requirements?

7.5.1 Experimental campaign

Two types of FGM samples have been built:

- Graded structure (G): the material composition gradually moves from 100% of 316L to 100% H13, scheme in Figure 87a;
- Wafer structure (W): is an alternation, layer by layer, of 316L and H13, with the first layer of 316L, scheme Figure 87b.

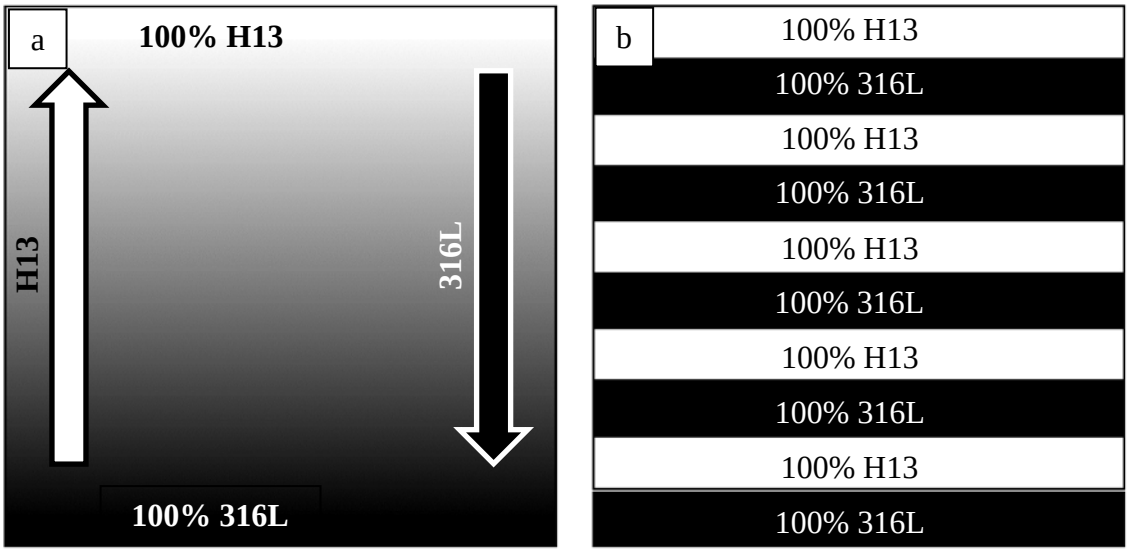

Figure 87: Schematization of the investigated Functionally Graded Materials specimens: a) graded, b) wafer.

Moreover, the two scan strategies of the SLs experimental campaign have also been investigated for the FGM cases: ZIG (Z) and ZIGZAG (ZZ), for a total of 4 different kinds of FGM structures concerning H13 and 316L. The summarized experimental campaign is visible in the following Table 13.

SAMPLE no.	Sample name	Deposition Strategy	Acronyms
1	Graded	ZIG	GZ
2	Graded	ZIGZAG	GZZ
3	Wafer	ZIG	WZ
4	Wafer	ZIGZAG	WZZ

Table 13: Experimental campaign of FGM structures.

7.5.2 Methods

7.5.2.1 FGM structures fabrication via DLD process

Based on the findings of the previous sections, the optimum in terms of process parameters has been used, i.e. $\dot{m}_p$=15 g/min, v=1200 mm/min, OV=60%. Siemens NX has been employed to produce the code for depositions in Lasertec 65 (Figure 88). The substrate used is 316L stainless steel with a dimension of 200x200x20 mm^3. It has been sandblasted and degreased with acetone before the deposition process.

Figure 88: Direct Laser Deposition process of FGM structures in Lasertec 65.

Blocks of 120x50x8 mm^3 have been deposited to extract samples of 116x10x6 mm^3 and specimens for the material characterization. It is worth recalling the fixed process parameters: the spot diameter of 3 mm, focal length of 13 mm, career gas and shielding gas (Argon) with a flow rate of 5 l/min and 6 l/min, respectively. The layer thickness has been set to 0.8 for a total of 10 ten layers. In the G-code file exported by Siemens NX, for the GZ structures, the first two and the latest two layers are composed, respectively, of 100% 316L and 100% H13, in order to consider the waste of material during the cutting process. Since the first material deposited in the FGMs specimen is always

composed of 100% 316L, the laser power value suggested by the manufacturer for 316L has been used as starting power. It was set equal to 1800 W for the first layer, with a drop of 100 W until the 3rd layer (1600W) and, then, another reduction of 50 W for each layer until 1200 W. The last power reductions have not been planned in the original file, but they resulted as a necessary action due to excessive heating of the laser lens. In this context, the operator's experience and attention to the monitoring apparatus are essential during the DLD process. The Lasertec 65 is equipped with a thermo-camera that is able to monitor the melt pool temperature and the temperature of the protection glass of the laser nozzle. When the glass becomes extremely hot, it is necessary to reduce the laser power, it can be done directly during the process using the touchscreen of the monitoring apparatus.
The ZIG and ZIGZAG deposition strategies employed for the process are illustrated in Figure 89, it is possible to note that both rotate at 90° every successive layer. Moreover, Siemens NX allows to choice of the starting point of the deposition; based on previous experiments, it was imposed to change every layer in the order represented in the figure (the red points indicate the start of the printing process of the layer of interest). It was found that this sequence improves the surface quality of the final object, resulting in a more uniform top surface. A contour strategy has been applied, with an overhang equal to 50% of the tool dimension (it defines how much of the deposited material can outflow the edges of the solid model).

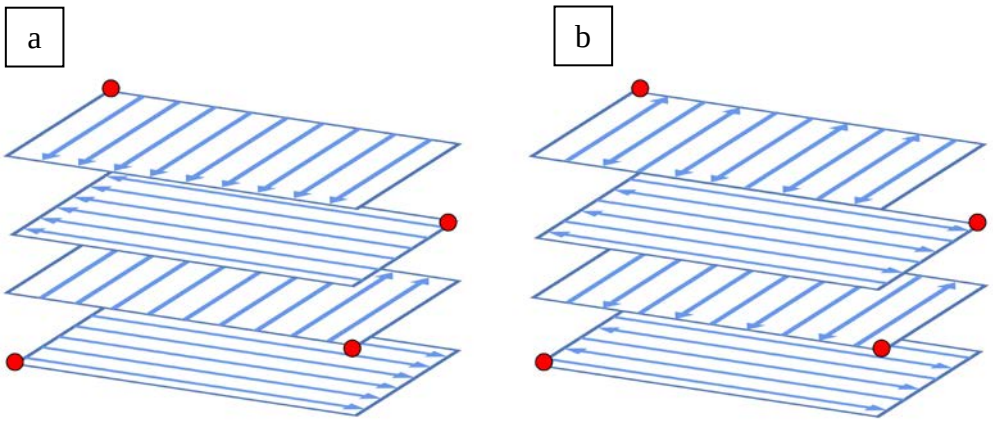

Figure 89: Deposition strategies with the indicated starting point (red points): a) Zig strategy, b) ZigZag strategy.

For the sake of clarity, the contour is visible in Figure 90 within the red circle, moreover, the directions of the deposition strategy are indicated by the white arrows for the two layers. It is possible to understand the deposition strategy employed by seeing the layer aspect: in the case of Figure 90, the tracks have the same shape at the end and at the beginning of the line, and indeed it represents the Zig specimens.

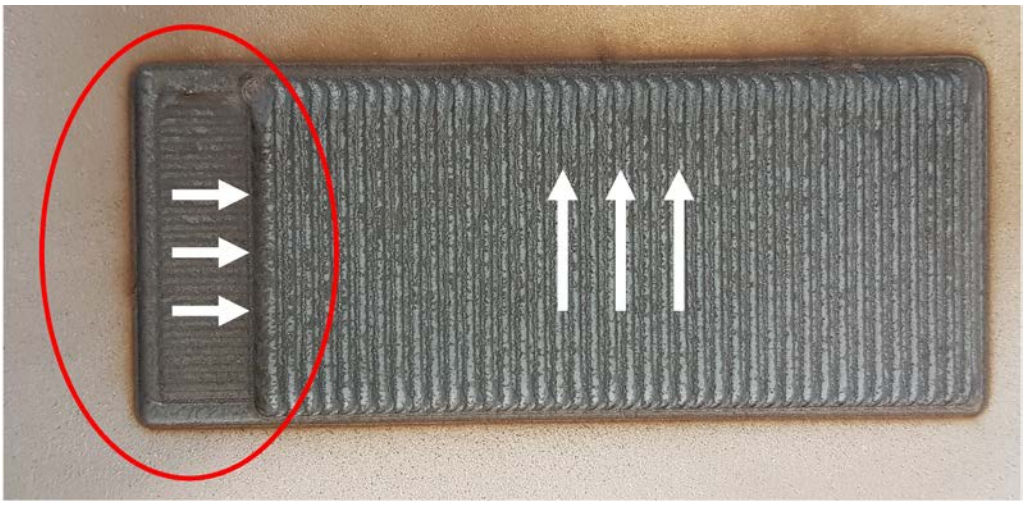

Figure 90: 316L-H13 Graded sample produced with the Zig deposition strategy.

In conclusion, the variations in terms of powder feed employed for the experimental campaign are summarized in the following Table 14 from the first to the last layer.

	Graded (Zig and ZigZag)		**Wafer (Zig and ZigZag)**	
Layer no	Powder Feed 316L	Powder Feed H13	Powder Feed 316L	Powder Feed H13
1	100%	0%	100%	0%
2	100%	0%	0%	100%
3	85%	15%	100%	0%
4	70%	30%	0%	100%
5	55%	45%	100%	0%
6	40%	60%	0%	100%
7	25%	75%	100%	0%
8	10%	90%	0%	100%
9	0%	100%	100%	0%
10	0%	100%	0%	100%

Table 14: Powders percentages variation in Graded-Zig and Graded-ZigZag, Wafer-Zig and Wafer-ZigZag.

7.5.2.2 Characterization

Deposited blocks have been cut via electrical discharge machining, obtaining four samples for each combination. One specimen was cut, cross-sectioned, and hot mounted in an acid-proof resin. The metallographic preparation has included water-cooled silicon carbide paper (200 mm diameter) for the grinding stage; the grit size selected also depends on the technique used to generate the cut surface. The used grit sequence was 240, 320, 400 and 600-grit, with a grinding time of 4 minutes. Then, specimens were polished in three stages, with 9, 6 and 1 μm diamond abrasive suspension to the polishing cloths. The polishing time was 5 minutes [54].

Microstructure characterization was performed by means of light OM and SEM on polished metallographic cross-sections after chemical etching with modified Vilella's. Microhardness Vickers measurements were conducted on the metallographic cross-sections with a dwell time of 15 s, as suggested by the standard ASTM E92-82 [55]. In the graded and the wafer structures, a step-size of 1 mm was used in both the horizontal e vertical direction. The vertical direction started from the bottom, deposited with 0% of H13 powders and with 100%316L powders, and ends at the top of the samples, deposited with 100% of H13 powders and with 0%316L powders, concerning the graded structure. In the wafer structure, the vertical direction started from the bottom, represented by the first layer deposited with 100% 316L powders and 0% H13 powders.

7.5.2.3 Experimental mechanical set-up

Three-point bending tests have been carried out by employing a universal testing machine (Galdabini QUASAR 50, Galdabini SPA, Italy) with a load cell of 50 kN at room temperature and with support holders of 10 mm diameter. The Quasar 50 is a testing machine with displacement control. The cross-head speed was set equal to 1 mm/min. It is equipped with associated software, LabTest™, that allows to set the tests correctly and check the condition of tests at each moment. Three specimens, 116x10x6 mm^3, have been tested for each experimental condition; the support span was equal to 96 mm respecting the 16:1 span-thickness ratio [112], with an over-span of 10 mm on each side. Figure 91a and Figure 91b show, respectively, the scheme of the test and the real experimental set-up, in which the sample is placed horizontally on two support holders and submitted to a vertical force from above.

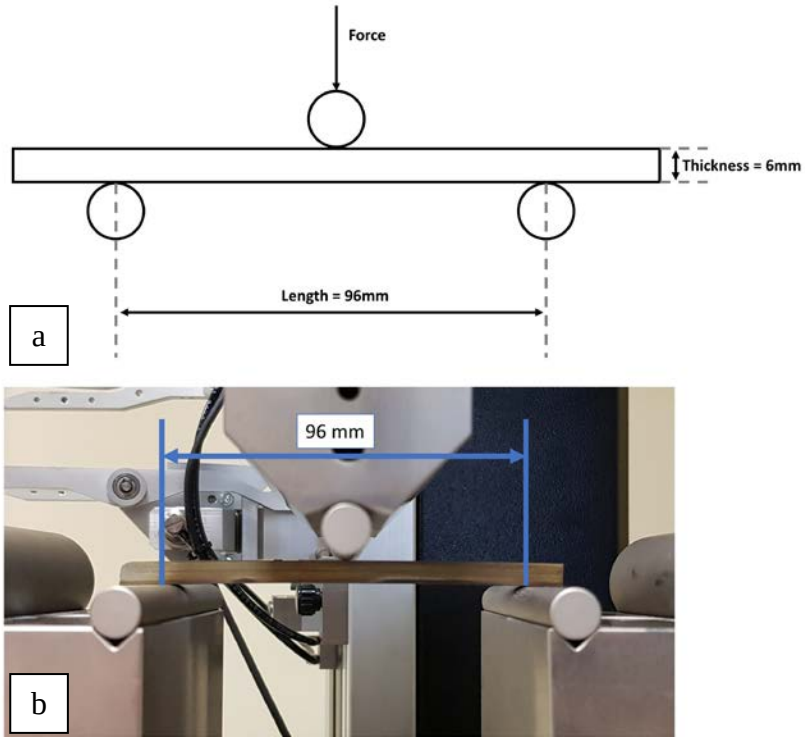

Figure 91: Three-point bending test. a) scheme of the test and b) experimental set-up.

7.5.3 Results and Discussion

The cross-sections of the samples etched using the modified Vilella's reagent are shown in Figure 92. Since the components are FGMs, the various zones of the cross-sections have different chemical compositions, and since the etching procedure is unique for all the specimens, it is impossible to obtain clear macrographs.

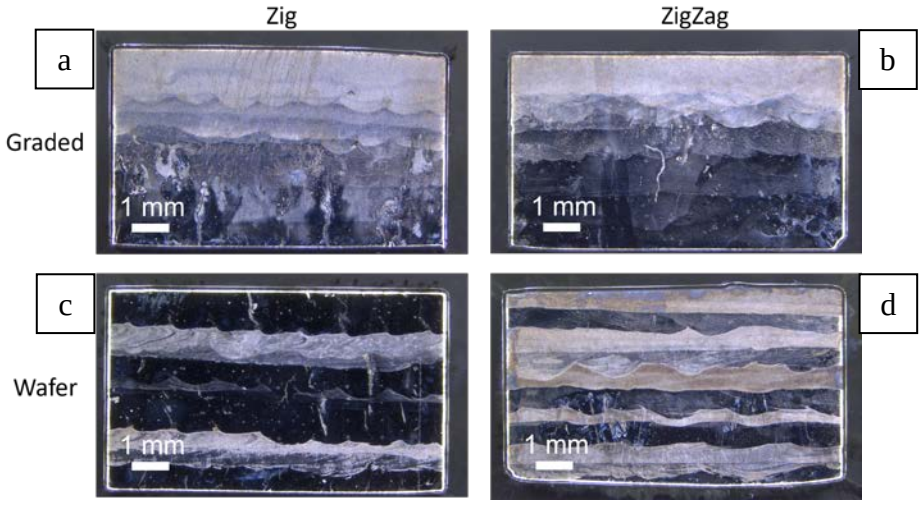

Figure 92: Optical macrographs of the cross-section of FGM 316L-H13 samples: a) Graded Zig, b) Graded ZigZag,c) Wafer Zig, d) Wafer ZigZag.

The samples with a rectangular cross-section for 3PB tests, after the cutting via EDM, are visible in Figure 93.

Figure 93: Graded and Wafer specimens, deposited with Zig and ZigZag strategies, for 3PB tests.

7.5.3.1 Microhardness analysis

A microhardness analysis has been carried out on the cross-sections of samples of the experimental campaign; the mean values with the relative standard deviation are displayed in Figure 94 and Figure 95. As expected, the results obtained concerning the graded sample (Figure 92), both GZ and GZZ, show an increasing trend from the bottom to the top. Indeed, at the bottom, when the percentage of H13 is zero (in the first layer), the hardness of the 316L is around ~200HV, a value higher than conventional wrought manufacturing 316L and comparable to the additive manufacturing one [113], [114].

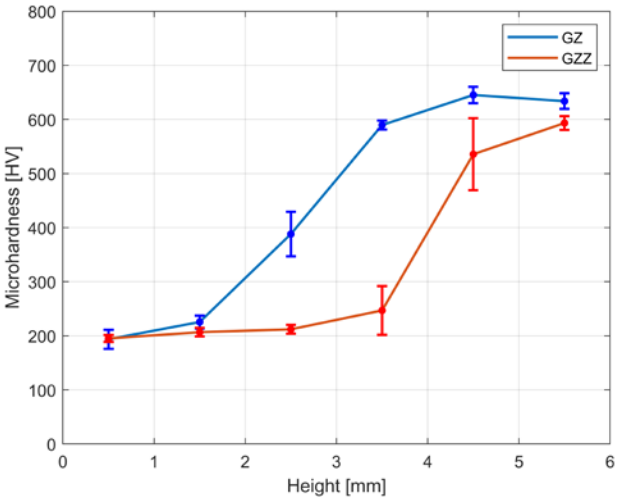

Figure 94: Microhardness of Graded structures (G) versus the height of the sample, according to the Zig (Z) and the ZigZag (ZZ) deposition strategy.

The hardness increases as the H13 percentage increases, reaching a very high value of hardness (~700HV). In particular, using the zig deposition strategy, the result obtained is an entirely gradual increasing of the hardness till to reach the perfect mean value of hardness (~450HV) between the 316L and H13 HV hardness, at the middle of the sample and so when there is a 50% of 316L and a

50% of H13. It reveals the perfect miscibility of the materials and indicates that the parameters chosen didn't affect the hardness properties of both 316L and H13 also in the FGM 3D structures, ensuring hardness values comparable with the single material component. Concerning the difference in HV in the internal graded layers between the Zig and ZigZag deposition strategies, they are probably due to the repetitive passes of the heat source for the SZZ case; indeed, as explained before, in this case, the laser act on a less solidified material compared to the zig strategy, this allows to 316L of the layer *n-1* to be mixed with the powders of layer *n* during the deposition process, resulting in a major total amount stainless steel material in respect to the one of the same layer in the sample SZ. Indeed, also seeing Figure 92a, it is possible to note that the darker material (316L) gradually disappears from the bottom to the top, on the other hand, in Figure 92b, 316L has a permanent presence until 2.7 mm, in accordance with the microhardness values detected for GZZ (Figure 94). Figure 95 shows the microhardness along with the height of WZ and WZZ; it is possible to notice that the alternation of the layers is respected and results in an alternation of microhardness.

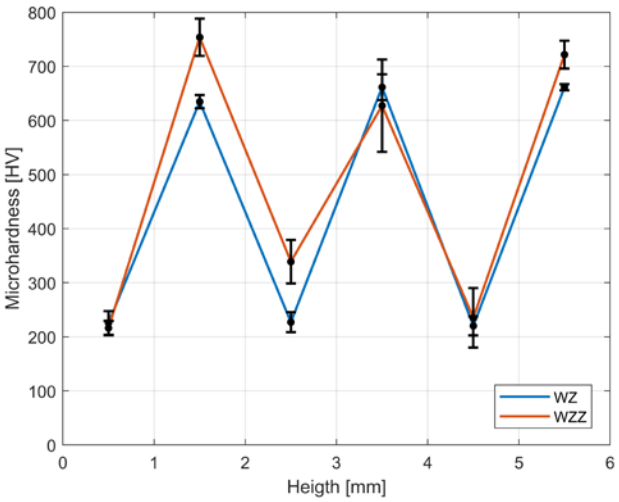

Figure 95: HV of Wafer structures (W) versus the height of the samples, according to the Zig (Z) and the ZigZag (ZZ) deposition strategy.

7.5.3.2 Metallurgical analysis

All the specimens have been analyzed via OM and using the HITACHI TM3000 SEM. Micrographs have been acquired along with the height of the FGM structures, from the bottom to the upper region in the GZ and GZZ samples; in WZ and WZZ ones, micrographs have been acquired at the interface between the two materials and at the layers corresponding to 316L and H13. Figure 96 and Figure 97 illustrate the microstructural evolution of the graded structures of, respectively, Zig and Zig Zag conditions. The first consideration is that the deposition strategies don't affect the microstructure of the material, but only the evolution, in other words, the layer in which they have been detected.

Specifically, in the GZZ sample, the passage from 316L to H13 microstructures has been detected in a higher position along with the height, as shown in the figure.

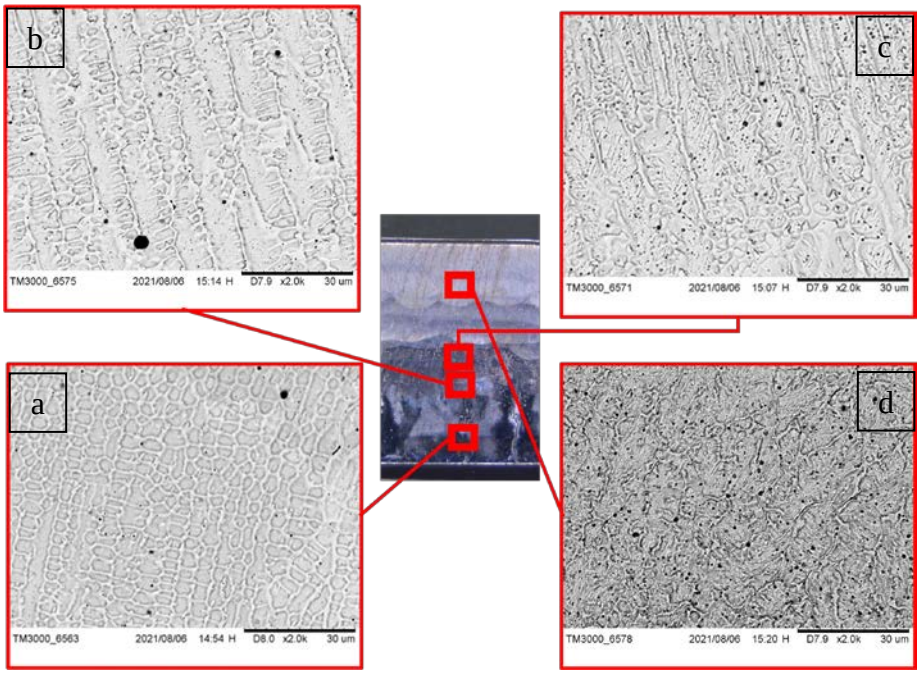

Figure 96: Micrographs of Graded Zig sample: a) bottom (316L), b) and c) middle (mix 316L-H13), and d) top (H13).

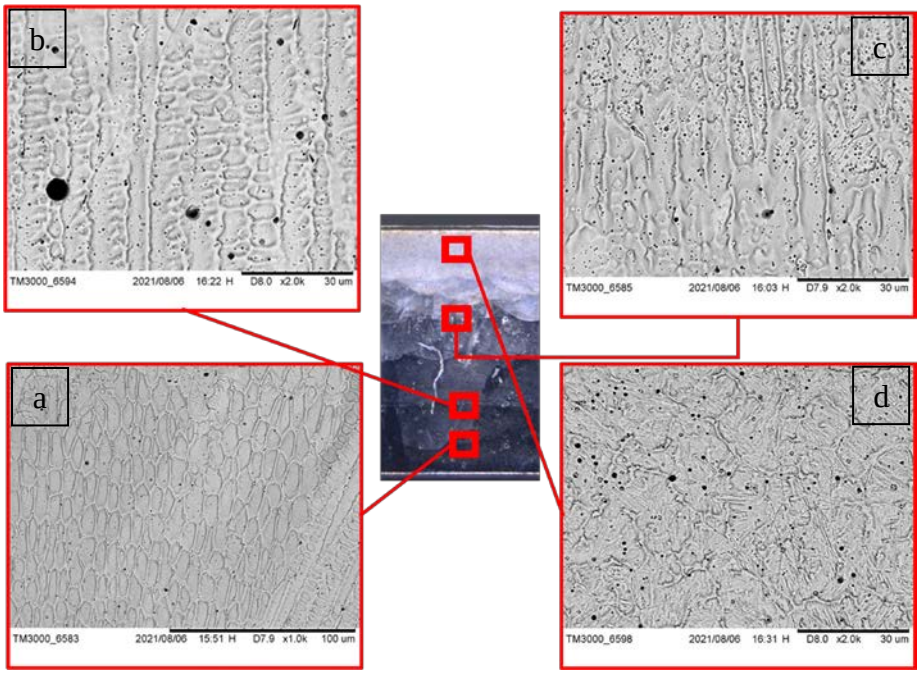

Figure 97: Micrographs of Graded ZigZag sample: a) bottom (316L), b) and c) middle (mix 316L-H13), and d) top (H13).

Figure 96a and Figure 97a show the typical austenitic microstructure that characterized DLD 316L [113], [115]. During the growth of the item, the temperature and the cooling rates undergo variations

and this unstable condition determines the coexistence of different microstructures within the same sample. At the top of the sample, it is possible to note the microstructure of H13 described above, i.e. lath martensite surrounded by retained austenite. Near the bottom, there is a structure characterized by equiaxed, fine grains due to the high solidification rate caused by the efficient heat dissipation related to the presence of the substrate. Moving away from the bottom and focusing on a more central area (Figure 96b and Figure 97b), grains characterized by larger dimensions and dendrites have been found due to remelting caused by the passage of the laser beam, which represents a thermal stimulation for the growth of the grain. Furthermore, this region is not close to the substrate or in contact with the external atmosphere, and so the path of heat dissipation is much more complicated and reduced; for this reason, it is characterized by a coarse microstructure. Another aspect regards the orientation of elongated austenitic grains, indeed as also declared by Yadollahi et al. [115], in each layer, the orientation of the columnar grains is inclined to move from the building direction (vertical) to the direction of the laser beam or the direction of movement of the molten bath. Figure 96c and Figure 97c show the gradual passage from 316L to H13 and so from the austenitic to the martensitic microstructure. Figure 96d and Figure 97d display the typical DLD H13 microstructures above described.

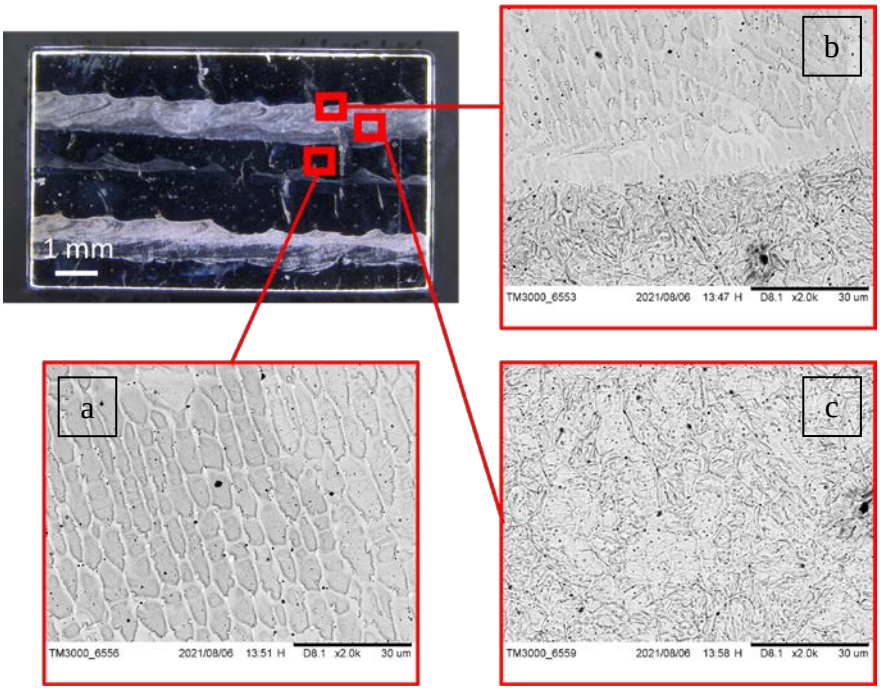

Figure 98: Micrographs of Wafer sample: a)interface between 316L and H13, b)316L, c)H13.

In addition, at the top of the item, it is possible to note the presence of equiaxial grains again, in this case, finer ones, since the high heat loss due to convection and radiation phenomena that occur due to contact with the external atmosphere. The same considerations can be made for the Wafer samples

(Figure 98), with the difference that the passage from one material microstructure to another was not gradual. In Figure 49b), it is clearly visible the difference between 316L (up) and H13 (down).
In conclusion, EDX analyses have been carried out, and the results are shown in Figure 99 and Figure 100. The presence of chromium, nickel (elements present in 316L, see Table 3) and vanadium (element present in H13, see Table 4) have been investigated. The first figure shows the influence of the deposition strategies on the chemical composition of the items along with the height, resulting in a more persistent presence of 316L steel in the bottom/ middle part of the product. This is also confirmed by the EDX line spectrum of the Wafer sample (Figure 100): in the Zig case, a substantial drop of Chromium and Nickel has been observed in all the passages from the 316L layer to the H13 layer; this does not happen in the WZZ items, probably due to the phenomena explained in section 7.5.3.1.

Figure 99: EDX line spectrum along with the height of the Graded samples.

Figure 100: EDX line spectrum along with the height of the Wafer samples.

7.5.3.3 Mechanical analysis

Six types of three-point bending conditions have been carried out, summarized in Table 15.

Condition no	Samples	Condition characteristic	Acronyms
1	GZ	100% H13 layer as outward lower surface	GZ-H13
2	GZ	100% 316L layer as outward lower surfaces	GZ-316L
3	GZZ	100% H13 layer as outward lower surface	GZZ-H13
4	GZZ	100% 316L layer as outward lower surface	GZZ-316L
5	WZ	-	WZ
6	WZZ	-	WZZ

Table 15: Three-point bending tests conditions.

The results of the tests related to the Graded structures are displayed in Figure 101.

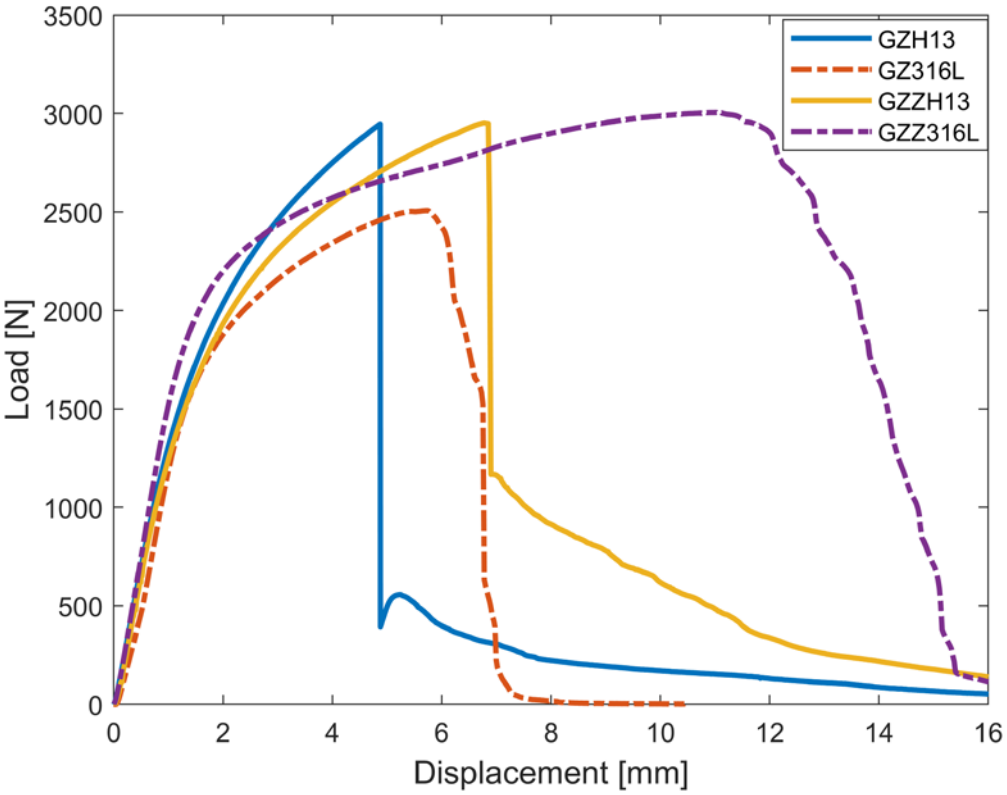

Figure 101: Graded Structures: Load-displacement curves illustrating the estimated mechanical properties.

In the first condition, concerning GZ, a linear relationship between load and displacement up to 1000 N is observed for a displacement range of 0-1 mm. The specimens show deformations without breaking up until displacements of ~5mm, the breaking load exceeds 2500N, reaching the first peak of ~2900N. Then, a brittle failure occurs, which propagates for most of the thickness of the specimen starting from the extrados surface; at the instant which this happens, the force reaches values below 500N, the crack propagation is blocked by encountering the closest layers to the intrados made of predominantly 316 L steel. Therefore, the material shows an increase in fracture toughness which makes it necessary to increase the load further to advance the fracture, so a second peak load occurs. At this point, the failure of the specimen progresses in a ductile mood between the layers mainly composed of 316L steel, which is capable of accumulating large plastic deformations.

In the second condition related to GZ structures, the extrados surface, where the maximum stresses act, is made up of a layer with a composition of 100% 316L, a material able to deform more before breakage than to steel H13. As it is known, materials prone to accumulate greater plastic deformations, as is the case of 316L compared to H13 steel, hardly yield with cracks due to cleavage and show greater fracture toughness with the same defects present in the volume of material. Summarizing, in the case of the GZ-316L specimens, a completely ductile fracture occurs, with large

deformations that progress with the applied load, reaching maximum values of force equal to ~2500N in combination with displacement close to 6 mm.

Regarding the GZZ-H13 condition, there is a linear relationship between load and displacement up to 1000N and a displacement of 0.7 mm, a slightly higher stiffness than Graded specimens made with the Zig scan strategy and aligned in the same way during the test (GZH13). The maximum force reaches ~3000N at a failure displacement of ~7 mm, which is also larger than the corresponding failure displacement for the GZ-H13 specimens, therefore the fracture toughness is higher for GZZ-H13. Failure is observed to propagate in two steps. The first part is represented by a brittle failure that starts from the above-mentioned failure displacement and continues from the extrados surface through the layers with a predominant composition of H13, resulting in a reduction of the load from 3000N to 1200N. In the second part, characterized by ductile failure, the crack propagation slow down by encountering the layers near to the intrados made of predominantly 316L steel.

Also in the GZZ-316L, there is a linear relationship between load and displacement up to ~1500N and displacement of 1mm, a stiffness comparable to that shown by Graded specimens made with the Zig scanning strategy and oriented in the same way during the test (GZ-316L). The maximum force reaches ~3000N with a displacement at the failure of ~12 mm, approximately double that the one evaluated for the GZ specimens equally oriented during the test. A brittle failure occurs when the maximum value of the applied force reaches ~3000N at a displacement close to 11 mm. Then this value, with increasing applied loads, the crack propagation slows down by encountering the layers near to the intrados made of predominantly 316L. It shows a ductile behavior equal to the one of GZ-316L, but this type and orientation of the specimens is the one that, compared to all the others tested, shows greater ductility, greater stiffness during the linear link between load and displacement, and greater fracture toughness.

The results of the tests related to the Wafer structures are displayed in Figure 102.

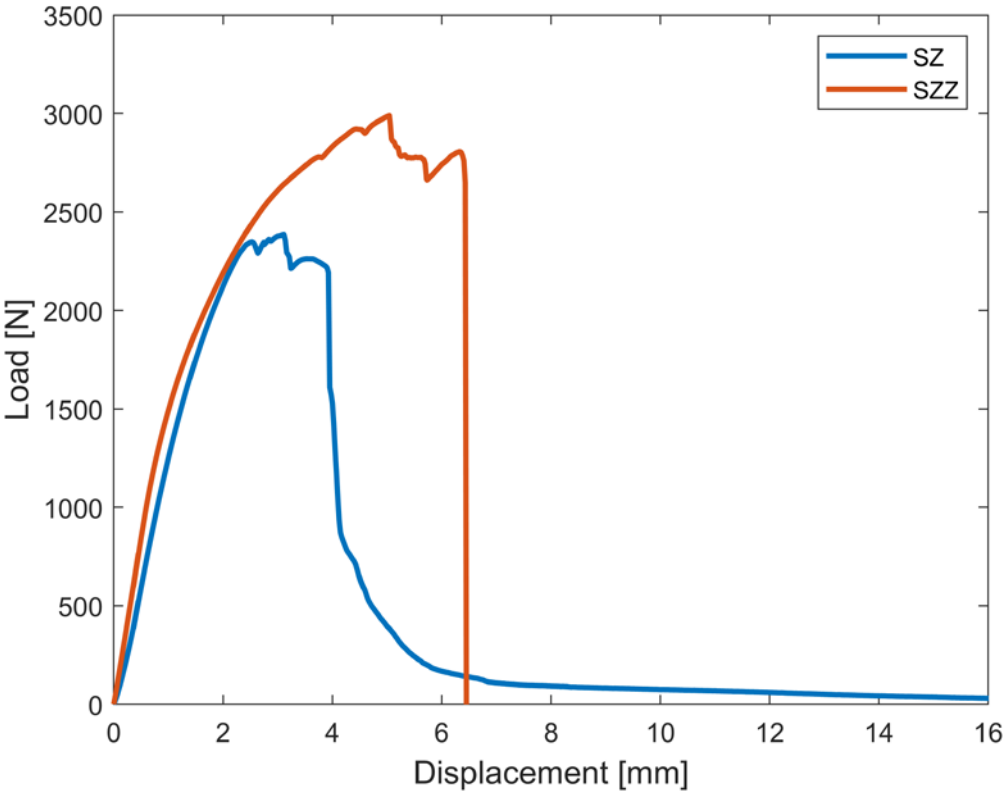

Figure 102: Wafer Zig and Zig Zag: Load-displacement curve illustrating the estimated mechanical properties.

For the WZ condition, in which samples with alternate layers of 316L and H13 and deposited in ZIG way, there is a linear relationship between load and displacement up to 1500N and displacement close to 1mm. The maximum force ranges from 2200 to 2600N, with a mean value of 2500N, with a related displacement of about 2.5 mm. From this point, a blended failure mode occurs, it can be considered both brittle and ductile. The first fracture starts from the extrados surface of the inflected specimen, in correspondence with the most stressed section, an area in which the maximum tensile stresses are reached. At this point, although the fracture begins after a displacement of about 2.5 mm, a brittle failure of the entire specimen is not observed, which still offers a flexural stiffness up to a deflection of 4 mm, after which the force rapidly collapses to zero. In the range between 2.5 and 4mm, there are failures of the successive layers that make up the volume of the specimen in which the propagation of the fracture is blocked when it encounters the interface between two layers. If the layer is mainly composed of 316L, small increases in the load are necessary to bring the fracture to expand to the following interface, if the layer is mainly composed of H13, there is a collapse of resistance to deformation of the specimen and the force is sharply reduced.

Also in the last condition, namely WZZ, there is a linear link between load and displacement up to a displacement of about 1 mm, but unlike the previous case, the load exceeds the value of 1000N during

linear behavior. In other words, the slope of this section is greater than in the case of Z-type specimens (WZ), so a greater stiffness is observed in Wafer specimens made by means of a Zig-Zag type scanning strategy. After the linear link between load and displacement, no fractures occur until a value of displacement of ~3mm is reached, after which a mixed behavior of the failure is found. Also in the WZZ condition, indeed, in some cases, fragile fractures occur, characterized by a reduction of the load in combination to very short displacement, in other cases, ductile fractures appear, characterized by a slow propagation that sees an increasing or, at the most, constant load while the displacement increases. Before the fracture is generated, the applied load reaches values between 2500 - 3000N, the specimen deforms without failing, up to loads slightly greater than those of the Z-type specimen. Therefore the specimens made by means of a Zig Zag scanning strategy are characterized by a higher fracture toughness than SZ.

However, it has been noted that in all the conditions performed, despite the effects due to the shear, characteristic of the three-point bending tests and accentuated by the non-homogeneous characteristics of the tested material, the delamination effects do not occur, the fracture propagates between the layers in the direction of the thickness of the specimen and not in the direction of the interface between the various layers of graded and, above all, sandwich items, as shown in Figure 103, this suggests that there is a robust metallurgical bond at the interface between the layers, that acts as a novel single material.

Figure 103: Bending failure in Functionally Graded Materials produced via DLD.

7.5.4 FGM Conclusion

In this section, functionally graded materials are analyzed. Four types of FGM samples were deposited with two different variations in the chemical composition, Graded and Wafer, and two deposition strategies, Zig and Zig Zag. In the Graded components, there is a gradual decrease of 316L and an increase of H13 from the bottom to the top. In the Wafer structures, layers of 316L and H13 are alternated.

All specimens have been characterized and mechanically tested through microhardness, SEM, EDX analyses, and three-point bending tests. At this point, it is possible to answer the opening questions declared in the introduction of the section:

i) It has been demonstrated that the Direct Lased Deposition technology is a promising technology for manufacturing Graded and Wafer parts. It was confirmed by the gradual changes in the chemical composition in the Graded component and by changes with a stair-step effect in the Wafer one.

ii) The properties of the new 316L-H13 material obtained are compliant with the metallurgical and mechanical requirements. Indeed, after the correct balance of the most influent process parameters, it is possible to change the chemical composition in order to obtain tailored microstructure in different zones of the same component, resulting in customized properties, and this is the nature of Functionally Graded Materials.

In particular, the microstructural evolution has involved the transition from austenitic 316L to H13, predominantly made up of lath martensite, from the bottom to the top in the Graded structure and at the interface between layers in Wafer components. The hardness has gradually changed from ~200HV, the typical hardness of 316L, to ~700HV, the DLD hardness value of H13, with intermediate values in the Graded structures' transition zone. In the Wafer structures, microhardness alternates the above-reported values. Both deposition strategies studied, namely Zig and ZigZag, have respected the metallurgical and hardness requirements, with a major reflection of design data in the Zig strategy. Moreover, the FGMs have not shown delamination between layers under bending stress, performing brittle and ductile failures, depending on 316L and H13 in the extrados layers in the Graded components, and a mix of brittle and ductile failures in Wafer components.

Chapter 8. Benchmark Production

In this Chapter, FGMs have been fabricated as benchmarks of the developed knowledge to verify the process parameters and validate the manufacturing guidelines explained in the previous chapter.
Two DLD cubes with a size of 25x25x25 mm^3 have been deposited. The first one, with a Graded structure, has been printed with a layer-by-layer increment of 5% in the H13 composition, associated with a relative reduction of 5% of the 316L. The second specimen, with a Wafer structure, has been manufactured by alternating layer-by-layer 316L and H13. EDX and microhardness analyses have been carried out. The results of the chemical analysis of the Graded cube in the top and bottom zones are, respectively, shown in Figure 104 and Figure 105.

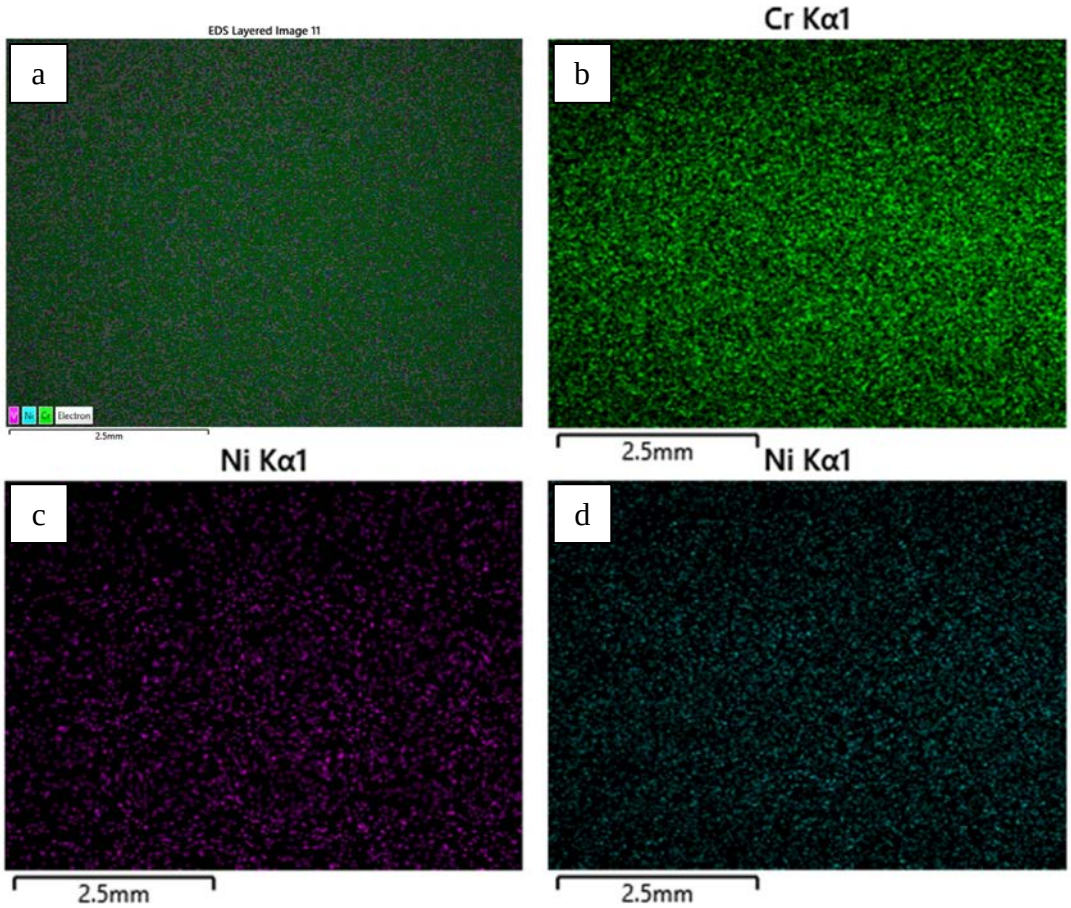

Figure 104: EDX elemental mapping in the top zone of Graded Cube: a) for Cr, Ni, V, b) for Cr, c)for V, d) for Ni.

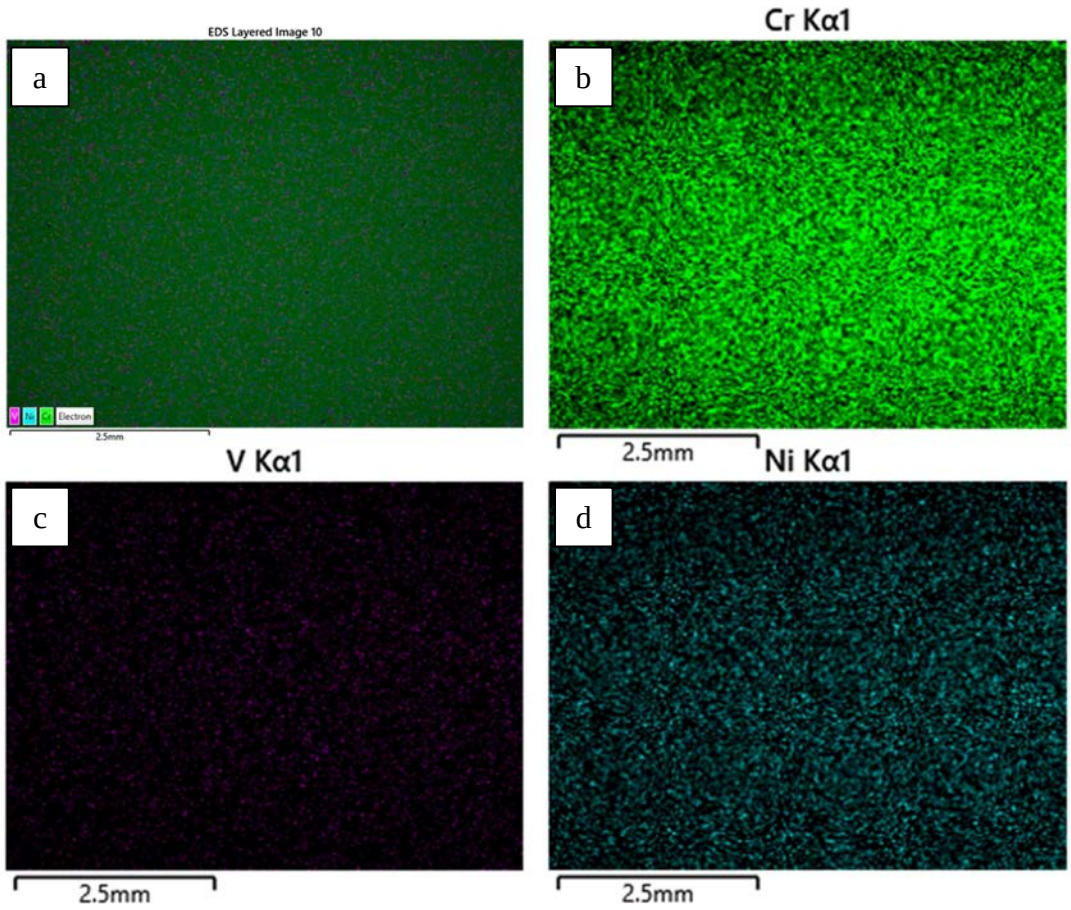

Figure 105: EDX elemental mapping in the bottom zone of Graded Cube: a) for Cr, Ni, V, b) for Cr, c)for V, d) for Ni.

As above-mentioned, from top to bottom, the H13 gradually decreases as well as the 316L increases. EDX analysis has confirmed the gradual variation of chemical composition: from top to bottom, a reduction of Vanadium and Chromium (for the chemical composition of H13 powders, see Table 4) and a gradual increment of Nickel (for the chemical composition of 316L powders, Table 3), as expected.

The results of the chemical analysis of the Wafer cube are shown in Figure 106. A clear difference in the chemical composition can be appreciated in both 316L and H13 layers.

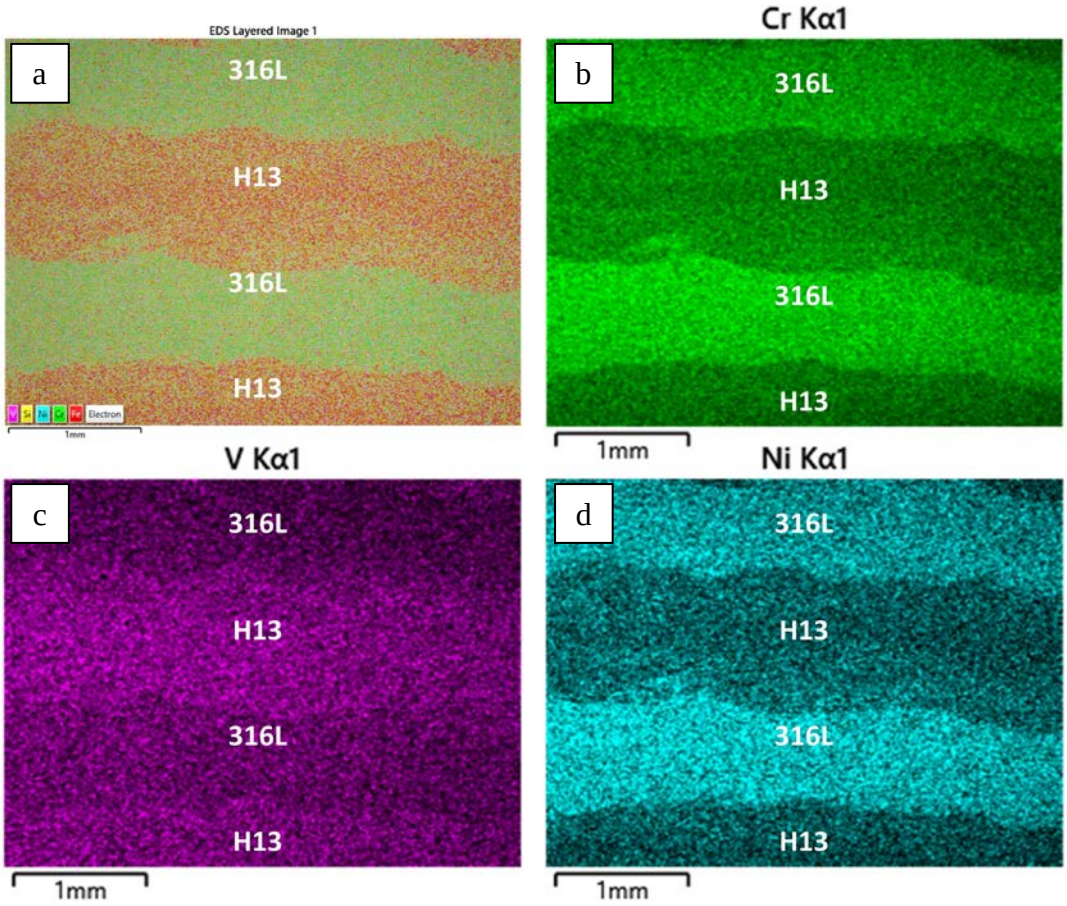

Figure 106: EDX elemental mapping in Wafer Cube: a) for Cr, Ni, V, b) for Cr, c)for V, d) for Ni.

The hardness profile of the Graded Cube is shown in Figure 107. As expected, the microhardness gradually increases as well as the percentage of the H13 increases.

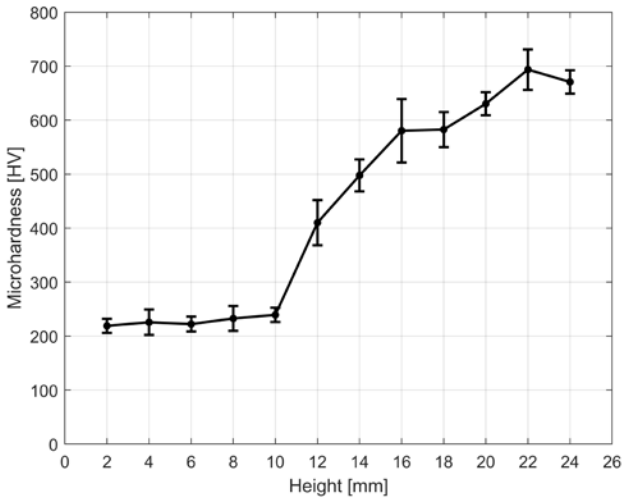

Figure 107: Microhardness versus height in the Graded Cube.

In the bottom and top zones, the microhardness values are typical of the 316L and H13, respectively, ~200HV and ~700HV, with an intermediate zone characterized by mean values.

The hardness profile of the Wafer Cube is displayed in Figure 108. As expected, the microhardness alternates high and low values of microhardness related to 316L and H13.

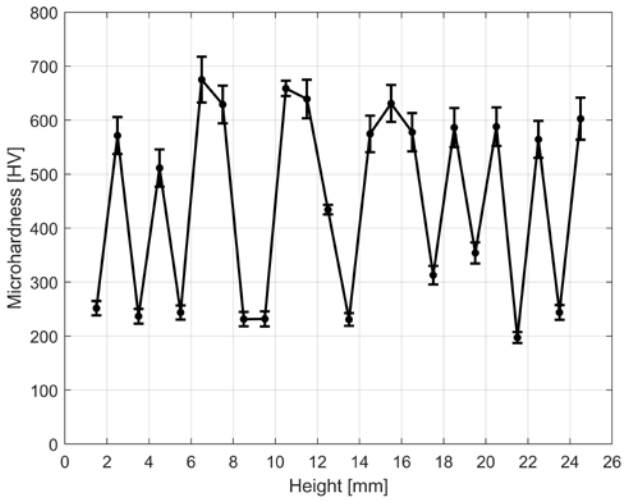

Figure 108: Microhardness versus height in the Wafer Cube.

In conclusion, the FGM structures produced via DLD validate the robustness of the suggested manufacturing guidelines and the appropriate management of the process parameters.

Conclusions

The aim of the present work was to generate, through an experiments-based approach, new knowledge that can be immediately used to widen the actual landscape of DLD production of engineered high-performing components with custom and tailored properties. Two different but complementary research paths have been defined to tackle the above-recalled aims:

i) explore the potentialities of DLD in producing customized components, tailoring both mechanical properties and chemical composition;

ii) the formulation of reliable process guidelines, overcoming the actual poor robustness of the technology for creating functionally graded structures.

The findings related to each objective are discussed in the following:

i) Direct Laser Deposition for Functionally Graded Materials

The experimental campaign has been started with the characterization of the feedstock, specifically, powders of stainless steel 316L and hot-work tool steel H13. Internal defects, such as porosities, and external defects, such as cracks, powders agglomerations and irregular shapes, have been detected during the analyses. Nevertheless, the presence of these imperfections doesn't affect the final workpiece in compliance with the literature.

Then, to fill the gap of knowledge regarding the specific suggestions to manufacture H13, a window of process parameters that allows successfully depositing H13 has been drawn. Therefore, the characterization of the feedstock has been succeeded by the study of single tracks. All the twenty-four combinations of laser power (from 1400W to 2000W, with an increment of 200W), powder feed rate (9, 12, 15 g/min) and scanning speed (1000 and 1200 mm/min) lead to effective depositions, with no detachments. With the lowest laser power value, the dilution is too low for 3D printing, but the combination of parameters seems to be suitable for coating purposes. Then, the dilution increases with the increment of laser power. Other considerations have been made about the geometrical characterization of the single tracks, but they will be discussed in the following point. EDX analyses have shown good miscibility of the H13 and 316L and the presence of heavy carbides on the grain boundaries, while SEM images have revealed the absence of internal cracks and macro porosities and the typical microstructures of the material processed via DLD.

Then, it has been investigated how to deposit single traces adjacently. The experimental campaign of the single layers has included two combinations of process parameters on the basis of the previous outcomes, and the introduction of two more variables: the overlap (from 30% to 70%, with an

increment of 15%) and the deposition strategies (ZIG and ZIGZAG). The results have pointed out that these parameters statistically strongly affect the waviness (an important surface parameter to evaluate the deposition), and two of them also the microhardness values (in this case, the influence of the strategy is negligible). In particular, an overlap equal to 60%, the combination-B of process parameters and the ZIG strategy are suggested for 3D printing H13 to obtain the lowest value of waviness and significative values of microhardness.

In conclusion, using both the manufacturer's suggestions to make 316L and the previous results for H13, two types of FGMs items have been produced: Graded structures (G), characterized by a gradient in chemical composition from the bottom, consisting of 100% 316L, which gradually decreases with increasing H13 until it disappears towards the top, composed of 100% H13; Wafer structures (W), consisting of alternating single layers of 316L and H13. In both cases, the FGMs parts are compliant with the requirements in terms of chemical composition, acceptable defects, microstructures evolution, hardness behavior and mechanical properties.

The properties of the new 316L-H13 material obtained are compliant with the metallurgical and mechanical requirements. Indeed, after the correct balance of the most influent process parameters, it is possible to change the chemical composition in order to obtain tailored microstructure in different zones of the same component, resulting in customized properties, and this is the nature of Functionally Graded Materials.

In particular, in the G-structures, the gradient in the chemical composition has been verified by an EDX analysis. The SEM analyses show a gradual path from 316L microstructures to H13 ones has been observed, in combination with the presence of micro-porosities and the absence of cracks. This metallurgical evolution results in the gradient of microhardness, showing the characteristic low hardness of 316L (~200HV) at the bottom of the specimen, the typical hardness of H13 (~700HV) at the top, through a gradual increment of the microhardness that reflects the H13 incremental composition. It can be assumed that the detected microporosities are not relevant, considering that the microhardness is comparable to the individual material's ones.

Moreover, the three-point bending tests have confirmed the feasibility of making workpieces characterized by tailored properties: failure at bending has different behavior according to the material located at the outer, specifically a ductile failure in the case of 316 and a brittle failure in the case of H13.

Concerning the W-structures, the alternative changes in the designed chemical composition and microstructures have been verified through the SEM and EDX analyses. Although more sudden passages from 316L to H13 microstructures and vice versa have been observed, once again, no cracks have been detected, both intra-layers and between the layers. The metallurgical considerations result

in the alternation of the hardness, layers composed of 100% 316L and layers consisting of 100% H13 generally have reached the typical hardness values of the materials when deposited via DLD individually. Consequently, as well as for the Graded structures, the microporosities found are not influent.

The results of the mechanical tests have highlighted an interesting mechanical behavior of the W-structures, characterized by a mix of brittle and ductile failure at bending: ductile in the 316L-layer, brittle in the H13-layer.

In addition, detailed information on the process parameters used to obtain these results is provided, also to fill the gap of knowledge related both to the H13 tool steel and 316L-H13 FGMs structures produced with the commercial machine described in the introduction chapters.

In summary, the feasibility of DLD fabrication of FGMs structures has been demonstrated and it is now possible to affirm that DLD workpieces with changes in chemical composition layer by layer can lead to tailored properties and can be used to improve the performance of components depending on the application.

ii) Manufacturing guidelines

Specific suggestions have been provided for the production of FGMs exploiting DLD technology in order to obtain manufacturing guidelines. All the experimental campaigns have been carried out following precise procedures defined and explained in detail: the optimization of the process parameters begins with a characterization of the feedstock, then with the single layers analyses (if the purpose is to print bulk 3D structures) or with thin walls analyses (if the final item is a thin-wall structure). The printing of 3D structures represents the last step to assess the validity of the outcomes. Particular attention was paid to the study of single tracks, and experimental-based indications are drawn to overcome the lack of standardization for the assessment of the single tracks, on the basis of reference microhardness values, chemical composition and quantitative geometrical parameters, that have included aspect ratio, dilution and shift as characterizing parameters. Specifically, STs should reach hardness values, at least, compliant with the literature, and provide the best trade-off between geometrical characteristics ($\alpha>100°$, $AR>5$, $10\%<DIL<30\%$, $\mu<50\mu m$).

The printing of FGMs benchmarks has validated the robustness of the suggested manufacturing guidelines and the appropriate management of the process parameters. It has been verified that, also with smaller changes in composition (regarding the Graded structures) and with higher dimensions (regarding the Wafer structure), the properties can be tailored and reflect the design data, considering that the required chemical composition variation, microstructures evolution, and hardness behaviour have been achieved.

Apparatuses

List of figures

List of tables

Nomenclature and Abbreviations

α	-	Wetting angle
A_c	-	Area of molten material below the base metal surface
AISI	-	American Iron and Steel Institute
AM	-	Additive Manufacturing
A_m	-	Area of molten material under the base metal surface
ANOVA	-	Analysis of Variance
AR	-	Aspect Ratio
CAD	-	Computer-Aided Design
CAM	-	Computer-Aided Manufacturing
CFF	-	Continuous Fiber/Filament Fabrication
d	-	Penetration depth
DED	-	Directed Energy Deposition
DIL	-	Dilution
DLD	-	Direct Laser Deposition
DoF	-	Degrees of Freedom
EBM	-	Electron Beam Welding
EDM	-	Electrical Discharge Machining
EDX	-	Energy Dispersive X-ray Spectroscopy
FDM	-	Fused Deposition Modeling
FFF	-	Fused Filament Fabrication
FGM	-	Functionally Graded Materials
G	-	Graded structure
GZ	-	Graded structure with Zig deposition strategy
GZZ	-	Graded structure with ZigZag deposition strategy
h	-	Clad Height
HV	-	Vickers Hardness
LENS	-	Laser Engineered Net Shaping
L-PBF	-	Laser- Powder-Bed Fusion
$\dot{m}_p$	-	Powder Feed Rate
OV	-	Overlap
P	-	Laser Power
s	-	Shift

SEM	-	Scanning Electron Microscopy
SL	-	Single Layers
SLM	-	Selective Laser Melting
ST	-	Single Tracks
v	-	Scanning Speed
w	-	Width of the track

References

[1] D. Guo *et al.*, “Synchroperation in industry 4.0 manufacturing,” *Int. J. Prod. Econ.*, vol. 238, no. March, p. 108171, 2021, doi: 10.1016/j.ijpe.2021.108171.

[2] G. Erboz, “How to Define Industry 40: The Main Pillars of Industry 4.0,” *Manag. Trends Dev. Enterp. Glob. Era*, no. November 2017, pp. 761–767, 2017.

[3] I. Gibson, D. Rosen, and B. Stucker, *Additive manufacturing technologies: 3D printing, rapid prototyping, and direct digital manufacturing, second edition*. 2015.

[4] U. M. Dilberoglu, B. Gharehpapagh, U. Yaman, and M. Dolen, “The Role of Additive Manufacturing in the Era of Industry 4.0,” *Procedia Manuf.*, vol. 11, no. June, pp. 545–554, 2017, doi: 10.1016/j.promfg.2017.07.148.

[5] ASTM International, “ASTM F2792 - 10,” *Standard Terminology for Additive Manufacturing Technologies*, 2010. .

[6] ISO/ASTM 52900, “Standard Terminology for Additive Manufacturing – General Principles – Terminology (ISO/ASTM 52900:2015(E)),” *ASTM International*, 2015. .

[7] Y. Shi, Y. Zhang, S. Baek, W. De Backer, and R. Harik, “Manufacturability analysis for additive manufacturing using a novel feature recognition technique,” *Comput. Aided. Des. Appl.*, 2018, doi: 10.1080/16864360.2018.1462574.

[8] M. Attaran, “The rise of 3-D printing: The advantages of additive manufacturing over traditional manufacturing,” *Bus. Horiz.*, 2017, doi: 10.1016/j.bushor.2017.05.011.

[9] R. Bogue, “3D printing: The dawn of a new era in manufacturing?,” *Assem. Autom.*, 2013, doi: 10.1108/AA-06-2013-055.

[10] https://am-power.de/tools/metal-additive-manufacturing/#av_section_2, “No Title.” .

[11] T. Gornet, “History of Additive Manufacturing,” pp. 1–24, 2017, doi: 10.4018/978-1-5225-2289-8.ch001.

[12] Z. Liu, Y. Wang, B. Wu, C. Cui, Y. Guo, and C. Yan, “A critical review of fused deposition modeling 3D printing technology in manufacturing polylactic acid parts,” *International Journal of Advanced Manufacturing Technology*. 2019, doi: 10.1007/s00170-019-03332-x.

[13] A. Nassar, E. Nassar, and M. Younis, “A novel design to external filament extruder for 3D printer,” *Aust. J. Mech. Eng.*, pp. 1–8, Apr. 2019, doi: 10.1080/14484846.2019.1605684.

[14] A. D. Valino, J. R. C. Dizon, A. H. Espera, Q. Chen, J. Messman, and R. C. Advincula,

"Advances in 3D printing of thermoplastic polymer composites and nanocomposites," *Progress in Polymer Science*. 2019, doi: 10.1016/j.progpolymsci.2019.101162.

[15] M. W. M. Cunico, D. A. Kai, P. M. Cavalheiro, and J. de Carvalho, "Development and characterisation of 3D printing finishing process applying recycled plastic waste," *Virtual Phys. Prototyp.*, vol. 14, no. 1, pp. 37–52, Jan. 2019, doi: 10.1080/17452759.2018.1521248.

[16] F. Ning, W. Cong, Y. Hu, and H. Wang, "Additive manufacturing of carbon fiber-reinforced plastic composites using fused deposition modeling: Effects of process parameters on tensile properties," *J. Compos. Mater.*, vol. 51, no. 4, pp. 451–462, Feb. 2017, doi: 10.1177/0021998316646169.

[17] D. C. Deisenroth, R. Moradi, A. H. Shooshtari, F. Singer, A. Bar-Cohen, and M. Ohadi, "Review of Heat Exchangers Enabled by Polymer and Polymer Composite Additive Manufacturing," *Heat Transf. Eng.*, vol. 39, no. 19, pp. 1648–1664, Nov. 2018, doi: 10.1080/01457632.2017.1384280.

[18] D. K. Rajak, D. D. Pagar, P. L. Menezes, and E. Linul, "Fiber-reinforced polymer composites: Manufacturing, properties, and applications," *Polymers*. 2019, doi: 10.3390/polym11101667.

[19] R. J. Hart, E. G. Patton, and O. Sapunkov, "Characterization of Continuous Fiber-Reinforced Composite Materials Manufactured Via Fused Filament Fabrication02," p. 14, 2018.

[20] A. T. Silvestri, I. Papa, F. Rubino, and A. Squillace, "On the critical technological issues of CFF: enhancing the bearing strength," *Mater. Manuf. Process.*, vol. 0, no. 0, pp. 1–14, 2021, doi: 10.1080/10426914.2021.1954195.

[21] A. El Hassanin *et al.*, "Laser-powder bed fusion of pre-mixed Inconel718-Cu powders : An experimental study," *J. Manuf. Process.*, vol. 71, no. September, pp. 329–344, 2021, doi: 10.1016/j.jmapro.2021.09.028.

[22] W. E. Frazier, "Metal Additive Manufacturing: A Review," *J. Mater. Eng. Perform.*, vol. 23, no. 6, pp. 1917–1928, 2014, doi: 10.1007/s11665-014-0958-z.

[23] A. T. Silvestri, S. Foglia, R. Borrelli, S. Franchitti, C. Pirozzi, and A. Astarita, "Electron beam melting of Ti6Al4V: Role of the process parameters under the same energy density," *J. Manuf. Process.*, vol. 60, pp. 162–179, 2020, doi: https://doi.org/10.1016/j.jmapro.2020.10.065.

[24] S. Liu and Y. C. Shin, "Additive manufacturing of Ti6Al4V alloy: A review," *Mater. Des.*,

vol. 164, p. 107552, 2019, doi: https://doi.org/10.1016/j.matdes.2018.107552.

[25] I. Gibson, D. Rosen, and B. Stucker, *Additive manufacturing technologies: 3D printing, rapid prototyping, and direct digital manufacturing, second edition*. 2015.

[26] N. Ahmed, “Direct metal fabrication in rapid prototyping: A review,” *J. Manuf. Process.*, vol. 42, pp. 167–191, 2019, doi: https://doi.org/10.1016/j.jmapro.2019.05.001.

[27] ASTM International, “Standard Guide for Directed Energy Deposition of Metals,” *ASTM Stand.*, pp. 1–22, 2016, doi: 10.1520/F3187.

[28] B. Almangour, *Additive Manufacturing of Emerging Materials*. Cham: Springer International Publishing, 2019.

[29] A. Bandyopadhyay and B. Heer, “Additive manufacturing of multi-material structures,” *Mater. Sci. Eng. R Reports*, vol. 129, pp. 1–16, 2018, doi: https://doi.org/10.1016/j.mser.2018.04.001.

[30] F. Hengsbach *et al.*, “Inline additively manufactured functionally graded multi-materials: microstructural and mechanical characterization of 316L parts with H13 layers,” *Prog. Addit. Manuf.*, 2018, doi: 10.1007/s40964-018-0044-4.

[31] I. M. El-Galy, B. I. Saleh, and M. H. Ahmed, “Functionally graded materials classifications and development trends from industrial point of view,” *SN Applied Sciences*. 2019, doi: 10.1007/s42452-019-1413-4.

[32] A. Reichardt *et al.*, “Advances in additive manufacturing of metal-based functionally graded materials,” *Int. Mater. Rev.*, 2021, doi: 10.1080/09506608.2019.1709354.

[33] S. S. Wang, “Fracture Mechanics for Delamination Problems in Composite Materials,” *J. Compos. Mater.*, 1983, doi: 10.1177/002199838301700302.

[34] N. Noda, “Thermal stresses in functionally graded materials,” *J. Therm. Stress.*, 1999, doi: 10.1080/014957399280841.

[35] W. Zhang, M. Soshi, and K. Yamazaki, “Development of an additive and subtractive hybrid manufacturing process planning strategy of planar surface for productivity and geometric accuracy,” *Int. J. Adv. Manuf. Technol.*, vol. 109, no. 5–6, pp. 1479–1491, 2020, doi: 10.1007/s00170-020-05733-9.

[36] R. M. Mahamood, E. T. Akinlabi, M. Shukla, and S. Pityana, “Functionally graded material: An overview,” 2012.

[37] S. K. Bohidar, R. Sharma, and P. R. Mishra, “Functionally Graded Materials: A Critical Review,” *Int. J. Res.*, 2014.

[38] G. E. Knoppers, J. W. Gunnink, J. Van Den Hout, and W. P. Van Vliet, “The reality of functionally graded material products,” *Proc. Solid Free. Fabr. Symp.*, 2004.

[39] F. Xu, X. Zhang, and H. Zhang, “A review on functionally graded structures and materials for energy absorption,” *Engineering Structures*. 2018, doi: 10.1016/j.engstruct.2018.05.094.

[40] Y. Li *et al.*, “A Review on Functionally Graded Materials and Structures via Additive Manufacturing: From Multi-Scale Design to Versatile Functional Properties,” *Advanced Materials Technologies*. 2020, doi: 10.1002/admt.201900981.

[41] Y. Zhang *et al.*, “Additive Manufacturing of Metallic Materials: A Review,” *Journal of Materials Engineering and Performance*. 2018, doi: 10.1007/s11665-017-2747-y.

[42] C. Kledwig, H. Perfahl, M. Reisacher, F. Brückner, J. Bliedtner, and C. Leyens, “Analysis of melt pool characteristics and process parameters using a coaxial monitoring system during directed energy deposition in additive manufacturing,” *Materials (Basel).*, 2019, doi: 10.3390/ma12020308.

[43] K. A. Lorenz, J. B. Jones, D. I. Wimpenny, and M. R. Jackson, “A review of hybrid manufacturing,” 2020.

[44] M. Cortina, J. I. Arrizubieta, J. E. Ruiz, E. Ukar, and A. Lamikiz, “Latest developments in industrial hybrid machine tools that combine additive and subtractive operations,” *Materials (Basel).*, vol. 11, no. 12, 2018, doi: 10.3390/ma11122583.

[45] F. Valjak and N. Bojčetić, “Conception of design principles for additive manufacturing,” *Proc. Int. Conf. Eng. Des. ICED*, vol. 2019-Augus, no. August, pp. 689–698, 2019, doi: 10.1017/dsi.2019.73.

[46] T. A. Amine, T. E. Sparks, and F. Liou, “A strategy for fabricating complex structures via a hybrid manufacturing process,” *22nd Annu. Int. Solid Free. Fabr. Symp. - An Addit. Manuf. Conf. SFF 2011*, pp. 175–184, 2011.

[47] B. Zhang, A. Goel, O. Ghalsasi, and S. Anand, “CAD-based design and pre-processing tools for additive manufacturing,” *J. Manuf. Syst.*, vol. 52, no. February, pp. 227–241, 2019, doi: 10.1016/j.jmsy.2019.03.005.

[48] Y. Hosoi, “Introduction to stainless steel,” *Keikinzoku/Journal Japan Inst. Light Met.*, vol. 37, no. 9, pp. 624–635, 1987, doi: 10.2464/jilm.37.624.

[49] F. Bartolomeu *et al.*, “316L stainless steel mechanical and tribological behavior—A comparison between selective laser melting, hot pressing and conventional casting,” *Addit. Manuf.*, vol. 16, pp. 81–89, 2017, doi: 10.1016/j.addma.2017.05.007.

[50] J. R. Davis, *Asm Specialty Handbook: Stainless Steels*. 1994.

[51] G. Roberts, G. Krauss, and R. Kennedy, “Tool Steels: 5th Edition,” *Book*, 1998.

[52] T. Grimm, G. Wiora, and G. Witt, “Characterization of typical surface effects in additive manufacturing with confocal microscopy,” *Surf. Topogr. Metrol. Prop.*, 2015, doi: 10.1088/2051-672X/3/1/014001.

[53] A. Townsend, N. Senin, L. Blunt, R. K. Leach, and J. S. Taylor, “Surface texture metrology for metal additive manufacturing: a review,” *Precision Engineering*. 2016, doi: 10.1016/j.precisioneng.2016.06.001.

[54] T. Materials, *ASM Handbook, Volume 9, Metallography and Microstructures*. 2004.

[55] ASTM E92-82(2003), *Standard Test Method for Vickers Hardness of Metallic Materials*. 2008.

[56] S. M. Thompson, L. Bian, N. Shamsaei, and A. Yadollahi, “An overview of Direct Laser Deposition for additive manufacturing; Part I: Transport phenomena, modeling and diagnostics,” *Addit. Manuf.*, vol. 8, pp. 36–62, Oct. 2015, doi: 10.1016/j.addma.2015.07.001.

[57] N. Shamsaei, A. Yadollahi, L. Bian, and S. M. Thompson, “An overview of Direct Laser Deposition for additive manufacturing; Part II: Mechanical behavior, process parameter optimization and control,” *Addit. Manuf.*, vol. 8, pp. 12–35, 2015, doi: 10.1016/j.addma.2015.07.002.

[58] B. Bax, R. Rajput, R. Kellet, and M. Reisacher, “Systematic evaluation of process parameter maps for laser cladding and directed energy deposition,” *Addit. Manuf.*, vol. 21, no. January, pp. 487–494, 2018, doi: 10.1016/j.addma.2018.04.002.

[59] P. Shayanfar, H. Daneshmanesh, and K. Janghorban, “Parameters Optimization for Laser Cladding of Inconel 625 on ASTM A592 Steel,” *J. Mater. Res. Technol.*, vol. 9, no. 4, pp. 8258–8265, 2020, doi: 10.1016/j.jmrt.2020.05.094.

[60] C. P. Paul, P. Bhargava, A. Kumar, A. K. Pathak, and L. M. Kukreja, “Laser rapid manufacturing: technology, applications, modeling and future prospects,” *Lasers Manuf.*, pp. 1–67, 2013.

[61] L. Tang and R. G. Landers, “Melt pool temperature control for laser metal deposition

processes-part I: Online temperature control," *J. Manuf. Sci. Eng. Trans. ASME*, vol. 132, no. 1, pp. 0110101–0110109, 2010, doi: 10.1115/1.4000882.

[62] F. Mazzucato, D. Forni, A. Valente, and E. Cadoni, "Laser metal deposition of inconel 718 alloy and as-built mechanical properties compared to casting," *Materials (Basel).*, vol. 14, no. 2, pp. 1–21, 2021, doi: 10.3390/ma14020437.

[63] P. Guo, B. Zou, C. Huang, and H. Gao, "Study on microstructure, mechanical properties and machinability of efficiently additive manufactured AISI 316L stainless steel by high-power direct laser deposition," *J. Mater. Process. Technol.*, 2017, doi: 10.1016/j.jmatprotec.2016.09.005.

[64] K. Zhang, S. Wang, W. Liu, and X. Shang, "Characterization of stainless steel parts by Laser Metal Deposition Shaping," *Mater. Des.*, 2014, doi: 10.1016/j.matdes.2013.09.006.

[65] A. Hansel *et al.*, "Study on Consistently Optimum Deposition Conditions of Typical Metal Material Using Additive/Subtractive Hybrid Machine Tool," 2016, doi: 10.1016/j.procir.2016.04.113.

[66] L. V. M. Antony and R. G. Reddy, "Processes for production of high-purity metal powders," *JOM*, 2003, doi: 10.1007/s11837-003-0153-4.

[67] E. M. Trent, "Mechanical methods of powder production as used in the carbide industry," *Powder Metall.*, 1958, doi: 10.1179/pom.1958.1.1-2.008.

[68] J. Dawes, R. Bowerman, and R. Trepleton, "Introduction to the additive manufacturing powder metallurgy supply chain," *Johnson Matthey Technol. Rev.*, vol. 59, no. 3, pp. 243–256, 2015, doi: 10.1595/205651315X688686.

[69] A. Popovich and V. Sufiiarov, "Metal Powder Additive Manufacturing," in *New Trends in 3D Printing*, 2016.

[70] A. J. Pinkerton and L. Li, "Direct additive laser manufacturing using gas- and water-atomised H13 tool steel powders," *Int. J. Adv. Manuf. Technol.*, vol. 25, no. 5–6, pp. 471–479, 2005, doi: 10.1007/s00170-003-1844-2.

[71] U. Ali *et al.*, "On the measurement of relative powder-bed compaction density in powder-bed additive manufacturing processes," *Mater. Des.*, 2018, doi: 10.1016/j.matdes.2018.06.030.

[72] I. E. Anderson, E. M. H. White, and R. Dehoff, "Feedstock powder processing research needs for additive manufacturing development," *Curr. Opin. Solid State Mater. Sci.*, vol. 22, no. 1, pp. 8–15, 2018, doi: 10.1016/j.cossms.2018.01.002.

[73] S. Singh, S. Ramakrishna, and R. Singh, “Material issues in additive manufacturing: A review,” *Journal of Manufacturing Processes*. 2017, doi: 10.1016/j.jmapro.2016.11.006.

[74] ASTM B822-17, “Standard test method for particle size distribution of metal powders and related compounds by light scattering,” *ASTM Int. West Conshohocken, PA*, 2017.

[75] S. Y. Wen, Y. C. Shin, J. Y. Murthy, and P. E. Sojka, “Modeling of coaxial powder flow for the laser direct deposition process,” *Int. J. Heat Mass Transf.*, 2009, doi: 10.1016/j.ijheatmasstransfer.2009.07.018.

[76] A. F3049 − 14, “Standard Guide for Characterizing Properties of Metal Powders Used for Additive Manufacturing Processes,” *F3049 - 14*, 2014.

[77] A. T. Silvestri, S. Amirabdollahian, M. Perini, P. Bosetti, and A. Squillace, “Direct Laser Deposition for Tailored Structure,” *ESAFORM 2021*, 2021, doi: 10.25518/esaform21.4124.

[78] S. Sreekanth, K. Hurtig, S. Joshi, and J. Andersson, “Influence of laser-directed energy deposition process parameters and thermal post-treatments on Nb-rich secondary phases in single-track Alloy 718 specimens,” *J. Laser Appl.*, vol. 33, no. 2, p. 022024, 2021, doi: 10.2351/7.0000259.

[79] S. Kapil, F. Legesse, S. Negi, K. P. Karunakaran, and S. Bag, “Hybrid layered manufacturing of a bimetallic injection mold of P20 tool steel and mild steel with conformal cooling channels,” *Prog. Addit. Manuf.*, vol. 5, no. 2, pp. 183–198, 2020, doi: 10.1007/s40964-020-00129-3.

[80] J. Mazumder, J. Choi, K. Nagarathnam, J. Koch, and D. Hetzner, “The direct metal deposition of H13 tool steel for 3-D components,” *Jom*, vol. 49, no. 5, pp. 55–60, 1997, doi: 10.1007/BF02914687.

[81] M. Wang *et al.*, “High-Temperature Properties and Microstructural Stability of the AISI H13 Hot-Work Tool Steel Processed by Selective Laser Melting,” *Metall. Mater. Trans. B Process Metall. Mater. Process. Sci.*, vol. 50, no. 1, pp. 531–542, 2019, doi: 10.1007/s11663-018-1442-1.

[82] E. B. Fonseca, A. H. G. Gabriel, L. C. Araújo, P. L. L. Santos, K. N. Campo, and E. S. N. Lopes, “Assessment of laser power and scan speed influence on microstructural features and consolidation of AISI H13 tool steel processed by additive manufacturing,” *Addit. Manuf.*, vol. 34, no. March, p. 101250, 2020, doi: 10.1016/j.addma.2020.101250.

[83] P. Wołosz, A. Baran, and M. Polański, “The influence of laser engineered net shaping

(LENS^{TM}) technological parameters on the laser deposition efficiency and properties of H13 (AISI) steel," *J. Alloys Compd.*, vol. 823, 2020, doi: 10.1016/j.jallcom.2020.153840.

[84] S. Amirabdollahian, F. Deirmina, M. Pellizzari, P. Bosetti, and A. Molinari, "Tempering behavior of a direct laser deposited hot work tool steel: Influence of quenching on secondary hardening and microstructure," *Mater. Sci. Eng. A*, vol. 814, no. March, p. 141126, 2021, doi: 10.1016/j.msea.2021.141126.

[85] A. T. Silvestri *et al.*, "Assessment of the mechanical properties of AlSi10Mg parts produced through selective laser melting under different conditions," 2020, doi: 10.1016/j.promfg.2020.04.115.

[86] T. Bhardwaj, M. Shukla, C. P. Paul, and K. S. Bindra, "Direct Energy Deposition - Laser Additive Manufacturing of Titanium-Molybdenum alloy: Parametric studies, microstructure and mechanical properties," *J. Alloys Compd.*, vol. 787, pp. 1238–1248, 2019, doi: 10.1016/j.jallcom.2019.02.121.

[87] L. Costa *et al.*, "A simplified semi-empirical method to select the processing parameters for laser clad coatings," *Mater. Sci. Forum*, vol. 414–415, no. March 2015, pp. 385–394, 2003, doi: 10.4028/www.scientific.net/msf.414-415.385.

[88] A. Riquelme, P. Rodrigo, M. D. Escalera-Rodríguez, and J. Rams, "Analysis and optimization of process parameters in Al-SiCp laser cladding," *Opt. Lasers Eng.*, vol. 78, pp. 165–173, 2016, doi: 10.1016/j.optlaseng.2015.10.014.

[89] K. M. Jasim, R. D. Rawlings, and D. R. F. West, "Metal-ceramic functionally gradient material produced by laser processing," *J. Mater. Sci.*, vol. 28, no. 10, pp. 2820–2826, 1993, doi: 10.1007/BF00356225.

[90] R. Colaco, T. Carvalho, and R. Vilar, "Laser cladding of stellite 6 on steel substrates," *High Temp. Chem. Proc.*, vol. 3, no. 3, pp. 21–29, 1994.

[91] J. Tuominen, M. Kaubisch, S. Thieme, J. Näkki, S. Nowotny, and P. Vuoristo, "Laser strip cladding for large area metal deposition," *Addit. Manuf.*, vol. 27, no. January, pp. 208–216, 2019, doi: 10.1016/j.addma.2019.01.008.

[92] H. S. Carslaw and J. C. Jaeger, "Conduction of heat in solids," Clarendon Press, 1959.

[93] D. Rosenthal, "The Theory of Moving Source of Heat and its Application to Metal Transfer," *ASME Transactions*. 1946.

[94] S. Sun, M. Brandt, J. Harris, and Y. Durandet, "The influence of stellite 6 particle size on the

inter-track porosity in multi-track cladding," *Surf. Coatings Technol.*, vol. 201, no. 3–4, pp. 998–1005, 2006, doi: 10.1016/j.surfcoat.2006.01.008.

[95] S. L. Campanelli, A. Angelastro, C. G. Signorile, and G. Casalino, "Investigation on direct laser powder deposition of 18 Ni (300) marage steel using mathematical model and experimental characterisation," *Int. J. Adv. Manuf. Technol.*, 2017, doi: 10.1007/s00170-016-9135-x.

[96] V. Ocelík, U. de Oliveira, M. de Boer, and J. T. M. de Hosson, "Thick Co-based coating on cast iron by side laser cladding: Analysis of processing conditions and coating properties," *Surf. Coatings Technol.*, 2007, doi: 10.1016/j.surfcoat.2006.10.044.

[97] A. Dass and A. Moridi, "State of the Art in Directed Energy Deposition : From," *Coatings*, 2019.

[98] R. Cottam, J. Wang, and V. Luzin, "Characterization of microstructure and residual stress in a 3D H13 tool steel component produced by additive manufacturing," *J. Mater. Res.*, vol. 29, no. 17, pp. 1978–1986, 2014, doi: 10.1557/jmr.2014.190.

[99] J. Mazumder, A. Schifferer, and J. Choi, "Direct materials deposition: Designed macro and microstructure," *Mater. Res. Innov.*, vol. 3, no. 3, pp. 118–131, 1999, doi: 10.1007/s100190050137.

[100] J. Choi and Y. Chang, "Characteristics of laser aided direct metal/material deposition process for tool steel," *Int. J. Mach. Tools Manuf.*, vol. 45, no. 4–5, pp. 597–607, 2005, doi: 10.1016/j.ijmachtools.2004.08.014.

[101] A. Bohlen, H. Freiße, M. Hunkel, and F. Vollertsen, "Additive manufacturing of tool steel by laser metal deposition," *Procedia CIRP*, vol. 74, pp. 192–195, 2018, doi: 10.1016/j.procir.2018.08.092.

[102] J. S. Park, J. H. Park, M. G. Lee, J. H. Sung, K. J. Cha, and D. H. Kim, "Effect of Energy Input on the Characteristic of AISI H13 and D2 Tool Steels Deposited by a Directed Energy Deposition Process," *Metall. Mater. Trans. A Phys. Metall. Mater. Sci.*, vol. 47, no. 5, pp. 2529–2535, 2016, doi: 10.1007/s11661-016-3427-5.

[103] S. Suryakumar, K. P. Karunakaran, A. Bernard, U. Chandrasekhar, N. Raghavender, and D. Sharma, "Weld bead modeling and process optimization in Hybrid Layered Manufacturing," *CAD Comput. Aided Des.*, vol. 43, no. 4, pp. 331–344, 2011, doi: 10.1016/j.cad.2011.01.006.

[104] D. C. Montgomery, *Design and analysis of experiments*. John wiley & sons, 2017.

[105] R. Leach, *Characterisation of areal surface texture*. 2013.

[106] X. Cao, B. Lin, and X. Zhang, "A study on grinding surface waviness of woven ceramic matrix composites," *Appl. Surf. Sci.*, vol. 270, pp. 503–512, 2013, doi: 10.1016/j.apsusc.2013.01.069.

[107] T. Kozior, J. Bochnia, P. Zmarzły, and D. Gogolewski, "Waviness of Freeform Surface Characterizations from," *Materials (Basel).*, 2020.

[108] F. Blateyron, "Good practices for the use of areal filters," *3rd Semin. Surf. Metrol. Am.*, no. August, pp. 1–12, 2014, doi: 10.13140/2.1.1007.9361.

[109] J. Raja, B. Muralikrishnan, and S. Fu, "Recent advances in separation of roughness, waviness and form," *Precis. Eng.*, vol. 26, no. 2, pp. 222–235, 2002, doi: 10.1016/S0141-6359(02)00103-4.

[110] ASME, *Surface Texture, Surface Roughness, Waviness and Lay; ASME B46.1-2019*. 2019.

[111] I. Standard 11266, "ISO 16610-21- Geometrical product specifications (GPS) — Filtration," *61010-1 © Iec2001*, 2014.

[112] ASTM INTERNATIONAL, "Standard Test Methods for Flexural Properties of Unreinforced and Reinforced Plastics and Electrical Insulating Materials. D790," *Annu. B. ASTM Stand.*, pp. 1–12, 2002, doi: 10.1520/D0790-17.2.

[113] M. O. Sklyar, G. A. Turichin, O. G. Klimova, O. G. Zotov, and I. K. Topalov, "Microstructure of 316L stainless steel components produced by direct laser deposition," *Steel Transl.*, vol. 46, no. 12, pp. 883–887, 2016, doi: 10.3103/S096709121612010X.

[114] S. M. Yusuf, Y. Chen, R. Boardman, S. Yang, and N. Gao, "Investigation on porosity and microhardness of 316L stainless steel fabricated by selective laser melting," *Metals (Basel).*, vol. 7, no. 2, pp. 1–12, 2017, doi: 10.3390/met7020064.

[115] A. Yadollahi, N. Shamsaei, S. M. Thompson, and D. W. Seely, "Effects of process time interval and heat treatment on the mechanical and microstructural properties of direct laser deposited 316L stainless steel," *Mater. Sci. Eng. A*, vol. 644, pp. 171–183, 2015, doi: 10.1016/j.msea.2015.07.056.